POLITECNICO DI TORINO

SCUOLA DI DOTTORATO
Dottorato in Metrologia: Scienza e Tecnica delle Misure – XXV ciclo

Tesi di Dottorato

Realization and characterization of optical frequency standards

Marco Pizzocaro

Tutori
ing. Giovanni A. Costanzo
dott. Filippo Levi

Coordinatore del corso di dottorato
prof. Franco Ferraris

Febbraio 2013

Abstract

During the Ph.D. Course I worked on the realization and the characterization of an ytterbium optical frequency standard. Since year 2000, it is possible using optical frequency comb to directly and reliably scale a frequency measurement in the optical domain to a measurement in the microwave domain. This possibility allows the realization of high accuracy and high stability optical frequency standards, whose atomic quality factors are several orders of magnitude higher than the best microwave ones. Among others, the alkaline earth atoms are very promising and, once trapped in an optical lattice, are capable of a short term stability approaching 10^{-15} at 1 s.

A ytterbium optical clock is currently being developed in the laboratories of the Optics Division of Istituto Nazionale di Ricerca Metrologica (INRIM) The experiment aims to cool and trap ytterbium atoms in a two stage magneto-optical trap (MOT) (at 399 nm and 556 nm) and to probe them in an optical lattice with a ultrastable laser at 578 nm.

This thesis presents the realization of the required laser sources, the stabilization of the clock laser, the development of the cooling and trapping stages and the design of a new experimental setup.

The blue and green radiations for the two-stage MOT at 399 nm and 556 nm are obtained by second harmonic generation in non-linear crystals. The yellow clock laser at 578 nm is generated by sum of frequency in non-linear crystal. The clock laser is stabilized with the Pound-Drever-Hall technique on a high-finesse Fabry-Pérot cavity. The temperature stabilization of the cavity is implemented with a novel Active Disturbance Rejection Control scheme. The frequency noise of the laser is characterized with a stability 3×10^{-15} at 1 s. Atoms are trapped in the blue magneto-optical trap at 399 nm and transferred in the green trap at 556 nm. A new experimental setup is designed, studying the vacuum chamber, the MOT coils and the atomic source.

I have been guest researcher at National Institute of Standards and Technology (NIST) for six months in 2011. I will describe development of NIST ytterbium optical clocks during my visit.

Sommario

Durante il corso di Dottorato ho lavorato alla realizzazione e caratterizzazione di uno campione ottico di frequenza all'itterbio Dal 2000, è possibile, utilizzando pettini ottici di frequenza, scalare direttamente e in modo affidabile una misura dal dominio ottico al dominio a microonde. Questa possibilità permette la realizzazione di standard ottici di elevata precisione e stabilità in frequenza, i cui fattori di qualità sono diversi ordini di grandezza superiori a quelli migliori a microonde. Tra gli altri, gli atomi alcalino-terrosi sono molto promettenti e, una volta intrappolati in un reticolo ottico, sono in grado di stabilità a breve termine che si avvicinano 10^{-15} a 1 s.

Al laboratorio di tempo e frequenza dell'INRIM un orologio ottico all'itterbio è attualmente in fase di sviluppo. L'esperimento si prefigge di raffreddare e intrappolare atomi di itterbio in una trappola magneto-ottica (MOT) a due stadi (a 399 nm e 556 nm) e interrogare la trasnizione in reticolo ottico con un laser ultrastabile a 578 nm.

Questa tesi presenta la realizzazione delle sorgenti laser necessarie all'esperimento, della stabilizzazione del laser di orologio, dello sviluppo degli stadi di raffreddamento e intrappoleamento e del progetto per un nuovo apparato sperimentale.

Le radiazioni blu e verde per le MOT a 399 nm e 556 nm sono ottenuti per generazione di seconda armonica in cristalli non lineari. Il laser giallo di orologio a 578 nm è generato per somma di frequenze in un altro cristallo non lineare. Il laser di orologio è stato stabilizzato con la tecnica di Pound-Drever-Hall su una cavità Fabry-Pérot ad alta finezza. La stabilizzazione in temperatura della cavità è stata implementata con un nuovo schema di reiezione attiva dei disturbi. Il rumore di frequenza del laser è stato caratterizzato con una stabilità di 3×10^{-15} a 1 s Atomi di itterbio sono stati intrappolati nella MOT blu a 399 nm e trasferiti nella trappola verde a 556 nm. Un nuovo apparato sperimentale è stato progettato, studiando la camera da vuoto, le bobine per la MOT e la sorgente atomica.

Sono stato ricercatore ospite al NIST per sei mesi nel 2011. Descriverò lo sviluppo degli orologi ottici all'itterbio del NIST durante la mia visita.

Ringraziamenti

Grazie a Filippo, Giovanni, Davide, Luca, Salvatore, Alberto, Elio, Claudio e Cecilia.

Grazie a Chris Oates, Nathan Lemke, Jeff Sherman, Andrew Ludlow, Nathan Hinkley e Richard Fox per avermi accolto a Boulder.

Grazie a Massimo Zucco per l'aiuto col comb.

Grazie a Jacopo Catani per i suggerimenti sulla duplicazione del laser blu.

Contents

1 Introduction

The work for this thesis has regarded the realization and characterization of an optical frequency standard base on ytterbium atoms. The experiment has been realized at the laboratories of the Optical Division of Istituto Nazionale di Ricerca Metrologica (INRIM) in Turin. Aim of the experiment is the realization of a frequency standard with high accuracy and high stability.

1.1 Atomic Frequency Standards

The definition of the second has been traditionally based on astronomical time scales. The second was defined to be the fraction 1/86 400 of Earth mean solar day. However the period of the Earth's rotation was found to fluctuate and to slowly increase. Because of that in 1960 a new definition was adopted based on the tropical year, that is the motion of Earth on its orbit around the sun.

At the time of this definition, scientists had already shown that an atomic standard of frequency, based on a transition between two energy levels of an atom or a molecule, could be realized. According to quantum mechanics [1], the energy of electrons in an atom can assume only discrete values. A transition between two energy levels E_1 and E_2 can be probed by the emission or absorption of a photon at the frequency $\nu_0 = |E_1 - E_2|/h$, where h is the Planck constant. Unlike Earth motion, an atomic transition frequency can be readily measured and, once corrected for perturbations, is universal, determined only by quantum mechanics and fundamental constants. An atomic frequency standard (atomic clock) can be realized matching the frequency of an external oscillator to the frequency ν_0. The first caesium atomic clock was successfully demonstrated by Essen and Parry in 1955 [2].

From 1967 the International System of Units (SI) [3] defines the second as the duration of 9 192 631 770 periods of the radiation corresponding to the transition between the two hyperfine levels of the ground state of the caesium 133 atom. The current definition of the second is thus realized by microwave caesium frequency standards, their frequency fixed by definition $\nu_0 = 9\,192\,631\,770\,\mathrm{Hz}$ in continuity with the measure done in 1958 respect to the previous definition [4].

The performances of frequency standards are characterized by two figures of merit: accuracy and instability [5]. Accuracy is the closeness of agreement between the frequency realized by the standard and the frequency of the unperturbed atomic transition. Instability is a statistical measure of how much the frequency changes over time. Accuracy of the standard cannot be better than the instability of the standard.

Several factors can perturb the measured frequency of an atomic transition and thus limit the accuracy of the standard. Each factor should be limited or well controlled to reduce their contribution to the uncertainty budget. The principal of these perturbations is the Doppler effect; an atom in motion sees radiation which is frequency shifted from the laboratory frame. Several other systematics effects have to be taken into account; for example frequency shifts are caused by relativistic effects (second order Doppler shift and gravitational time dilatation), collisions between atoms, magnetic and electric fields both static (Zeeman effect and Stark effect) and from electromagnetic radiation (light shift). One particular case of light shift is caused by blackbody radiation of the [6]. This is why in 1997 it has been specified that the definition of the SI second refers to a caesium atom at rest at a temperature of 0 K.

In frequency metrology, instability is commonly evaluated using the two-samples deviation or Allan deviation $\sigma_y(\tau)$ [7], expressed as a relative frequency deviation as a function of the averaging time τ. Allan deviation is well suited for measurement with counters (frequency and time interval counters) and it is thus preferred to spectral methods, especially for long averaging time. Allan deviation is a unbiased estimator for white frequency noise and, unlike the classical standard deviation, it is also a good estimator for low-frequency colored noise (e.g., flicker noise).

The fundamental limit to the instability of an atomic clock is given by quantum-projection noise [8]. Suppose an atom is prepared in the linear superposition

$$|\varphi\rangle = \alpha\,|1\rangle + \beta\,|2\rangle \tag{1.1}$$

of two states $|1\rangle$ and $|2\rangle$ and where α and β are complex numbers with $|\alpha|^2 + |\beta|^2 = 1$. According to quantum mechanics measuring whether the atom is in $|1\rangle$ or $|2\rangle$ gives as result $|1\rangle$ with probability $|\alpha|^2$. The outcome of the measurement cannot be predicted except for $|\alpha|^2 = 1$ or $|\alpha|^2 = 0$. In atomic clocks, electromagnetic radiation probes the atomic transition (microwaves are used in caesium clocks). The frequency of the radiation is tuned to be in resonance with the atoms measuring the number of atoms in $|1\rangle$ or $|2\rangle$. If N atoms are measured frequency fluctuations scales as $1/\sqrt{N}$ and for a cycle time τ_c the quantum-projection-noise limit is approximately [9]

$$\sigma_y(\tau) \simeq \frac{\mathit{\Delta}\nu}{\nu_0}\frac{1}{s/n} \simeq \frac{\mathit{\Delta}\nu}{\nu_0}\sqrt{\frac{\tau_\mathrm{c}}{N\tau}} \tag{1.2}$$

where ν_0 is the oscillator frequency, $\mathit{\Delta}\nu$ the linewidth of the transition, and s/n is the signal-to-noise ratio for τ averaging time. Equation (1.2) scales as the inverse of the quality factor of the transition $Q = \nu_0/\mathit{\Delta}\nu$ and improves increasing the number of atoms. The linewidth of the transition is Fourier limited by the finite interaction time T between the radiation and the atoms $\mathit{\Delta}\nu \simeq 1/T$. A stabler clock is thus obtained increasing the interaction time.

In caesium clock atoms are probed while moving in a microwave cavities. Larger cavities would make longer interaction time but can lead to other technical difficulties. A technique for increasing the interaction time was introduced by Ramsey in 1950 [10]; two shorts interactions with microwave pulses are used, separated by a dark time T_R. The linewidth depends on the long dark time $\mathit{\Delta}\nu \simeq 1/T_\mathrm{R}$. The Nobel Prize in Physics 1989 was awarded to Norman Ramsey for his invention of the separated oscillatory fields method and its use in atomic clocks.

Another strategy to increase the interaction time is to slow the atoms, so that they can stay in the microwave cavity for a longer time. This has been possible since 1995 thanks to the introduction of laser cooling and trapping [11] for which Steven Chu, Claude Cohen-Tannoudji, and William Phillips won the Nobel Prize in Physics 1997. Since slow atom falls under gravity in the interaction cavity, a fountain geometry is used: atoms are cooled and launched vertically in the microwave region and, when they fall back, they pass again in the microwave cavity thus achieving a Ramsey interrogation scheme.

The SI second is now realized by microwave caesium frequency standards with a fractional frequency uncertainty $\delta\nu/\nu \approx 10^{-15}$, with the best caesium fountain clocks reaching 3×10^{-16} [12]. Preliminary results with next-generation cryogenic fountains [13] approach a fractional uncertainty 1×10^{-16}. The typical instability for a caesium frequency standard is $\sigma_y(\tau) \simeq 1 \times 10^{-13}/\sqrt{\tau/(1\,\mathrm{s})}$, but this greatly depends on the noise of the local oscillator. Instability limited by quantum projection noise has been achieved with ultrastable oscillators [14].

1.2 Optical Frequency Standards

Equation (1.2) suggests that a transition with a higher frequency ν_0 can achieve a lower clock instability. Moving from the microwave domain ($\nu_0 \sim 10^{10}\,\mathrm{Hz}$) to optical domain ($\nu_0 \sim 5 \times 10^{14}\,\mathrm{Hz}$) can in principle lead to a great reduction in instability. Intuitively this corresponds to a much finer measurement like, for example, measuring a length with a ruler marked every millimetres instead of every centimetres. Laser stabilized on optical transitions are thus interesting as optical frequency standards (colloquially known as optical clocks, even if they have not yet contributed to time scales unlike the microwave counterpart).

Soon after the realization of lasers in 1960 scientists realized that laser frequency can be stabilized on molecular transitions, for example of methane (CH_4) or iodine (I_2). The laser frequency has to be measured respect to the caesium standard, whose frequency is orders of magnitude smaller. The first important frequency measurement of a methane-stabilized helium-neon laser (at 3.39 µm) was accomplished by Evenson et al. in 1972 [15]. The measurement was based on a chain of harmonic multiplication steps from the caesium frequency (9 GHz) to the laser frequency (88 THz). The chain relied on different intermediate microwave and far-infrared sources used as transfer oscillators. The efforts on the frequency measurement of the methane-stabilized helium-neon laser, together with the measurement of its wavelength, led to the measurement of the speed of light [16]. The value of the speed of light was eventually assumed constant $c = 299\,792\,458\,\mathrm{m/s}$ as the base of the definition of the metre in 1983 [3]. The first frequency measurement with visible wavelengths were performed later in 1983 [17, 18].

Research on optical frequency standards shown a major advance in the last decade when several critical technologies reached maturity [19, 20]. Different neutral atoms or ions have been recognized to have a narrow optical transition, suitable to act as reference and with reduced sensitivity to perturbations (clock transition). The first critical technology is laser cooling and trapping of atoms or ions. Laser cooling and trapping allows long interaction time and is fundamental to mostly suppress the Doppler shift that affects the accuracy of clocks. The second is the stabilization of laser frequency on high-finesse Fabry-Pérot cavities [21], needed to probe the narrow clock transitions and for high-resolution spectroscopy. The third is non-linear optics [22], that is often exploited to generate the wanted wavelengths.

One last fundamental invention made widespread the metrological investigation of optical transitions. The introduction of the optical frequency comb in 1999 [23] made possible to directly and reliably scale a frequency measurement in the optical domain to a measurement in the microwave domain, avoiding complicated harmonic chains. Nobel Prize in Physics 2005 was awarded to John Hall and Theodor Hänsch for the optical frequency comb technique and for their contributions to laser-based precision spectroscopy. The optical frequency comb lasers emit a periodic train of short pulses. Their spectrum corresponds to a series (comb) of distinct sharp lines whose frequencies are given by

$$f_N = N f_\mathrm{R} + f_0, \tag{1.3}$$

where N is an integer, f_R is the pulse repetition rate and f_0 is a common offset [24–26]. Determining an absolute optical frequencies with the comb requires 3 radio frequency (RF) frequencies, f_R, f_0, and the beat note frequency between the laser under test and the closest tooth of the comb. The RF frequencies are readily measured against the caesium standard and eq. (1.3) is used to scale the optical frequency.

Figure 1.1 shows the fractional frequency uncertainty of optical frequency standards from the first measurement of the methane-stabilized laser in 1972 to 2012. The figure highlights the rapid decrease in uncertainty in the years following the comb introduction, that has now surpassed the uncertainty in state-of-the-art microwave caesium clocks. Absolute frequency measurement of optical transitions respect to the SI cannot have uncertainty lower that that of the reference, that is that of the caesium clocks, but in some cases the contribution coming from the optical clock has been evaluated lower than the contribution of the caesium reference. Frequency ratios coming from direct comparison of optical frequencies have dimension one and their uncertainty does not depend on the realization of SI units. Two major researches have been developed: optical clocks based on single trapped ions and optical clocks based on neutral atoms trapped in an optical lattice. A critical aspect of clocks based on trapped ions and atoms in an optical lattice is the suppression of the Doppler and photon recoil effects. Generally, if an atom or ion is confined tightly during the interaction time, in a space much shorter than the clock wavelength, all motion effects are mostly suppressed (Lamb-Dicke regime [27]).

Ion traps are obtained using a combination of static and oscillating electric fields. A single ion can be cooled while trapped [28, 29]. Ions are probed in the bottom of the trap, where the trapping fields are zero, and where systematics shifts are suppressed or well controlled. Ion optical frequency standards have been developed in several national metrology institutes with mercury Hg^+ [30], aluminum Al^+ [31, 32], strontium Sr^+ [33, 34] and ytterbium Yb^+ [35]. Ion clocks show unprecedented accuracy [32] because a simple quantum system is used (the single ion) but the signal-to-noise ratio is limited in eq. (1.2) because only one ion is trapped to avoid interactions between different charged particles. State-of-the-art ion clocks show uncertainty well below 1×10^{-16}, with a notably example below 1×10^{-17} [32]. Wolfgang Paul and Hans Dehmelt were awarded the Nobel Prize in Physics 1989 for the development of the ion trap while David Wineland shared the last Nobel Prize in Physics (2012) for his work with ion systems.

The approach is different with neutral atoms. Large number of neutral atoms can be trapped and cooled to millikelvin temperatures or below in a magneto-optical trap (MOT) exploiting the combined force from a magnetic field gradient and light pressure [11]. Unfortunately the light shift from the trapping laser greatly perturbs the state of the atoms. One strategy to overcome this problem is releasing the atoms from the trap and probing them during free fall; Doppler and recoil shifts are partially suppressed with interferometric techniques but the interaction time is limited by gravity. Standards based on this technique has been successfully implemented with calcium atoms [36].

Alternatively, neutral atoms cooled in a MOT can be trapped in an optical lattice: atoms are trapped in the periodic potential made by a retro-reflected laser (standing wave). The optical lattice strongly perturbs the atoms but, as originally proposed by Katori et al. in 2003 [37], the details of the lattice can be properly chosen so that the energy changes on the two clock levels are the same. In particular the wavelength of the optical lattice can be tuned at a “magic” wavelength for which the clock transition is unperturbed at the first order. Optical lattice clock are presently developed worldwide based on strontium [38–41], magnesium [42], mercury [43] and ytterbium atoms [44–49]. State-of-the-art optical clocks based on optical lattice show uncertainty at the 10^{-16} level (see fig. 1.1) An uncertainty of few parts in 10^{-17} seems achievable in the next years.

1.3 Ytterbium frequency standards

Ytterbium is a rare earth element of the lanthanide series (see its position in the periodic table in fig. 1.2). Optical lattice clock based on ytterbium are being studied and developed at National Institute of Standards and Technology (NIST) [44, 45], at the National Metrology Institute of Japan (NMIJ) [46, 48], at the Korea Research Institute of Standards and Science (KRISS) [49], at the University of Düsseldorf [53] and at INRIM [47]. It has several stable isotopes that makes it an interesting element for several atomic physics experiments like parity non-conservation measurement [54], Bose-Einstein condensation [55], degenerate Fermi gases [56], bosonic-fermionic system [57], and quantum information [58].

Ytterbium has two electrons in the external shell and its spectrum is divided between spin singlet and spin triplet states, similarly to helium and alkaline earths elements. It is easy to cool and trap in a double stage MOT. Millions of ytterbium atoms can be cooled at millikelvin temperature using a MOT on the strong blue transition between spin singlet states ${}^1\mathrm{S}_0{-}{}^1\mathrm{P}_1$ at 399 nm (see fig. 1.3). A second stage cooling can be performed with a green MOT on the narrower intercombination transition ${}^1\mathrm{S}_0{-}{}^3\mathrm{P}_1$ at 556 nm, that can achieve a temperature of the order of few microkelvin. The forbidden clock

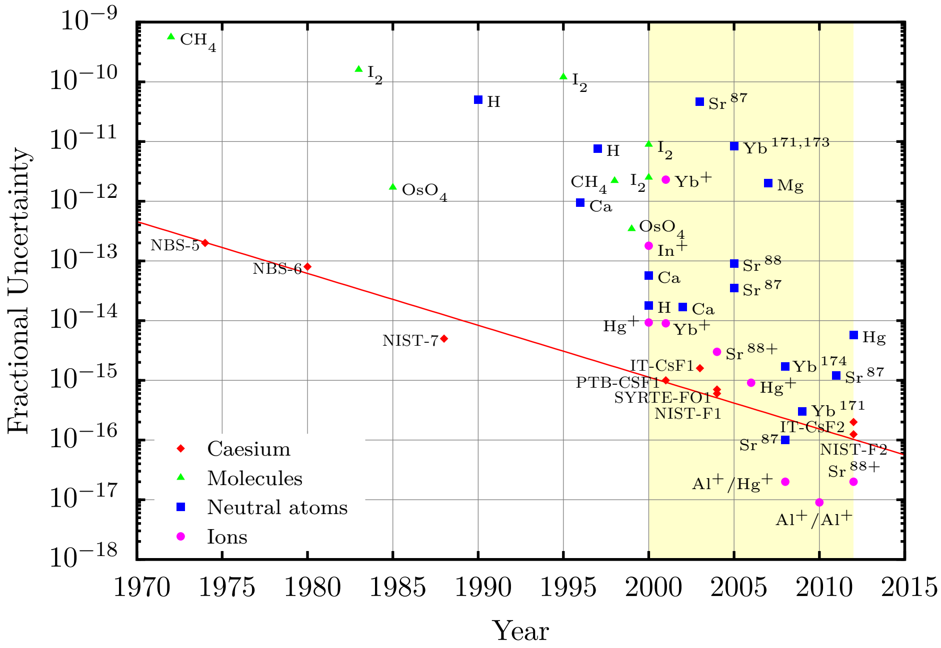

Figure 1.1: Comparison between the fractional frequency uncertainty of state-of-the-art caesium microwave clocks and that of optical frequency measurements made with transitions in molecules, neutral atoms or ions. The yellow region highlights measurements made after the introduction of optical frequency combs. Data for caesium clocks are from [12, 50]. Some of the optical measurement data are collected in [51]. Recent results come from the original works, some of which can be found in the bibliography [30–34, 38, 39, 41–45, 52].

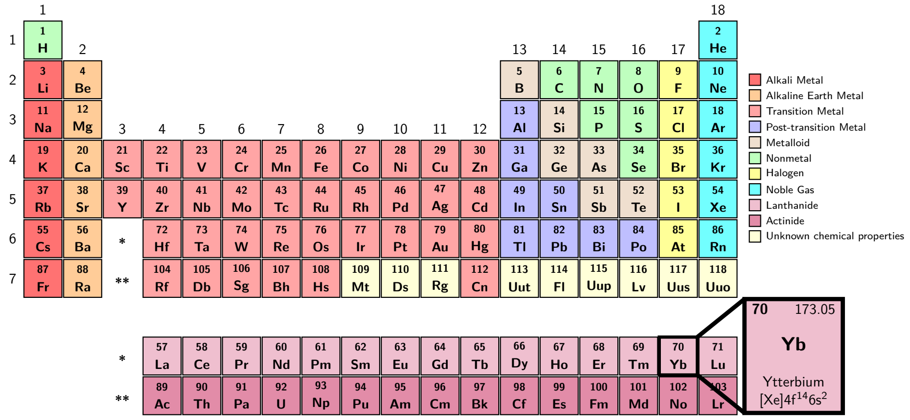

	1	2	3	4	5	6	7	8	9	10	11	12	13	14	15	16	17	18
1	1 H																	2 He
2	3 Li	4 Be											5 B	6 C	7 N	8 O	9 F	10 Ne
3	11 Na	12 Mg											13 Al	14 Si	15 P	16 S	17 Cl	18 Ar
4	19 K	20 Ca	21 Sc	22 Ti	23 V	24 Cr	25 Mn	26 Fe	27 Co	28 Ni	29 Cu	30 Zn	31 Ga	32 Ge	33 As	34 Se	35 Br	36 Kr
5	37 Rb	38 Sr	39 Y	40 Zr	41 Nb	42 Mo	43 Tc	44 Ru	45 Rh	46 Pd	47 Ag	48 Cd	49 In	50 Sn	51 Sb	52 Te	53 I	54 Xe
6	55 Cs	56 Ba	*	72 Hf	73 Ta	74 W	75 Re	76 Os	77 Ir	78 Pt	79 Au	80 Hg	81 Tl	82 Pb	83 Bi	84 Po	85 At	86 Rn
7	87 Fr	88 Ra	**	104 Rf	105 Db	106 Sg	107 Bh	108 Hs	109 Mt	110 Ds	111 Rg	112 Cn	113 Uut	114 Fl	115 Uup	116 Lv	117 Uus	118 Uuo

*	57 La	58 Ce	59 Pr	60 Nd	61 Pm	62 Sm	63 Eu	64 Gd	65 Tb	66 Dy	67 Ho	68 Er	69 Tm	70 Yb	71 Lu
**	89 Ac	90 Th	91 Pa	92 U	93 Np	94 Pu	95 Am	96 Cm	97 Bk	98 Cf	99 Es	100 Fm	101 Md	102 No	103 Lr

- Alkali Metal
- Alkaline Earth Metal
- Transition Metal
- Post-transition Metal
- Metalloid
- Nonmetal
- Halogen
- Noble Gas
- Lanthanide
- Actinide
- Unknown chemical properties

70 173.05
Yb
Ytterbium
$[Xe]4f^{14}6s^2$

Figure 1.2: Position of ytterbium in the periodic table of elements.

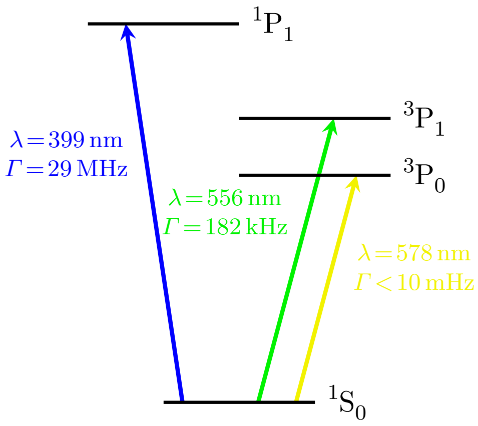

Figure 1.3: Low-lying levels of ytterbium relevant for the optical clock.

transition $^1S_0$–$^3P_0$ to the triplet metastable state $^3P_0$ is yellow at 578 nm (518 THz). The magic wavelength of the optical lattice for ytterbium is 759 nm.

The spectroscopy of the clock transition requires a laser at 578 nm frequency-stabilized to an ultrastable Fabry-Pérot cavity. The frequency of the laser can be locked to the ytterbium transition and then measured with respect to the SI second using an optical frequency comb.

Figure 1.4 shows the relation between the ytterbium optical lattice clock and other frequency standards at INRIM. INRIM maintains two caesium primary frequency standards, the fountain IT-CsF1 [59] and the cryogenic fountain IT-CsF2 [13] that realize the definition of the SI second. INRIM also has three hydrogen masers, and five commercial caesium clocks used for the generation of the Italian national time scale. The optical frequency comb will be used to measure the frequency of a cavity-stabilized laser at 578 nm [60] locked to ytterbium atoms with respect to the microwave clocks. The comb can also be used for a direct comparison between optical clocks. At INRIM it will be used to reference a cavity-stabilized laser at telecom wavelength 1542 nm [61, 62]. This laser will be used in a noise-compensated optical fiber link for remote optical frequency dissemination and comparison between INRIM and other laboratories [63], namely the strontium clock developed at European Laboratory for Non-Linear Spectroscopy (LENS) in Florence [40].

Several optical transitions are recommended as secondary representations of the SI second. The unperturbed optical clock transition of ytterbium ^{171}Yb neutral atom has been recently recommended as secondary representations of the second in December 2012 [64] to reflect the recent measurements made at NIST and at NMIJ. Its frequency is $\nu_{^{171}\mathrm{Yb}} = 518\,295\,836\,590\,865.0\,\mathrm{Hz}$ with an estimated relative standard uncertainty of 2.7×10^{-15}.

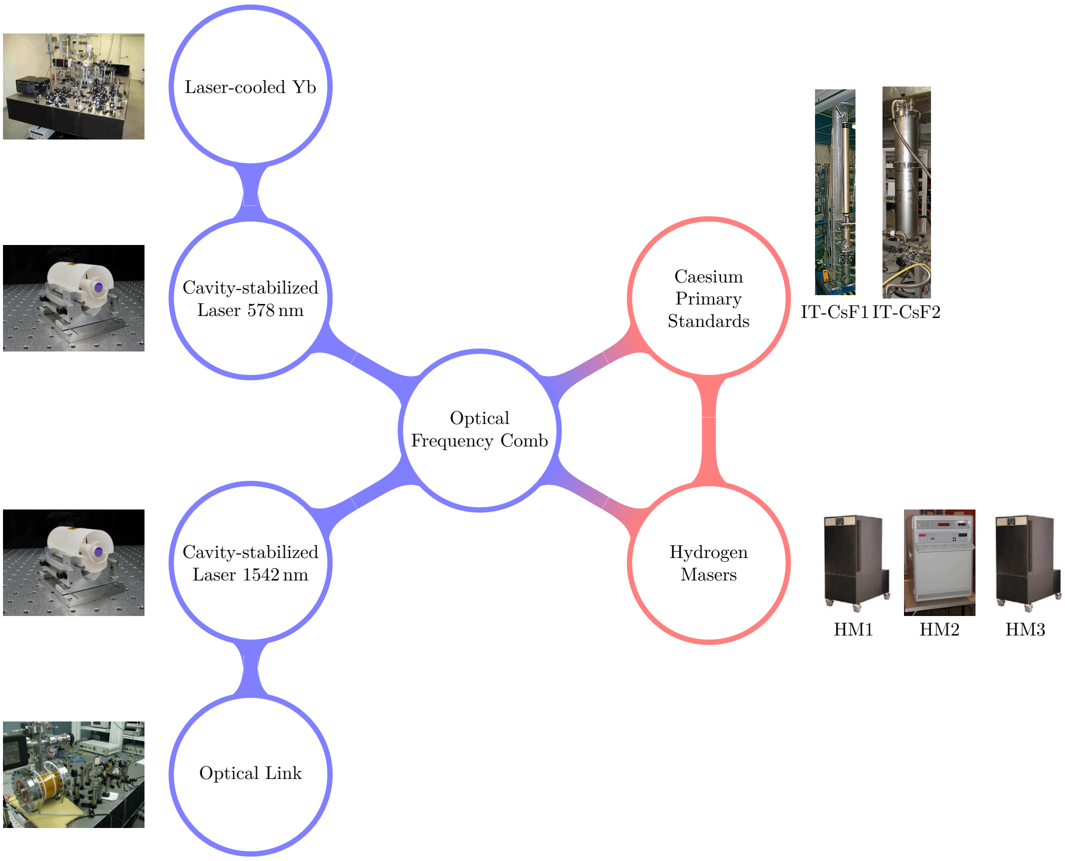

Figure 1.4: INRIM clocks ensemble

1.4 Thesis outline

The thesis is organized as follows.

A theoretical background on cooling and trapping of neutral atoms is given in chapter 2. In chapter 3, I give some details on the properties of ytterbium.

Most of my work for this thesis was done at INRIM where a ytterbium optical clock is being developed. In chapter 4, I describe the generation of the lasers needed for the experiment and the techniques of non-linear optics needed for the generation of the various wavelengths (399 nm, 556 nm and 578 nm). In chapter 5, I described the details of the stabilization and the characterization of the clock laser at 578 nm. Chapter 6 reports the experimental observation of the second-stage MOT at 556 nm. A new experimental setup for the INRIM clock is soon to be realized. The detail of the design of the new apparatus are in chapter 7.

During my Ph.D. I have been guest researcher at NIST for six months. In chapter 8, I give some details of the NIST ytterbium optical clock.

2 Cold neutral atoms

I will give here some theoretical details on laser cooling and trapping of neutral atoms. Light can excerpt two forces on atoms. The first is radiation pressure force that comes from the photon momentum and it is useful for cooling and trapping in a MOT. The second is the dipole force that come from the light shift of the energy levels and it is exploited in optical lattices.

2.1 Radiation pressure force

The radiation pressure force on a neutral atom in a near resonant laser field is given by [11]

$$\boldsymbol{F} = \frac{\hbar \boldsymbol{k} \gamma}{2} \frac{I}{I_{\mathrm{s}}} \frac{1}{1 + \frac{I}{I_{\mathrm{s}}} + (2(\delta - \boldsymbol{k} \cdot \boldsymbol{v})/\gamma)^2}, \tag{2.1}$$

where $\hbar$ is the reduced Planck constant, the laser radiation has wavevector $\boldsymbol{k}$, intensity I and detuning δ from the atomic resonance, γ is the linewidth of the atomic transition, $I_{\mathrm{s}} = \hbar c k^3 \gamma/(12\pi)$ is the saturation intensity, and $\boldsymbol{v}$ the velocity of the atom. Equation (2.1) can be interpreted as the photon momentum $\hbar \boldsymbol{k}$ times a lorentzian rate of absorption, shifted by the Doppler effect $\boldsymbol{k} \cdot \boldsymbol{v}$. It should be noted that this force arises from absorption followed by spontaneous emission but since spontaneous emission is isotropic its effect averages out and the result is a net force along $\boldsymbol{k}$.

The radiation pressure force depends on the velocity of the atoms because the Doppler effect changes the effective detuning of the laser $\delta \to \delta - \boldsymbol{k} \cdot \boldsymbol{v}$. When the laser is detuned towards the red ($\delta < 0$) photons are adsorbed preferably by atoms moving towards them ($\boldsymbol{k} \cdot \boldsymbol{v} < 0$); atoms are then slowed down by the radiation pressure. Under these conditions the spontaneous emitted photons are at higher frequency that the adsorbed ones and the atoms lose energy in the process. This is then a dissipative force and a laser can be used to slow down an atomic beam [65].

When two counter-propagating red-detuned laser beams are used, both detuned towards the red, atoms are slowed down in both directions and the atoms are cooled by the radiation pressure (optical molasses) [28, 66]. Six counter-propagating laser beams can cool the atoms in all directions.

2.2 Magneto-optical traps

The principle of a MOT is similar but the laser-atom detuning depends also on the position because of the magnetic field gradient applied. Consider only a one-dimensional case and an atomic transitions with $J_\mathrm{g} = 0 \to J_\mathrm{e} = 1$, where $J_\mathrm{g,e}$ are the total electronic angular momentum of the ground and excited levels.

The force on the atoms from two counterpropagating laser beams can be written

$$F = F_+ + F_-, \tag{2.2}$$

where

$$F_\pm = \pm \frac{\hbar k \gamma}{2} \frac{I/I_s}{1 + 2I/I_s + (2\delta_\pm/\gamma)^2}. \tag{2.3}$$

The factor 2 in the denominator takes into account the power broadening from both beams. The detunings for the two beams are

$$\delta_\pm = \delta \mp kv \pm \frac{\mu' B}{\hbar}, \tag{2.4}$$

where B is the magnetic field and μ' is the magnetic dipole moment of the transition and the sign is chosen by the polarization of the two beams ($\sigma_+\sigma_-$ configuration). For a constant magnetic field gradient the magnetic field depends on space $B(x) = Ax$ and the situation is depicted in fig. 2.1. In fact the excited level is splitted by the magnetic field in the three state with angular projection along the field $M_\mathrm{e} = -1, 0, +1$. A σ_+ beam only drives the transition between the ground state ($M_\mathrm{g} = 0$) and the excited state with $M_\mathrm{e} = +1$. The opposite is true for the σ_- beam. For $B > 0$ the state $M_\mathrm{e} = -1$ is shifted down while the state $M_\mathrm{e} = +1$ is shifted up. State $M_\mathrm{e} = 0$ is not shifted. So, for example, an atom on the right side of fig. 2.1, scatters more atoms from the σ_- beam coming from the left and it is drived toward the center of the MOT.

Equation (2.3) can be expanded in Taylor series for small v and x

$$F \simeq -\beta v - \kappa x, \tag{2.5}$$

with the damping coefficient

$$\beta = -\frac{8\hbar k^2 I/I_\mathrm{s} \delta}{\gamma(1 + 2I/I_\mathrm{s} + (2\delta/\gamma)^2)} \tag{2.6}$$

and the spring constant

$$\kappa = \frac{\mu' A}{\hbar k} \beta. \tag{2.7}$$

For red detuning of the laser eq. (2.5) describe a harmonic force with friction and thus result in both cooling and trapping of the atoms.

There are two temperature scale relevant for MOTs; the Doppler temperature is $T_\mathrm{D} = \hbar\gamma/(2k_\mathrm{B})$ and the recoil temperature $T_\mathrm{r} = \hbar^2 k^2/(M k_\mathrm{B})$. The Doppler temperature scales as the width of the transition while the recoil temperature is related to the energy increase of an atom that absorbs a single photon with momentum $\hbar k$. The temperature of atoms under the force of eq. (2.5) can be calculated considering the cooling from energy dissipation and the heating from photon recoils [67]. The damping force in eq. (2.5) causes a loss of energy

$$\left.\frac{\mathrm{d}E}{\mathrm{d}t}\right|_\mathrm{cool} = -Fv = -\beta v^2. \tag{2.8}$$

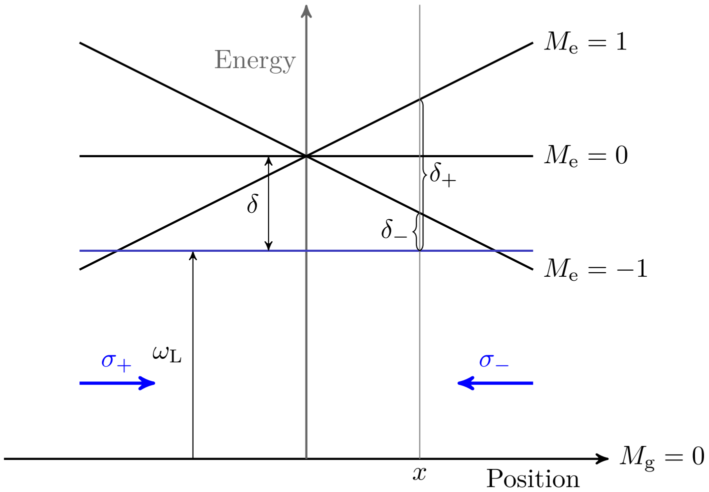

Figure 2.1: Scheme for a 1D MOT.

The heating from photon recoils goes as the scattering rate (with $kv \ll \delta$)

$$\left.\frac{\mathrm{d}E}{\mathrm{d}t}\right|_{\mathrm{heat}} = \frac{\hbar^2 \boldsymbol{k}^2}{M} \frac{I/I_\mathrm{s}}{[1 + \frac{I}{I_\mathrm{s}} + (2\delta/\gamma)^2]^2}. \tag{2.9}$$

At equilibrium the two should result in no net energy change $\mathrm{d}E/\mathrm{d}t|_{\mathrm{cool}} + \mathrm{d}E/\mathrm{d}t|_{\mathrm{heat}} = 0$, resulting in an equation for v^2, and thus a temperature ($k_\mathrm{B}T/2 = 1/2mv^2$)

$$T = \frac{\hbar\gamma}{8k_\mathrm{B}} \frac{\gamma}{|\delta|} \left[1 + \frac{I}{I_\mathrm{s}} + (2\delta/\gamma)^2\right]. \tag{2.10}$$

This temperature has a minimum for $I/I_\mathrm{s} \ll 1$, $\delta = -\gamma/2$, when its value is the Doppler temperature $T_\mathrm{D} = \hbar\gamma/(2k_\mathrm{B})$.

For real atoms this two-levels picture is usually insufficient; in the presence of splitting of the levels other cooling mechanism exists that results in temperatures lower than the Doppler limit[11, 68]. Sub-Doppler cooling techniques exploits the strong coupling between the electronic and motional degrees of freedom caused by optical pumping process that have an effective narrower linewidth and can achieve lower temperatures. The recoil temperature cannot be surpassed with a mechanism that relies on spontaneous emission.

2.3 Dipole force

Consider a two-level atom with a transition of frequency ω_0 and linewidth γ. The atom in a light field with frequency ω_L and amplitude $\mathcal{E}_0$ are perturbed and experience a shift of the transition frequency (light shift or AC Stark shift) [69]

$$\mathit{\Delta}\omega = -\frac{2\mathit{\Omega}^2\omega_0}{(\omega_\mathrm{L}^2 - \omega_0^2)} \tag{2.11}$$

where $\mathit{\Omega} = -\rho\mathcal{E}_0/\hbar$ is the Rabi frequency, with ρ the dipole moment for the transition. The Rabi frequency can be rewritten in term of the intensity $I = \mathcal{E}_0^2$ as [11]

$$|\mathit{\Omega}|^2 = I\frac{3\lambda^3\gamma}{4\pi^2\hbar c}, \tag{2.12}$$

where λ is the wavelength of the transition and c the speed of light. In this approximation (valid for $|\mathit{\Omega}| \ll |\delta| = |\omega_\mathrm{L} - \omega_0|$) the shift is proportional to the intensity of the light. We write

$$\mathit{\Delta}\omega = -\frac{1}{2\hbar}\alpha_0\mathcal{E}_0^2, \tag{2.13}$$

where

$$\alpha_0 = \frac{2|\rho|^2}{\hbar}\frac{\omega_0}{\omega_0^2 - \omega_\mathrm{L}^2} \tag{2.14}$$

is the dipole polarizability.

For a multi-level atom the shift of a state $|j\rangle$ is given by the sum on every dipole allowed transitions

$$\alpha_j = \sum_k \frac{2|\rho_{jk}|^2}{\hbar}\frac{\omega_{jk}}{\omega_{jk}^2 - \omega_\mathrm{L}^2}, \tag{2.15}$$

$$\mathit{\Delta}\omega_j = -\frac{1}{2\hbar}\alpha_j\mathcal{E}_0^2, \tag{2.16}$$

where k labels the different states of the atom, ω_{jk} is the transition frequency between the states $|j\rangle$ and $|k\rangle$ and ρ_{jk} is their dipole matrix element. The corresponding energy level shift can be exploited to confine the atoms in a non-uniform light field. In a classical analogy, the dipole moment induced by an electric field is $\boldsymbol{\rho} = \alpha\boldsymbol{E}$ and the interaction energy between the dipole and the field is $U = -\boldsymbol{\rho}\cdot\boldsymbol{E}$. For an induced dipole $\boldsymbol{\rho} = \alpha\boldsymbol{E}$ the interaction energy is actually $U = -\boldsymbol{\rho}\cdot\boldsymbol{E}/2$, and for a scalar polarizability $U = -\alpha E^2/2$. In a non-uniform field this energy results in a force $\boldsymbol{F} = -\boldsymbol{\nabla}U = \alpha\boldsymbol{\nabla}E^2$. This force is conservative and thus it can only trap atoms but cannot cool them. Atoms must be cold before being loaded in a dipole trap because the trap depth is usually small (few microkelvins). Atoms can be further cooled while in the dipole trap with other techniques (e.g., sideband cooling).

2.4 Optical lattice

A 1D optical lattice can be obtained in a standing wave (along z)

$$\begin{aligned}\boldsymbol{E} &= \mathcal{E}_0\boldsymbol{e}\exp\left[-\mathrm{i}(\omega_\mathrm{L}t + k_\mathrm{L}z)\right] + \mathcal{E}_0\boldsymbol{e}\exp\left[-\mathrm{i}(\omega_\mathrm{L}t - k_\mathrm{L}z)\right), &(2.17)\\ &= 2\mathcal{E}_0\boldsymbol{e}\exp\left[-\mathrm{i}\omega_\mathrm{L}t\right]\cos(k_\mathrm{L}z), &(2.18)\end{aligned}$$

where ω_L and k_L are the frequency and wavevector of the lattice and $\boldsymbol{e}$ is the polarization vector. By light shift of the energy levels the standing wave gives a potential with the space dependency for an atom in the state $|j\rangle$.

$$U(z) = -\alpha_j\mathcal{E}_0^2\cos^2(k_\mathrm{L}z) = -U_0\cos^2(k_\mathrm{L}z), \tag{2.19}$$

where U_0 is the peak trap depth. For $\alpha_j > 0$ atoms are trapped in the maxima of the standing wave.

The periodic potential in eq. (2.19) gives in general a band structure as well known from solid state physics [70]. However, from a frequency standard point of view, we are interested in the case of deep lattice when the band structure is unimportant and each atom is substantially confined in a single potential well where it can be probed in the Lamb-Dicke regime.

This confinement is valid only in the longitudinal direction. A weaker trap is obtained in the transverse direction r using a Gaussian profile [71] for the lattice laser. Near the waist of the Gaussian beam the potential is then

$$U(z, r) = -U_0 \mathrm{e}^{-2r^2/w_0^2} \cos^2(k_\mathrm{L} z), \tag{2.20}$$

where w_0 is the beam waist radius.

In the deep lattice approximation eq. (2.20) can be approximated as a harmonic potential around a minimum

$$U(z, r) \simeq U_0 \left(k_\mathrm{L}^2 z^2 + \frac{2r^2}{w_0^2} \right) = \frac{1}{2} M \omega_z z^2 + \frac{1}{2} M \omega_r r^2 \tag{2.21}$$

where M is the mass of the atom, ω_z, ω_r are the normal mode frequencies. I have neglected higher order terms. It is convenient to give the trap depth in unit of the lattice recoil energy $E_\mathrm{r} = \hbar^2 k_\mathrm{L}^2/M$. The harmonic frequencies are then

$$\omega_z = \sqrt{\frac{2U_0 k^2}{M}} = 2/\hbar \sqrt{U_0 E_\mathrm{r}}, \tag{2.22}$$

$$\omega_r = \sqrt{\frac{2U_0}{M w_0^2}} = \frac{1}{k_\mathrm{L} w_0} \omega_z. \tag{2.23}$$

In this approximation the longitudinal potential gives rise to the well known energy spectrum for a harmonic oscillator

$$E_n = \hbar \omega_z (n + 1/2), \tag{2.24}$$

where n is an integer (vibrational quantum number).

2.5 Magic wavelength

The potential depth for a lattice at frequency ω_l on an atom in the state $|j\rangle$ is (eq. (2.19))

$$U_{0j} = -\alpha_j(\omega_\mathrm{L}) \mathcal{E}_0^2. \tag{2.25}$$

Consider a transition from the ground to an excited state with frequency ω_0 (such as the clock transition). The frequency of the transition is shifted by the lattice to

$$\omega = \omega_0 - \frac{1}{4\hbar} \Delta\alpha(\omega_\mathrm{L}, \boldsymbol{e}) \mathcal{E}_0^2 + \frac{1}{64\hbar} \Delta\gamma(\omega_\mathrm{L}, \boldsymbol{e}) \mathcal{E}_0^4 - \ldots, \tag{2.26}$$

where $\mathit{\Delta}\alpha(\omega_{\mathrm{L}},\boldsymbol{e}) = \alpha_{\mathrm{e}}(\omega_{\mathrm{L}},\boldsymbol{e}) - \alpha_{\mathrm{g}}(\omega_{\mathrm{L}},\boldsymbol{e})$ and the frequency dependence is given by eq. (2.15). In general it depends on the frequency of the lattice laser ω_{L} and on its polarization state $\boldsymbol{e}$. The higher order contributions comes from interaction with two photons and $\mathit{\Delta}\gamma$ is the differential hyperpolarizability between the ground and excited state.

For the clock transition $^1\mathrm{S}_0$–$^3\mathrm{P}_0$ both ground and excited state have total angular momentum $J = 0$ so that their polarizability have the same dependence on polarization,at least at first order. For the clock transition of atoms used in optical clocks a lattice frequency exists $\omega_{\mathrm{L}} = \omega_{\mathrm{magic}}$ for which $\alpha_{\mathrm{e}}(\omega_{\mathrm{magic}}) = \alpha_{\mathrm{g}}(\omega_{\mathrm{magic}})$. Figure 2.2 shows this crossing at the magic wavelength for ytterbium. This allows trapping at the maximum of the standing wave for both levels $\alpha_{\mathrm{e,g}}(\omega_{\mathrm{magic}}) > 0$ but leaves the transition frequency unperturbed at the first order. Moreover the potential depth of the lattice eq. (2.25) is the same for both levels at the magic wavelength,so that both are trapped with the same characteristics (i.e., same ω_z). In this uniform-confinement regime the lattice light does not couple motion and electronic degrees of freedom. This is the situation depicted in fig. 2.3.

During clock operations the frequency of the lattice has to be tuned to this point. For a typical lattice of $500E_{\mathrm{r}}$, to control the clock shift at about 1 mHz the lattice frequency should be tuned to the magic wavelength to about 100 kHz.

The hyperpolarizability is not cancelled at the magic wavelength and its effects should be carefully controlled, for example investigating the two-photons resonances [72].

2.6 Lamb-Dicke regime

If probing is done on the direction of the lattice most of motional effects depend on ω_z. At the magic wavelength (in the uniform-confinement regime) the atom state can be factorized in the electronic part ($|\mathrm{e}\rangle$ or $|\mathrm{g}\rangle$ for the excited or ground state) and the motion part $|n\rangle$ in the harmonic potential. A transition can be made between $|\mathrm{g}\rangle\,|n\rangle$ and $|\mathrm{e}\rangle\,|m\rangle$ at frequency $\omega_0 + (m-n)\omega_z$. The transition could be purely electronic ($n = m$) or followed by motion excitation or de-excitation (sidebands with $m > n$ or $m < n$) The transition probability and the spectroscopy of the trapped atoms depend on the magnitude of ω_z.

If γ is the linewidth of the probing transition, for $\gamma/\omega_z \gg 1$ the atoms is in a “free-particle” regime; the sidebands are not usually resolved and a Doppler profile is obtained since we cannot discriminate purely electronic excitations (for a thermal distribution of atoms in the levels). The opposite limit $\gamma/\omega_z \ll 1$ corresponds to well-resolved sidebands; the Doppler effect is responsible for modulation frequencies around the purely electronic transition. It should be noted that despite the photon recoil and the atom motion state, in this regime the resonance occurs at the carrier ω_0 with the sidebands at $\omega_0 + (m-n)\omega_z$. Recoil and the details of the trap influence the relative line intensity between the carrier and the sidebands; the spectrum is usually asymmetric.

The Lamb-Dick regime is achieved when atoms are confined in a space much shorter than the clock wavelength. We can write the Lamb-Dicke parameter as $\eta = k_0 x_0/\sqrt{2}$,

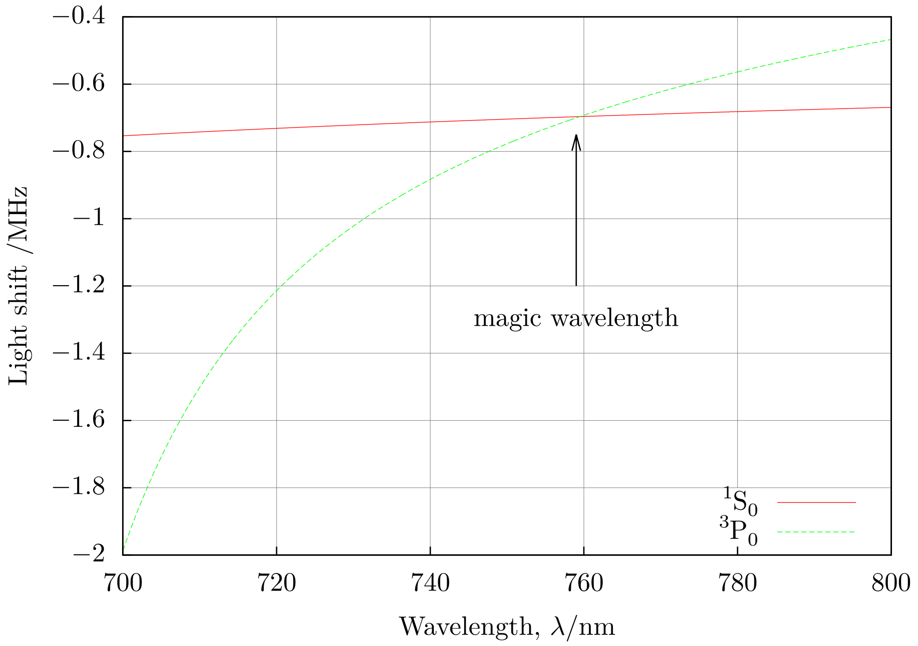

Figure 2.2: Light shift of the energy levels for the ground and excited states of the clock transition of ytterbium as a function of wavelength (laser of 1 W focused to a waist of 35 µm).

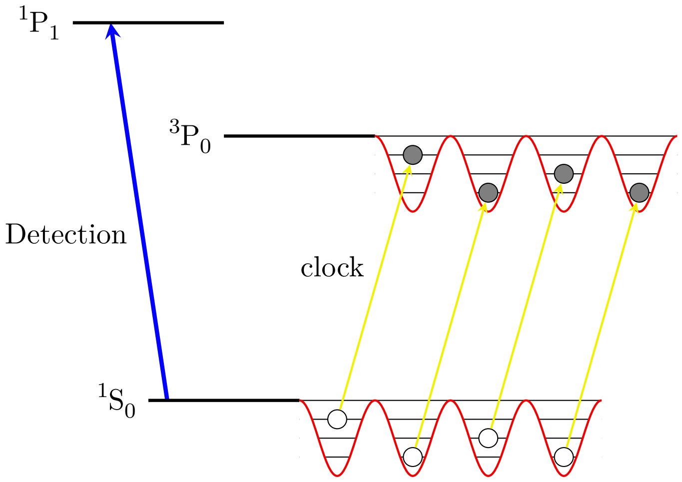

Figure 2.3: Excitation of atoms in the optical lattice.

where $k_0 = \omega_0/c$ is the wavenumber of the transition and x_0 is the size of the spatial confinement. For the ground state of a harmonic oscillator this is

$$\eta = k_0\sqrt{\frac{\hbar}{2M\omega_z}} = \sqrt{\frac{\omega_\mathrm{r}}{\omega_z}}, \tag{2.27}$$

where $\omega_\mathrm{r} = \hbar k_0^2/(2M)$ is the recoil frequency of the atom while absorbing a photon at ω_0. The Lamb-Dicke regime is achieve when

$$\eta\sqrt{\langle n+1\rangle} \ll 1, \tag{2.28}$$

where n is the vibrational quantum number. In this regime the sideband intensities are reduced respect to the carrier one and the sideband structure becomes more symmetric. The recoil energy is not taken by the atom but by the confining potential and there is no shift or broadening of the transition.

3 Ytterbium properties

Ytterbium is a chemical element with atomic number $Z = 70$ and its symbol is Yb. It is the penultimate element in the lanthanide series of the periodic table. Natural ytterbium is a mixture of seven stable isotopes, see table 3.1 [73]. The five even isotopes (^{168}Yb,^{170}Yb,^{172}Yb,^{174}Yb,^{176}Yb) are bosonic with zero nuclear spin. The two odd isotopes are fermionic with different nuclear spin (^{171}Yb with $I_{171} = 1/2$, and ^{173}Yb with $I_{173} = 5/2$). Most isotopes, except for ^{168}Yb, have relative abundance greater than 3 % and can be easily used in experiment starting from natural ytterbium.

3.1 Physical properties

Ytterbium has a density of 6.90 g/cm^3. The temperature of its melting point is 1097 K and that of its boiling point is 1469 K [74]. Ytterbium vapor pressure can be significant at temperature well below the melting point (see fig. 3.1). For example in an oven held at 673 K the vapor pressure is greater than 0.1 Pa. Moreover the vapor pressure at room temperature is much less than any ultra-high vacuum (UHV) level $< 1 \times 10^{-15}$ Pa.

3.2 Spectrum overview

Ytterbium electronic configuration is [Xe]4f^{14}6s^2. The excitation of one of the electron in the s shell give rise to an energy level structure similar to that of alkaline earth atoms like calcium (Ca) and strontium (Sr). This structure can be described by the Russell-Saunders term notation $^{2S+1}L_J$ where S is the total electronic spin quantum number, J the total electronic angular momentum quantum number, and L is the orbital quantum number in spectroscopic notation [75]. Figure 3.2 shows the term diagram of low-lying

Table 3.1: Mass, natural abundance and nuclear spin of natural occurring Yb isotopes[73].

Isotope	Mass /u	Abundance /%	Spin	Mag. Moment /μ_{N}
^{168}Yb	167.933 894	0.13	0	
^{170}Yb	169.934 759	3.05	0	
^{171}Yb	170.936 323	14.3	1/2	+0.4919
^{172}Yb	171.936 378	21.9	0	
^{173}Yb	172.938 208	16.12	5/2	−0.6776
^{174}Yb	173.938 859	31.8	0	
^{176}Yb	175.942 564	12.7	0	

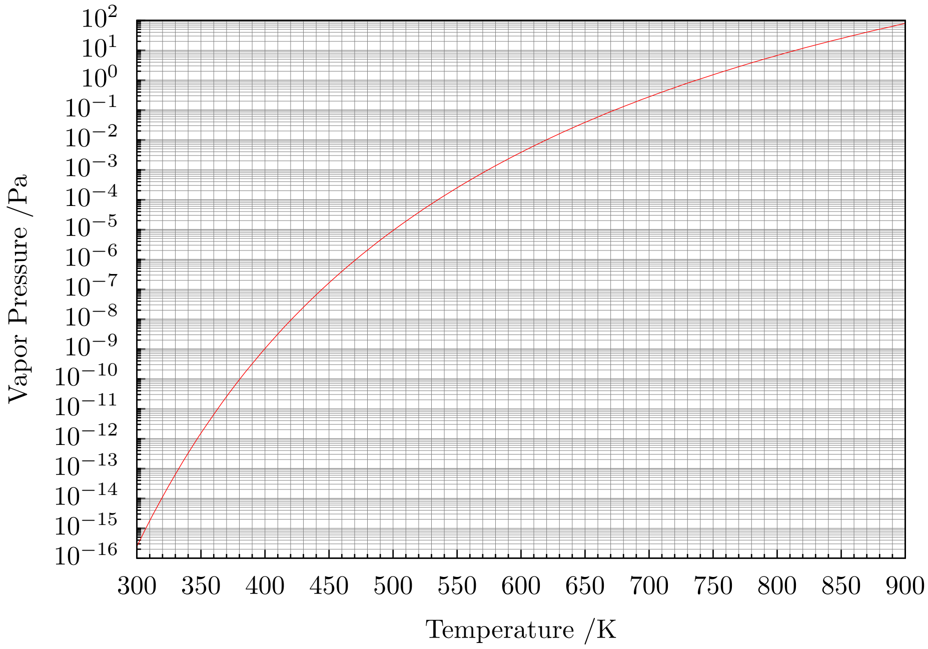

Figure 3.1: Vapor pressure of ytterbium as a function of temperature (from the formula in [74]).

levels of ytterbium. The ground state is $^1S_0$. Strong dipole allowed transitions exist from the ground state to higher lying $^1P_1$ states. The first excited levels are from the triplet term ^3P. Several dipole transitions exist between the ^3P states to ^3D and ^3S states. Radiative transitions between spin singlet and spin triplet states are forbidden because of the dipole selection rule $\Delta S = 0$. These intercombination transition are thus usually narrow and well suited as clock transitions. In ytterbium (as in strontium) one notable exception to the lack of dipole coupling between singlet and triplet state is the transition between the ground state $^1S_0$ and the excited $^3P_1$ state that, because of LS interaction, mixes with the $^1P_1$ state. The $^3P_0$ and $^3P_2$ states are metastable. Table 3.2 reports some dipole-allowed transitions of ytterbium where wavelengths are experimentally determined [76] and Einstein A coefficients are determined from the matrix elements theoretically calculated in [77].

Unlike alkaline earth atoms, in ytterbium an electron from the closed 4f shell can be excited giving rise to extra lines in the spectrum. This part of the spectrum is described in the jj coupling scheme using the notation $(J_1, J_2)_J$ [75]. The 4f-excitation threshold is shallow, at $23\,188.518\,\mathrm{cm}^{-1}$ with the $(7/2,\ 3/2)_2$ state, but it is usually neglected in theoretical calculation [77]. The state $(7/2,\ 5/2)^{\mathrm{o}}_1$ is strongly coupled with the ground state (wavelength 347 nm) and has a lifetime $\tau = 14.8(5)$ ns only 3 times larger that of the $^1P_1$ state [78].

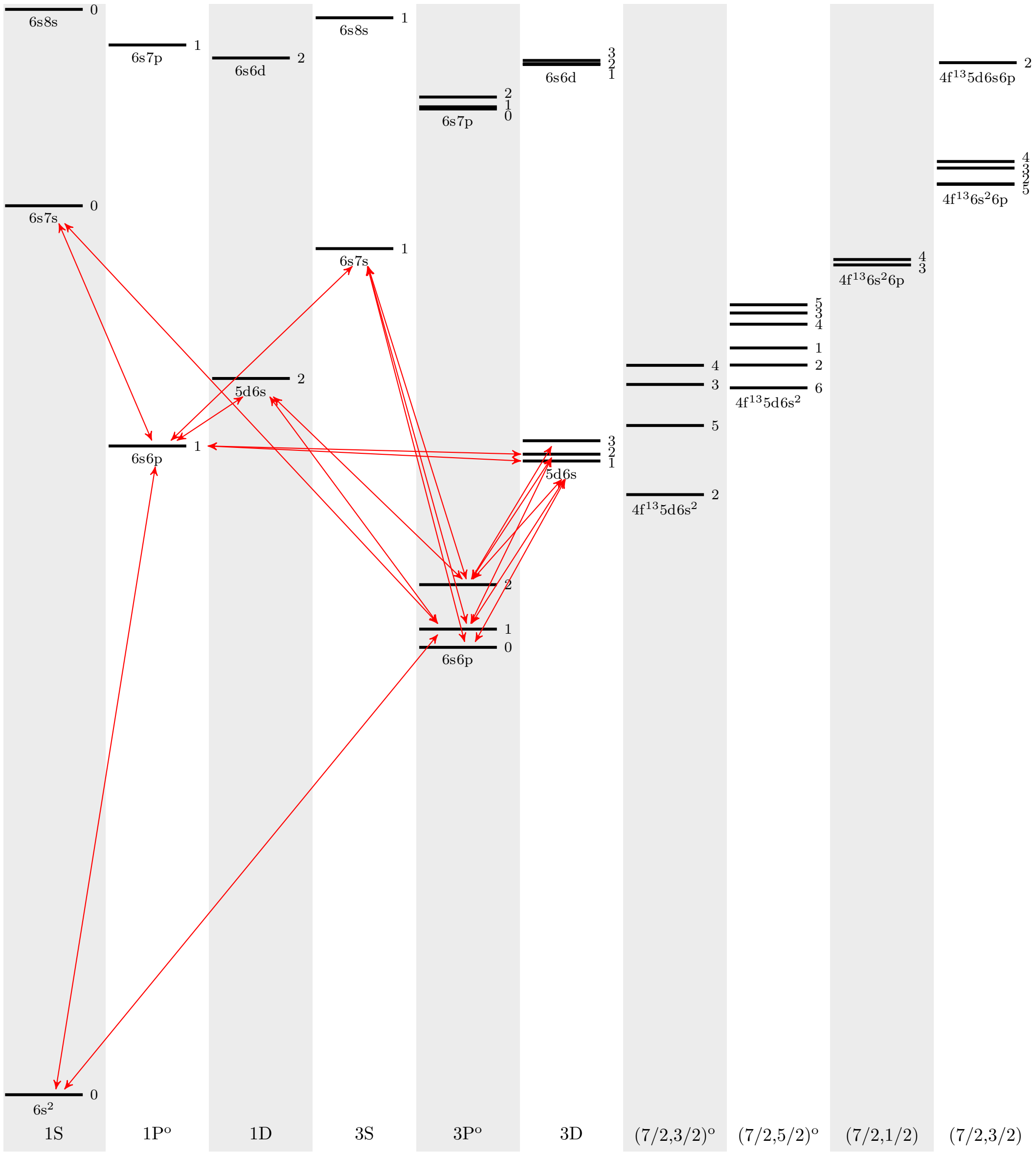

Figure 3.2: Term diagram for ytterbium. Superscript o indicates states of odd parity. Arrows mark dipole allowed transitions reported in table 3.2. Note that, for odd isotopes, further hyperfine structure is present.

Table 3.2: Wavelength [76] and Einstein A coefficient [77] of selected transition of ytterbium.

Levels		λ /nm	A /s^{-1}
6s6p $^3P_1^o$	6s^2 $^1S_0$	555.8	1.2×10^6
6s6p $^1P_1^o$	6s^2 $^1S_0$	398.9	1.8×10^8
5d6s $^3D_1$	6s6p $^3P_0^o$	1388.8	1.7×10^6
5d6s $^3D_1$	6s6p $^3P_1^o$	1539.1	9.2×10^5
5d6s $^3D_1$	6s6p $^3P_2^o$	2092.6	2.7×10^4
6s6p $^1P_1^o$	5d6s $^3D_1$	17 267.6	9.6
5d6s $^3D_2$	6s6p $^3P_1^o$	1479.3	2.0×10^6
5d6s $^3D_2$	6s6p $^3P_2^o$	1983.5	3.0×10^5
6s6p $^1P_1^o$	5d6s $^3D_2$	31 618.2	2.2
5d6s $^3D_3$	6s6p $^3P_2^o$	1798.4	1.9×10^6
5d6s $^1D_2$	6s6p $^3P_1^o$	1032.5	1.1×10^5
5d6s $^1D_2$	6s6p $^3P_2^o$	1255.1	3.0×10^4
5d6s $^1D_2$	6s6p $^1P_1^o$	3832.2	9.3×10^4
6s7s $^3S_1$	6s6p $^3P_0^o$	649.1	9.7×10^6
6s7s $^3S_1$	6s6p $^3P_1^o$	680.1	2.7×10^7
6s7s $^3S_1$	6s6p $^3P_2^o$	770.2	3.8×10^7
6s7s $^3S_1$	6s6p $^1P_1^o$	1311.2	1.6×10^5
6s7s $^1S_0$	6s6p $^3P_1^o$	611.3	4.3×10^5
6s7s $^1S_0$	6s6p $^1P_1^o$	1077.3	3.0×10^7

3.3 Relevant transitions

The most relevant transitions for the operation of the optical clock are the $^1S_0{-}^1P_1$ and $^1S_0{-}^1P_1$ for cooling and trapping whilst the clock transition is the $^1S_0{-}^3P_0$.

3.3.1 399 nm $^1S_0{-}^1P_1$ transition

The strong $^1S_0{-}^1P_1$ transition of ytterbium has a wavelength of 398.9 nm and it is well suited for cooling and trapping. The lifetime of the $^1P_1$ state has been measured $\tau = 5.464(5)$ ns [79]. This translates, neglecting the much weaker decay to other states, to an Einstein A coefficient for the $^1S_0{-}^1P_1$ transition of $A = 1/\tau = 1.830(2) \times 10^8\,\mathrm{s}^{-1}$ and to a natural linewidth $\gamma/(2\pi) = 1/(2\pi\tau) = 29.12(3)$ MHz.

Efficient cooling requires a closed transition, where atoms are not lost from other decay channels. Optical pumping is used for cooling transition that are not closed. The 399 nm transition in ytterbium is not exactly closed because atoms from the $^1P_1$ level can decay in the $^3D_1$, $^3D_2$, and $(7/2, 3/2)_2$ states and those from the ^3D term can decay to to the ^3P term. Atoms in $^3P_1$ decay to the ground state ($\tau = 873$ ns) but $^3P_2$ and $^3P_0$ levels are metastable and atoms in there are lost. Theoretical calculation [77] predicts a rate of decay in the $^3P_2$ and $^3P_0$ levels of $a_{2,0} = 6.6\,\mathrm{s}^{-1}$, or a branching ratio of 4×10^{-8}. Experimentally the branching ratio to the $^3P_1$ level has been measured $1.2(4) \times 10^{-7}$ [80]. This values are low and repumpers laser are not needed for efficient cooling and trapping in a MOT. However adding repumping laser from the $^3P_2$ and $^3P_0$ levels to the higher lying $^3S_1$ level can improve the lifetime in the 399 nm MOT [81].

3.3.2 556 nm $^1S_0{-}^3P_1$ transition

The $^1S_0{-}^3P_1$ transition has a wavelength of 555.6 nm. The lifetime of the $^3P_1$ state has been measured $\tau = 873(2)$ ns [82]. Since atoms from this level decay only in the ground state, the Einstein A coefficient for the $^1S_0{-}^3P_1$ transition is readily calculated $A = 1/\tau = 1.145(3) \times 10^6\,\mathrm{s}^{-1}$. This corresponds to a linewidth $\gamma/(2\pi) = 1/(2\pi\tau) = 182.2(4)$ kHz.

This transition can be used to cool the atoms at lower temperatures (see table 3.4). This transition is closed and can be used to trap a large number of ytterbium atoms directly. Direct loading of the green MOT can be useful for experiments with quantum-degenerate gases but it is too slow for a clock, where a short cycle time is needed.

The mixing of the $^3P_1$ state with the $^1P_1$ state can be written

$$|^1P_1\rangle = \alpha\,|^1P_1^0\rangle + \beta\,|^3P_1^0\rangle\,, \tag{3.1}$$

$$|^3P_1\rangle = \alpha\,|^3P_1^0\rangle - \beta\,|^1P_1^0\rangle\,, \tag{3.2}$$

$$\tag{3.3}$$

where $|^1P_1^0\rangle$ and $|^3P_1^0\rangle$ are the pure LS state in absence of interaction and α and β are complex numbers with $|\alpha|^2 + |\beta|^2 = 1$. Only the component $|^1P_1^0\rangle$ is coupled to the ground state by electric dipole transition and the state $|^3P_1\rangle$ acquires a radiative

Table 3.3: Isotopic and hyperfine shifts from ^{174}Yb of the $^1\mathrm{S}_0-^1\mathrm{P}_1$ transition at 399 nm [83].

Isotope	Rel. strength	Shift /MHz
176	0.1273	−509.31(5)
173 (5/2-5/2)	0.0498	−253.42(5)
174	0.3184	0
173 (5/2-3/2)	0.0225	516.0(2)
172	0.2182	533.31(5)
173 (5/2-7/2)	0.0884	587.99(6)
171 (1/2-3/2)	0.1140	832.44(6)
171 (1/2-1/2)	0.0285	1153.70(6)
170	0.0303	1192.39(7)
168	0.001 35	1887.40(5)

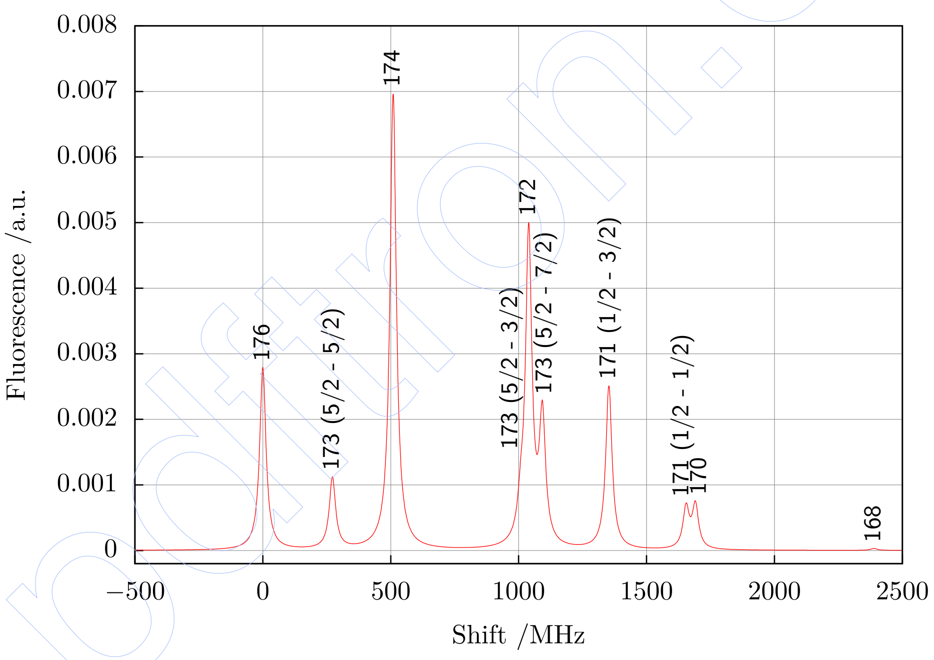

Figure 3.3: Spectrum of the $^1\mathrm{S}_0-^1\mathrm{P}_1$ transition at 399 nm (calculated from table 3.3).

lifetime only from β. The radiative lifetime is given by $\tau \propto \omega^{-3}\rho^{-2}$ where ω is the transition frequency and ρ the dipole matrix element [11]. This allows to calculate from the experimental values of τ and ω

$$\frac{|\alpha|^2}{|\beta|^2} = \frac{\tau(^3\mathrm{P}_1)}{\tau(^1\mathrm{P}_1)} \frac{\omega^3(^3\mathrm{P}_1)}{\omega^3(^1\mathrm{P}_1)} \tag{3.4}$$

so that we can estimate $|\alpha|^2 = 0.983$ and $|\beta|^2 = 1.66\,\%$.

3.3.3 578 nm $^1\mathrm{S}_0$–$^3\mathrm{P}_0$ transition

Whilst the $^1\mathrm{S}_0$–$^3\mathrm{P}_1$ transition is suitable as a clock transition in calcium [36] and magnesium [42], in ytterbium it is too broad for that role. The best candidate for the clock transition in ytterbium is the $^1\mathrm{S}_0$–$^3\mathrm{P}_0$ transition at 578.42 nm. This transition is forbidden by spin-flip and by the electric-dipole selection rule ($\Delta j = 0, \pm 1$, $j = 0 \to j = 0$ forbidden) and the $^3\mathrm{P}_0$ state is metastable. In odd isotopes the hyperfine interaction with the nuclear magnetic moment mixes some of the $^3\mathrm{P}_1$ and $^1\mathrm{P}_1$ state to the metastable state. For ytterbium the lifetime of the $^3\mathrm{P}_0$ state has been theoretical estimated to be $\tau = 20\,\mathrm{s}$ for ^{171}Yb and $\tau = 23\,\mathrm{s}$ for ^{173}Yb [84]. In even isotopes the clock transition is completely forbidden. To observe this transition is necessary to apply an external magnetic field of $\sim 1\,\mathrm{mT}$ (magnetically induced spectroscopy)[85–87]. The external magnetic field couples the $^3\mathrm{P}_1$ state in the metastable $^3\mathrm{P}_0$ state as the nuclear magnetic moment in odd isotopes.

The absolute frequency of the transition has been measured for ^{171}Yb and ^{173}Yb atoms trapped in a MOT with a relative standard uncertainty of $u_\mathrm{r} = 9 \times 10^{-12}$ [52], for ^{174}Yb atoms trapped in an optical lattice with $u_\mathrm{r} = 1.5 \times 10^{-15}$ [44] and for ^{171}Yb atoms trapped in an optical lattice with $u_\mathrm{r} = 1.4 \times 10^{-15}$ [45]. This last uncertainty is the statistical uncertainty of the measurement respect to the caesium primary frequency standard and it is larger that the systematics uncertainty of both clocks. The uncertainty evaluation for the ^{171}Yb clock is 3.4×10^{-16} [45]. A summary of these measurement is given in table 3.5. Table 3.6 gives the isotopic shifts.

3.3.4 Magic wavelength

The magic wavelength for the $^1\mathrm{S}_0$–$^3\mathrm{P}_0$ was theoretically estimated to be 742 nm [84]. It was later determine experimentally to be few nanometres away at 759 nm. The corresponding frequency is 394 798 329(10) MHz for ^{171}Yb [45] and 394 799 475(35) MHz for ^{174}Yb [86]. The slope of the polarizability at the magic wavelength is $(-22(2)\,\mathrm{mHz/GHz})/E_\mathrm{r}$ for a lattice depth expressed in recoil energy E_r.

Table 3.4: Comparison of the properties for the $^1\mathrm{S}_0{-}^1\mathrm{P}_1$, $^1\mathrm{S}_0{-}^3\mathrm{P}_1$, and $^1\mathrm{S}_0{-}^3\mathrm{P}_0$ transitions.

Parameter		$^1\mathrm{S}_0{-}^1\mathrm{P}_1$	$^1\mathrm{S}_0{-}^3\mathrm{P}_1$	$^1\mathrm{S}_0{-}^3\mathrm{P}_0$
Transition wavelength	λ	398.91 nm	555.80 nm	578.42 nm
Transition frequency	$\nu = c/\lambda$	751.53 THz	539.39 THz	518.29 THz
Transition wavenumber	$k = 2\pi/\lambda$	$157\,508\,\mathrm{cm}^{-1}$	$113\,048\,\mathrm{cm}^{-1}$	$17\,288\,\mathrm{cm}^{-1}$
Landè g factor	g_J	1.035	1.492 82	
Lifetime	τ	5.464 ns	873 ns	>20 s
Linewidth	$\gamma/2\pi = 1/(2\pi\tau)$	29.13 MHz	182 kHz	<10 mHz
Saturation intensity	$I_\mathrm{s} = \pi hc/3\lambda^3\tau$	$60\,\mathrm{mW/cm^2}$	$0.14\,\mathrm{mW/cm^2}$	$<10\,\mathrm{pW/cm^2}$
Doppler temperature	$T_\mathrm{D} = \hbar\gamma/(2k_\mathrm{B})$	699 µK	4.4 µK	–
Recoil temperature	$T_\mathrm{r} = \hbar^2k^2/(Mk_\mathrm{B})$	0.70 µK	0.36 µK	0.32 µK

Table 3.5: Absolute frequency determination of the $^1S_0 - ^3P_0$ transition at 578 nm [44, 45, 52].

Yb	ν /THz
171	518.295 836 590 865 2(7)
173	518.294 576 847 6(44)
174	518.294 025 309 217 8(9)

Table 3.6: Isotopic shifts of the $^1S_0 - ^3P_0$ transition at 578 nm (from table 3.5).

Yb	Shift / MHz
171 - 173	1259.743(4)
171 - 174	1811.281 647 4(11)
173 - 174	551.538(4)

Table 3.7: Isotopic and hyperfine shifts from ^{176}Yb of the $^{1}\mathrm{S}_0-^{3}\mathrm{P}_1$ transition at 556 nm [88].

Isotope	Rel. strength	Shift /MHz
173 (5/2-7/2)	0.0715	−1431.87(6)
171 (1/2-1/2)	0.0476	−1177.23(6)
176	0.1274	0
174	0.3187	954.83(6)
172	0.2184	1954.85(6)
170	0.0303	3241.18(6)
173 (5/2-5/2)	0.0537	3266.24(6)
168	0.0014	4609.96(8)
171 (1/2-3/2)	0.0952	4759.44(8)
173 (5/2-3/2)	0.0358	4762.11(12)

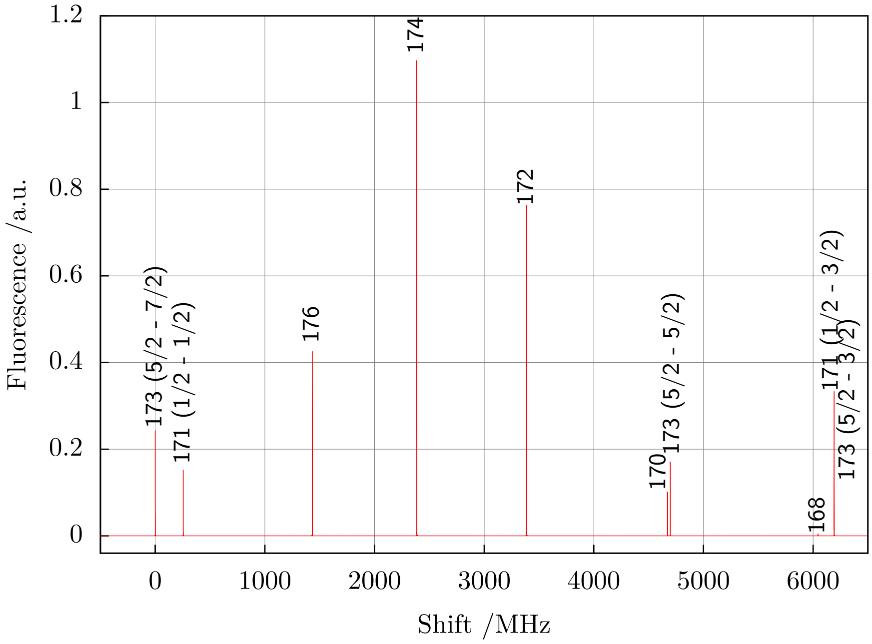

Figure 3.4: Spectrum of the $^{1}\mathrm{S}_0-^{3}\mathrm{P}_1$ transition at 556 nm (calculated from table 3.7).

4 Lasers

Lasers of several wavelengths are necessary for the operation of an optical frequency standard. For ytterbium 399 nm and 556 nm lasers are needed for cooling and trapping, a laser at 578 nm is needed to probe the clock transitions, and the optical lattice should work at the magic wavelength 759 nm. The 399 nm, 556 nm, and 578 nm wavelengths can be obtained efficiently using non-linear optics such as second harmonic generation (SHG) and sum frequency generation (SFG) in non-linear crystals. The magic wavelength is within reach of tunable titanium-sapphire (Ti:sapphire) lasers or amplified diode lasers.

Non-linear optics exploit the, usually weak, second order polarizability of specific crystals (for an introduction see [22, 89, 90]). In a non linear process two photons of frequency ω_1 and ω_2 can be combined in a photon with frequency ω_3. Conservation of energy and momentum requires

$$\omega_1 + \omega_2 = \omega_3 \tag{4.1}$$

$$k_1 + k_2 = k_3, \tag{4.2}$$

where the k are the corresponding wavevectors. For SHG the frequency of the starting photons is the same and we obtain

$$2\omega_1 = \omega_3 \tag{4.3}$$

$$2k_1 = k_3, \tag{4.4}$$

where $k_1 = \omega_1 n_1/c$, $k_3 = \omega_1 n_3/c$ and n_1 and n_3 are the index of refraction for the fundamental and duplicated frequencies. Conservation of energy and momentum thus require $n_1 = n_3$, that is in general not true for ordinary materials that show dispersion. The mismatch in wavevector is described by

$$\mathit{\Delta} k = 2k_1 - k_3 = \frac{2\omega_1}{c}(n_1 - n_3). \tag{4.5}$$

For $\mathit{\Delta} k \neq 0$ the phase velocity of the fundamental and second harmonic wave is not the same. This means that if in a point of the crystal energy flows from ω_1 to ω_3, after a length $1/\mathit{\Delta} k$ the process is reversed and the SHG process in the crystal is not efficient. The condition $\mathit{\Delta} k = 0$ ensures that contributions to the second harmonic wave generated at each point of the crystal add up constructively, maximizing the total SHG power.

Different strategies exist to achieve phasematching. The ones used in this thesis are birefringent phasematching and quasi-phasematching.

In the first case a birefringent crystal is used and the fundamental and doubled fields have perpendicular polarizations. Several configuration are possible; for example the fundamental one could be an ordinary ray propagating with index of refraction n_o (type

I SHG). The second harmonic one is then an extraordinary ray that sees an index of refraction that depends on the angle between the wavevector and the crystal axis θ [90],

$$n_\theta = \left[\frac{\sin^2\theta}{n_\mathrm{o}} + \frac{\cos^2\theta}{n_\mathrm{e}}\right]^{-1/2}, \tag{4.6}$$

where n_o and n_e are the indexes of refraction along the ordinary and extraordinary axes and in general depends on frequency. The phasematching condition $n_1 = n_3$ can thus be achieve choosing a specific angle θ at which

$$n_\mathrm{o}(\omega_1) = n_\theta(\omega_3), \tag{4.7}$$

so that the SHG can be tuned rotating the crystal.

Angle tuning has a disadvantage. Because of birefringence the energy of the second harmonic wave travels at an angle $\rho = -(1/n_\theta)\partial n_\theta/\partial\theta$ respect to the fundamental one (the Poynting vector is not aligned with k). This angle, called walk-off angle, limits the useful length of the crystal that can be exploited for SHG, because after a certain length the fundamental wave and the second harmonic are not longer superimposed.

A formula for the SHG power considering walk-off and gaussian beams was given in [91]. The same formula in SI units can be found in [90]

$$P_3 = \frac{16\pi^2 d_\mathrm{eff}^2 l}{\epsilon_0 c \lambda_1^3 n_3 n_1} P_1^2 \mathrm{e}^{-\alpha' l} h_\mathrm{m}(B, \xi), \tag{4.8}$$

where P_1 is the fundamental power on the crystal, P_3 is the second-harmonic power, d_eff is the effective non-linear coefficient for the crystal, l is the length of the crystal, and α' accounts for absorption at both wavelengths $\alpha' = \alpha_1 + \alpha_3/2$. The function $h_\mathrm{m}(B, \xi)$ (Boyd-Kleinman factor) accounts for walk-off $B = \rho\sqrt{lk_1}/2$ and the focusing of the gaussian beam $\xi = 2l/z_\mathrm{R}$, where $z_\mathrm{R} = \pi w_0^2/\lambda_1$ is the Rayleigh range of the gaussian mode of the fundamental and w_0 is the beam waist radius. Depending on B, h_m has a maximum for ξ between 1.39 and 2.64. For $B = 0$ (no walk-off) the maximum of $h_\mathrm{m} \simeq 1$. Instead h_m strongly reduce the SHG power for large B.

Another strategy that avoids the problems arising from walk-off is quasi-phasematching. In quasi-phasematching the nonlinear properties of the crystal are artificially structured (poled) to maintain the fundamental and the second harmonic in phase. For example a crystal can be periodically poled with a period $\mathit{\Lambda}$. By poling the phase of the second harmonic wave is reversed in each period. When the crystal is grown so that $\mathit{\Lambda} = 1/\mathit{\Delta} k$ the contribution from each period adds constructively even if there is dispersion. The length of the poling can be optimized changing the temperature of the crystal.

4.1 Blue laser generation with PPKTP

The 399 nm radiation has a peculiar color, at the edge of the visible spectrum and hard to focus by the human eye. It is a deep violet but the spots of 399 nm laser on white paper is electric blue. In ytterbium experiments lasers at this wavelength are refereed as blue lasers.

Light at 399 nm can be obtained by indium gallium nitride diode lasers [87]. They can have moderate power (30 mW) and more diode lasers could be injection locked to obtained the power needed for trapping ytterbium [87]. Their availability is really limited at 399 nm, because companies concentrates on the 405 nm wavelength used in Blu-ray Disc readers.

Non-linear optics is thus an interesting solution, with the double wavelength 798 nm available using Ti:sapphire lasers or amplified diode lasers. In INRIM experiment the blue 399 nm radiation is obtained by SHG from a 798 nm Ti:sapphire laser using a periodically-poled potassium titanyl phosphate (PPKTP) crystal ($KTiOPO_4$), looking for high power, stability and tunability.

The 798 nm source is a Coherent MBR-110 Ti:sapphire laser pumped by a 8 W solid state pump laser at 532 nm (Coherent Verdi-V8). The MBR laser can be tuned from 700 nm to 970 nm and it has an output power at 798 nm of 1.3 W.

The MBR is a complex laser and several components are built in it for single frequency lasing and for continuous scanning range. It has a ring cavity with an optical diode (Faraday isolator) for single direction operations. A birefringent filter is used for coarse wavelength selection. A thin etalon is placed inside its cavity to select only a longitudinal mode. The etalon is actively locked to the cavity resonance using a first harmonic technique; the etalon angle is modulated at 80 kHz for this purpose. A piezo is mounted on one of the cavity mirror for fine tuning of the frequency. This piezo is used to lock the laser frequency to an external reference cavity made in Invar using a side-of-the-fringe technique. The reference cavity has its own piezo that can be externally tuned. When locked to the reference cavity the MBR has a linewidth < 20 kHz.

The setup for SHG is shown in fig. 4.4. A bow-tie enhancement cavity resonant at 798 nm is formed using 4 mirrors M1-4. The cavity is necessary to increase the running power on the crystal and thus to improve the SHG. I will give more detail on the design of a duplication cavity in the next section. The PPKTP crystal is 10 mm long and placed between M3 and M4, on a rotation stage. The working temperature of the oven is around 50 °C.

The light from the MBR laser is coupled to the cavity using two mode-matching lenses. An optical isolator prevents reflections on the laser. The length of the cavity is locked to the Ti:sapphire frequency using the Hänsch-Couillaud technique [92], since the PPKTP crystal is birefringent. The reflection from mirror M1 is passed through a neutral filter, a quarter-wave plate ($\lambda/4$ waveplate) and an beam-splitter cube. The difference of the signals of two photodiodes on the cube outputs is the Hänsch-Couillaud error signal. The servo acts on a piezo transducer on mirror M2.

The typical SHG power output of the PPKTP crystal ranges from 60 mW to 90 mW; this power is enough for trapping ytterbium atoms and for clock operations. However this crystal proved to be unreliable at 399 nm. The wavelength 399 nm is on the border of the transparency range for PPKTP (stated 350 nm to 4400 nm) and the absorption of the crystal in the blue is limiting the performances of SHG. Absorption causes the properties of the crystal to depends on the SHG power. Locking the resonant cavity

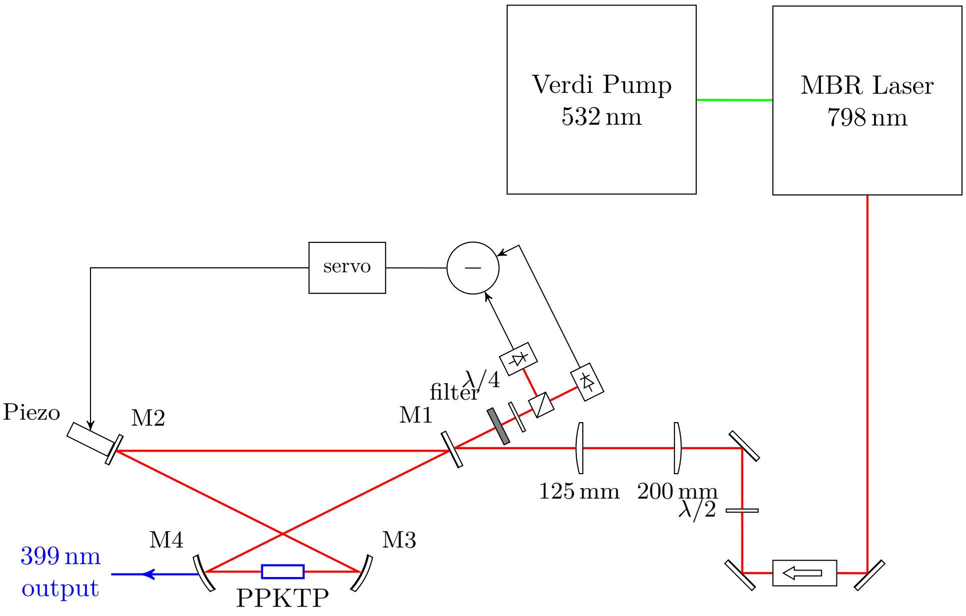

Figure 4.1: Scheme for the SHG of the 399 nm laser using the PPKTP crystal.

causes a sudden increase in blue power that changes the temperature of the crystal and deforms the Hänsch-Couillaud signal. These effects require tweaking to re-optimize the SHG and make the locking unstable and unreliable. The higher the power the greater are the effects of absorption and the more unstable is the locking of the cavity. For example, the system is capable of generating 150 mW at 399 nm but most of the time we operate the system to have only 60 mW of blue, limiting the power at 798 nm if necessary. The experiment described in chapter 6 are performed with this setup and with up to 60 mW at 399 nm generated by only 800 mW at 798 nm.

4.2 Blue generation with LBO

Looking for a reliable way to obtaine the blue laser we recently tried a different crystal after the suggestion from the Quantum Gas group at LENS in Firenze [93]. The new crystal is lithium triborate (LBO), LiB_3O_5, a robust material used, for example, in the Verdi pump lasers, and already exploited for ytterbium experiments [93, 94]. LBO has some advantages over PPKTP: it is transparent from 160 nm to 2600 nm and thus does not have thermal effects from absorption at 399 nm; it is a bulk crystal that does not require precise temperature control. In this section I will describe the optimizations and calculations necessary for a successful SHG design.

Our LBO crystal is made by Raicol, is $l = 15$ mm long, has a section of 1.5 mm × 1.5 mm, and is cut for normal incidence with antireflection coating on the faces. Phasematching is achieved by angle-tuning (critical phase matching). Some properties of LBO are reported in table 4.1

Table 4.1: Properties of LBO crystal for SHG from 798 nm to 399 nm [95].

Parameter			
Nonlinear coefficient	/(m/V)	d_{eff}	0.75×10^{-12}
Walk-off angle	/rad	ρ	0.0162
Ordinary index of refraction at 798 nm		$n_{\mathrm{o}}(\omega_1)$	1.611
Extraordinary index of refraction at 399 nm		$n_{\mathrm{e}}(\omega_3)$	1.611
Absortion at 798 nm	/m^{-1}	α_1	3.5×10^{-2}
Absortion at 399 nm	/m^{-1}	α_3	3.1×10^{-1}

For our crystal $B = 3.53$ and the Boyd-Kleinman factor of eq. (4.8) [91] has a maximum of $h_{\mathrm{m}} = 0.2$ for $\xi = 1.5$. For the crystal length $l = 15\,\mathrm{mm}$ this corresponds to a Rayleigh range $z_{\mathrm{R}} = 4.8\,\mathrm{mm}$, or a confocal parameter $b = 2z_{\mathrm{R}} = 9.6\,\mathrm{mm}$ or a waist radius $w_0 = \sqrt{z_{\mathrm{R}}\lambda/\pi} = 35\,\mu\mathrm{m}$. With this parameters we can calculate the SHG power as

$$P_3 = E_{\mathrm{nl}} P_{1\mathrm{c}}^2 \tag{4.9}$$

where $E_{\mathrm{nl}} = 7.5 \times 10^{-5}\,\mathrm{W}^{-1}$ as calculated from eq. (4.8) and $P_{1\mathrm{c}}$ is the power at 798 nm circulating in the duplication cavity.

4.2.1 Choice of the input coupler

The power circulating in the enhancing cavity $P_{1\mathrm{c}}$ is related to the power injected in the cavity P_1 by [96]

$$P_{1\mathrm{c}} = \frac{P_1 T_1}{\left[1 - \sqrt{(1-T_1)(1-l_{\mathrm{cav}})(1-E_{\mathrm{nl}}P_{1\mathrm{c}})}\right]^2}, \tag{4.10}$$

where T_1 is the transmission of the input coupler of the cavity (M1 in figs. 4.1 and 4.3) and l_{cav} represents the linear losses in the cavity, by the crystal and mirrors other than the input coupler.

If the quadratic depletion of the pump is negligible ($(1 - E_{\mathrm{nl}}P_{1\mathrm{c}}) \approx 1$), the power circulating in the cavity is maximized choosing an input coupler transmission $T_1 = l_{\mathrm{cav}}$. This situation is a sort of impedance matching in which the power injected in the cavity corresponds exactly to the round trip power loss.

If the depletion of the pump is not negligible, that is for high efficient SHG, eq. (4.10) should in general be solved numerically for $P_{1\mathrm{c}}$. The optimal input coupler transmission depends on the linear losses and the input power

$$T_1 = \frac{l_{\mathrm{cav}}}{2} + \sqrt{\frac{l_{\mathrm{cav}}^2}{4} + E_{\mathrm{nl}}P_1}. \tag{4.11}$$

For example the dependence of the SHG power with the transmission of the input coupler M1 for different linear losses is shown in fig. 4.2. The input coupler transmission should then be chosen to match the input power and the linear losses of the actual cavity.

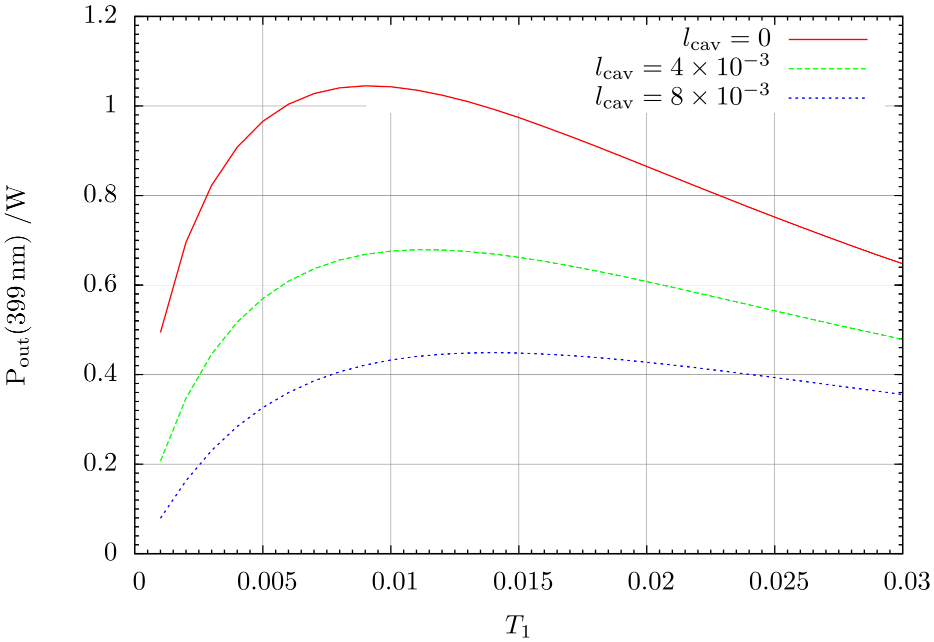

Figure 4.2: Example of the dependence of the SHG power with the transmission of the input coupler M1 for different linear losses in cavity, assuming an input power $P_1 = 1.1\,\mathrm{W}$.

4.2.2 Design of the cavity mode

We should design a resonant cavity with the required waist 35 µm. This can be done using the $ABCD$ matrices formalism [97] to optimize the distances between the mirrors. I have done the calculations following [98].

Consider a bow-tie enhancing cavity like in fig. 4.3 with two flat mirrors (M1 and M2) and two curved mirrors with radius R and focal length $f = R/2$ (M3 and M4). Midway between M3 and M4 there is the nonlinear crystal of length l and index of refraction n at the fundamental wavelength. Let u be the distance between one of the curved mirror and the waist in the center of the crystal, v the distance between the same mirror and the secondary waist, and α the angle of incidence on the mirrors.

Let $z_{\mathrm{R}x}$ and $z_{\mathrm{R}y}$ be the Rayleigh ranges for the principal waist in the tangential and sagittal directions. Following [98] we can define the following adimensional variables

$$U = \frac{u}{f}, \quad V = \frac{v}{f}, \tag{4.12}$$

$$X = \frac{z_{\mathrm{R}x}}{nf}, \quad Y = \frac{z_{\mathrm{R}y}}{nf}, \tag{4.13}$$

$$\phi = \cos\alpha, \tag{4.14}$$

and the function

$$\mathcal{F}(U,V) = \frac{U-1}{V-1}\left(1-(U-1)(V-1)\right). \tag{4.15}$$

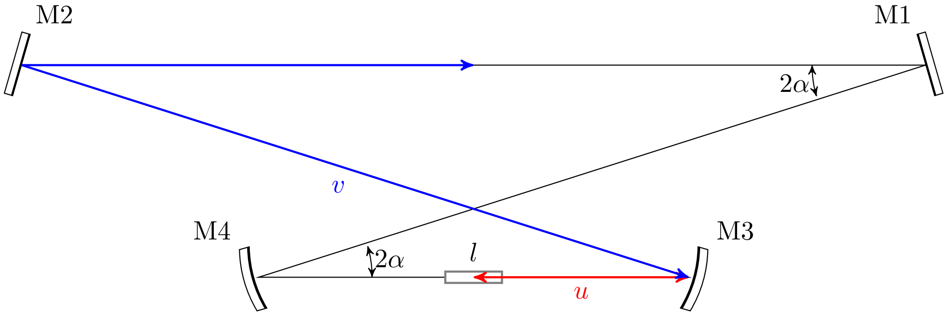

Figure 4.3: Geometrical parameters for the SHG cavity.

Then we want to simultaneously solve for

$$\mathcal{F}\left(\frac{U}{\phi}, \frac{V}{\phi}\right) = \frac{X^2}{\phi^2}, \tag{4.16}$$

$$\mathcal{F}\left(U\phi, V\phi\right) = Y^2\phi^2. \tag{4.17}$$

Without astigmatism from the folding ($\phi = 1$) the formula is the same in the tangential and sagittal plane. Even with astigmatism the previous equations can be solved for a circular waist ($X = Y$).

In our cavity is $z_{\mathrm{R}x} = z_{\mathrm{R}y} = \pi w_0^2/\lambda = 4.8\,\mathrm{mm}$ and we fixed the folding angle $2\alpha = 16°$. The radius of curvature of the mirrors M3 and M4 is $R = 100\,\mathrm{mm}$. Then numerically solving eq. (4.16) and eq. (4.17) results in $u = 54.1\,\mathrm{mm}$ and $v = 303.2\,\mathrm{mm}$. The physical distance between the center of the crystal and one of the curved mirror should take into account the index of refraction of the crystal and is [98]

$$g = u + l\frac{n-1}{2n} = 56.9\,\mathrm{mm}. \tag{4.18}$$

Setting the principal waist circular makes the secondary waist slightly elliptical. In our cavity $w_{2x} = 261\,\mathrm{\mu m}$ and $w_{2y} = 295\,\mathrm{\mu m}$. This is not of concern because the MBR laser we want to couple in the cavity has a slightly elliptical mode on its own, and the mode-matching between the MBR laser and the cavity can be easily calculated.

4.2.3 Results

Figure 4.4 shows a technical draw with the dimensions of the cavity. Figure 4.5 shows a picture. For maximum stability and simplicity in the alignment we mounted the mirrors on a monolithic block of aluminum with holes for the mirror mounts machined according to the previous calculations. Mirror mounts are top-actuated for easy alignment. The flat mirror M2 is mounted on a small piezo actuator for locking of the cavity on the MBR laser. The LBO crystal is mounted on a copper oven on top of a rotational stage.

The reflectivity of the mirrors M2, M3, and M4 is nominally $R > 0.999$ at 798 nm. The loss in the crystal for the fundamental is expected 5.2×10^{-4} while the anti-reflection

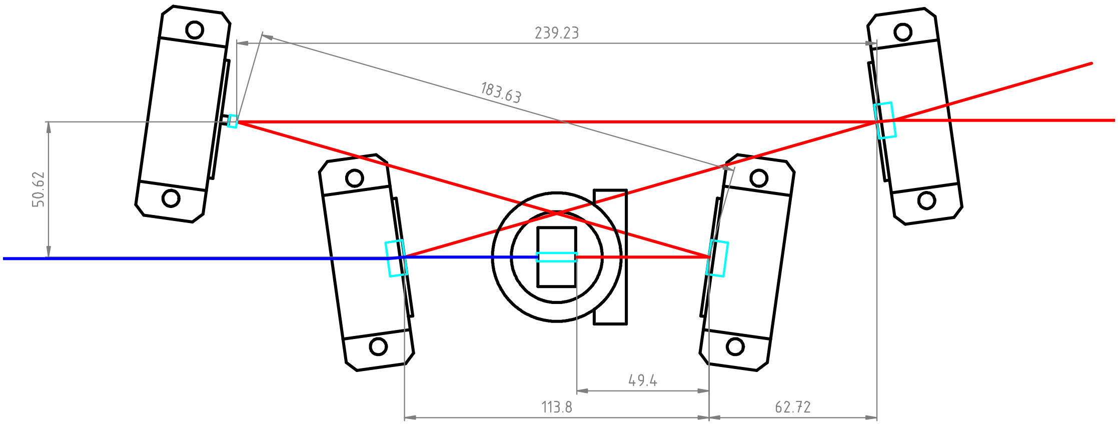

Figure 4.4: Technical draw of the cavity for the SHG of 399 nm with the LBO crystal. Quotes report the dimensions of the cavity in millimetres.

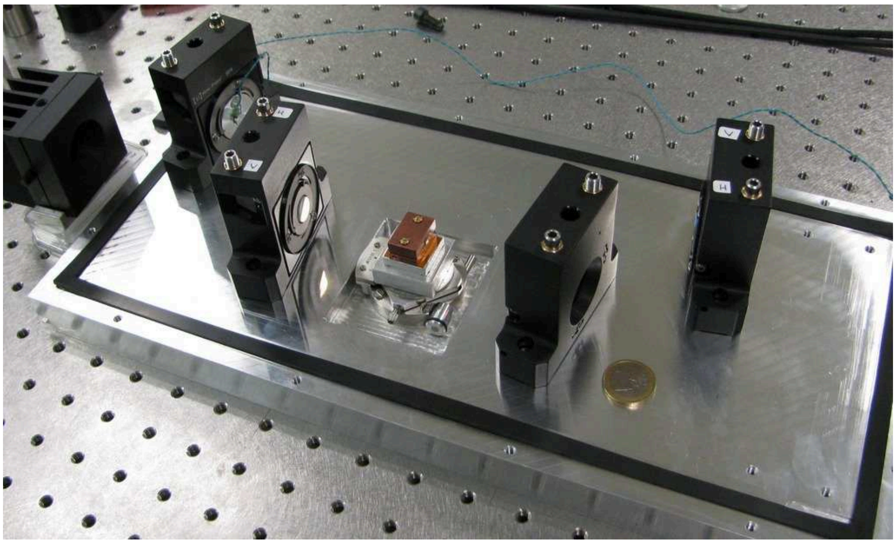

Figure 4.5: Picture of the cavity for the SHG of 399 nm. The LBO crystal is in the copper oven in the center.

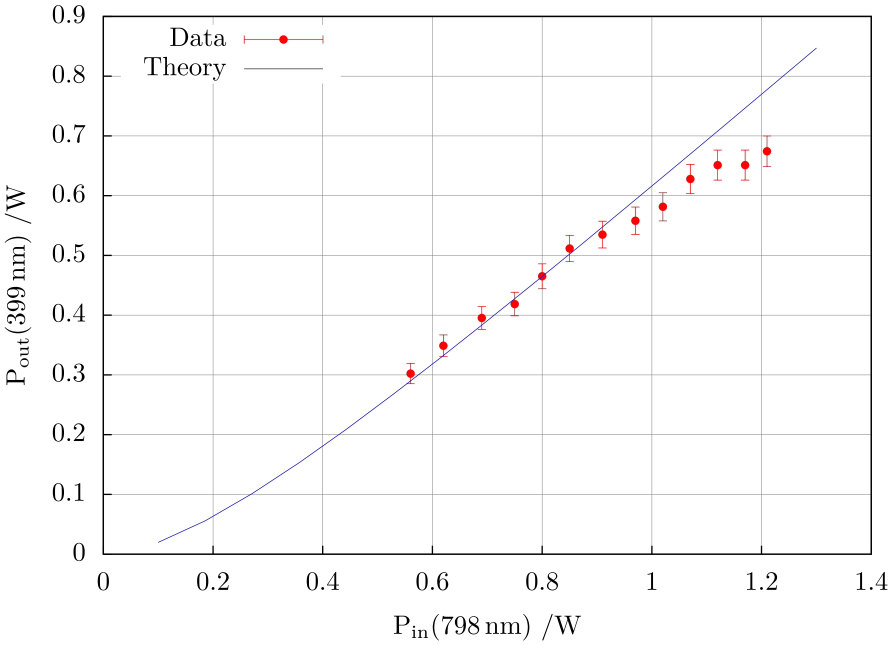

Figure 4.6: SHG power as a function of input power. The continuous line is theoretically calculated for $T_1 = 0.012$ and $l_{cav} = 3.8 \times 10^{-3}$.

coating of the crystal faces has a nominal loss of 1×10^{-3}. We can then estimate the linear losses in the cavity $l_{cav} < 5 \times 10^{-3}$.

We chose the input coupler reflection at 0.988 ($T_1 = 0.012$). Mirror M4 is anti-reflection coated for the 399 nm with a transmission of 0.95.

The MBR laser is coupled to the secondary waist of the cavity using two lenses for mode-matching. After the optical isolator and the other optics the maximum power at 798 nm on the cavity is 1.2 W.

Mirror M2 is mounted on a small piezo for frequency tuning. The cavity is locked to the MBR frequency using again the Hänsch-Couillaud technique, as in the setup for the PPKTP crystal (section 4.1).

Figure 4.6 shows experimental data for the SHG power at 399 nm as a function of the input power. The output has a maximum power of 0.65 W with 1.2 W of input power; the SHG efficiency is 54 %. The same figure shows also a theoretical prediction of the SHG power for $T_1 = 0.012$ and $l_{cav} = 3.8 \times 10^{-3}$. Theory and experimental data are well matched; they slightly diverge at high power because each data point was taken without re-alignment of the optics.

4.3 Green generation

The green 556 nm radiation is obtained by SHG from a 1112 nm fiber laser using another PPKTP crystal.

The 1112 nm laser source is a ytterbium doped fiber laser Koheras Adjustik. It has a maximum output power of 10 mW at this wavelength and a linewidth of 70 kHz. It has two frequency controls; the temperature of the fiber can be used for coarse wavelength tuning while a piezo can be used for fast control (up to 20 kHz).

The output of the fiber laser is sent to a fiber amplifier Keopsys Benchtop. This amplifier is nominally capable of 4 W of output while seeded by the fiber laser. However we removed the cooling fans of the amplifier that were causing additional frequency noise, and reduced the power. We have measured up to 1.3 W just after the amplifier in the optimal setup. Higher powers make the amplifier unstable and unreliable.

The amplified laser is send on the non-linear crystal using free-air optics (see fig. 4.7). First we use an optical isolator because the fiber amplifier is highly susceptible to feedback. The polarization of the light on the isolator is tuned acting on two polarization controls (paddles) on both the output fibers of the laser and of the amplifier. Then the 1112 laser is steered on the crystal using two mirrors and its polarization is cleaned using one half-wave plate ($\lambda/2$ waveplate) and one $\lambda/4$ waveplate. The laser is focused on the crystal using a 50 mm lens.

The PPKTP crystal is 20 mm long and used in single pass. It is held in a copper oven for temperature stabilization. The phase-matching condition is achieved changing the temperature and it is found around 46 °C.

After the crystal the green light generated is shaped using another lens. Two mirrors for the visible wavelengths are used to filter the infrared light before the green is sent to the acousto-optic modulators (AOMs) and the fiber couplings needed for the experiment.

Up to 12 mW of 556 nm light has been obtained starting from 1.1 W of 1112 nm measured at the crystal. We swapped the crystal for another one, identical to the former, and observed almost identical performances even if the first crystal has been used for 7 years.

We have observed some degradation of the power at 556 nm. We believe the fiber amplifier is loosing efficiency and since the SHG depends quadratically on the fundamental power, this greatly affects the power available after the crystal. In six months the maximum power went from 12 mW to 9 mW.

4.4 Yellow generation

The yellow laser at 578 nm is obtained by SFG in a periodically-poled lithium niobate (PPLN), $LiNbO_3$, crystal, as shown in fig. 4.8, using two infrared laser sources (1030 nm and 1319 nm). Light at 578 nm can be obtained by SHG of a quantum-dot laser at 1156 nm [99] but SFG allows for more power [100].

The 1319 nm source is a monolithic neodymium-doped yttrium aluminium garnet (Nd:YAG) laser (Lightwave Electronics Model 126). It has an output power of 90 mW and a linewidth of less than 5 kHz when measured at 1 ms. Its frequency can be tuned by two controls. The slow one is achieved by heating or cooling the laser crystal, has a scanning range of 10 GHz, and it can respond up to 1 GHz/s. The fast control drive a piezoelectric element that tune the frequency with a range of 30 MHz and a bandwidth

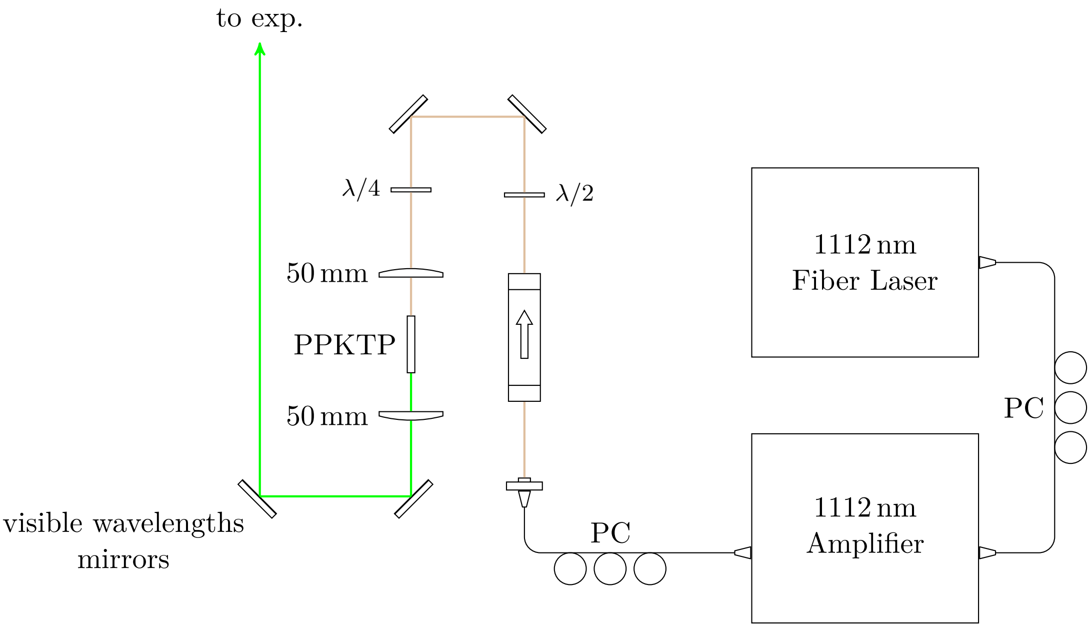

Figure 4.7: Scheme for the SHG of the 556 nm laser. PC, polarization control.

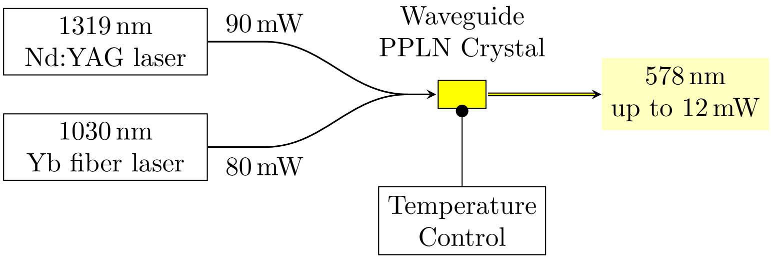

Figure 4.8: Scheme for the SFG of the 578 nm laser.

up to 100 kHz.

The 1030 nm source is an erbium fiber laser (NP Photonics' Rock Laser) with 80 mW output power. The manufacturer declares a linewidth of less than 10 kHz. It can be frequency tuned on a 500 MHz range with a bandwidth up to 30 kHz.

The crystal is a waveguide, magnesium-doped, PPLN device, produced by HC Photonics. Being a waveguide crystal, the infrared lasers are coupled to one of 32 working channels where are tightly confined over the length of the crystal (20 mm). This design avoids problems arising from the focusing of the beam, diffraction, or walk-off angles. The crystal is designed to work without an enhancing cavity, since it is already quite efficient.

Infrared light of both lasers is delivered to the crystal through a polarization-maintaining (PM) fiber coupler (Y-shaped). The coupler is especially made to couple 1319 nm light on one port and 1030 nm on the other. The 1319 nm Nd:YAG laser is mode-matched with two lenses in the fiber while the 1030 nm fiber laser is directly coupled. The output of the coupler is bare fiber, and it is simply put near to the input face of the crystal to couple the light with the non-linear waveguide (the distance is of the order of 1 µm). To this purpose, the crystal is placed on a high-precision manual 3-axes stage. Optical isolators are used on both lasers since the bare fiber end of the coupler was causing enough backreflection to destabilize both source (especially the 1030 nm fiber laser). The SFG works only with one polarization of the input beams (vertical); being the fiber PM, the correct polarization is achieved manually rotating the fiber itself. At the crystal output, a microscope objective collimates the 578 nm laser beam, and then the residual infrared light is filtered using mirrors for the visible wavelength.

The non-linear crystal held in a copper oven. It is thermally tuned, achieving phase-matching and maximizing the output power at 578 nm, with a heater and a thermal control. Figure 4.9 shows the dependency of the power of the yellow laser obtained by SFG versus the temperature of the non-linear device. The power shows a typical diffraction-like behaviour around the phase-matching temperature found at about 76 °C.

Infrared powers at the crystal are 33 mW for the 1319 nm laser (some power is lost with the fiber coupling) and 80 mW for the 1030 nm fiber laser. Only a fraction of the input light is effectively coupled with the waveguide: this fraction was measured following the crystal with a lens and with a power-meter far form the crystal to avoid scattering uncoupled light on the sensor. The powers coupled with the waveguide are $P_{\mathrm{coupl}}(1319\,\mathrm{nm}) = 17\,\mathrm{mW}$ and $P_{\mathrm{coupl}}(1030\,\mathrm{nm}) = 41\,\mathrm{mW}$. These values are better estimates of the powers involved in the sum frequency generation. We have obtained up to $P_{\mathrm{out}} = 12\,\mathrm{mW}$ of laser at 578 nm that is the maximum value the manufacturer of the crystal suggests not to exceed.

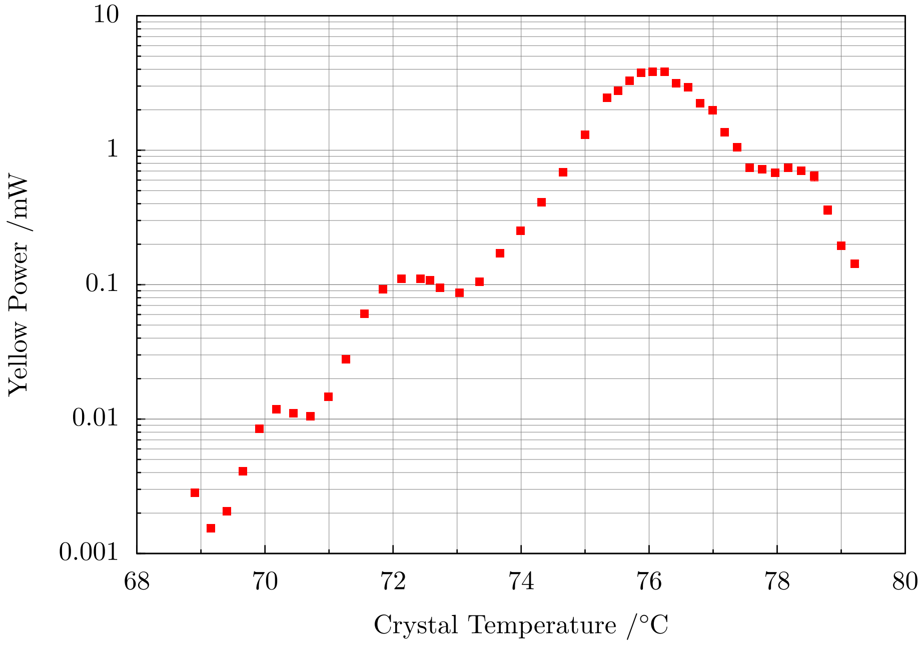

Figure 4.9: Output power of the yellow laser obtained by SFG as a function of the temperature of the non-linear crystal. Phase-matching temperature is achieved at about 76 °C.

5 Stabilization of the clock laser

A low-noise, narrow linewidth laser is fundamental to probe the narrow clock transitions in optical frequency standards. One of the attractive feature of an optical frequency standard is the high stability, but this is limited by the Dick effect [101, 102]. Because optical standards work periodically sampling the atomic transition the frequency stability is degraded by the frequency noise of the clock laser; the laser noise at Fourier frequency close to the multiple of the cycle frequency are down-converted or aliased degrading the clock stability. The limit to the stability is given by [102]

$$\sigma_y(\tau) = \frac{1}{\tau} \sum_{m=1}^{\infty} \frac{g_m^2}{g_0^2} S_y\left(\frac{m}{T_\mathrm{c}}\right), \tag{5.1}$$

where τ is the integration time, T_c the cycle time, g_m and g_0 coefficient that depend on the interrogation scheme and $S_y(m/T_\mathrm{c})$ is the one-sided power spectral density of the relative frequency fluctuations of the free running laser at Fourier frequency m/T_c.

A low noise laser is achieved locking the frequency of the laser to ultrastable Fabry-Pérot cavities. Ultrastable optical cavities are largely used for high-resolution spectroscopy and optical atomics clocks [31, 39], test of fundamental physics [103], generation of low-phase-noise micro-wave signals [104], frequency transfers via fiber link [62, 105], and gravitational wave detection [106].

Laser frequency locking to a cavity is usually done with the powerful Pound-Drever-Hall technique [107]. An introduction to this technique can be found in [108].

When the Pound-Drever-Hall locking is properly executed, the frequency noise spectrum of the laser closely reproduces that of the cavity length. So it is important to reduce the impact of vibrations and temperature variations that will eventually be converted in laser frequency noise. For this last reason the spacer of the cavity is made in materials with low thermal expansion. Corning Ultra Low Expansion glass (ULE) is the most common choice for ultrastable Fabry-Pérot cavities [21, 109–115]. (An alternative lately presented [116] is crystalline silicon working at cryogenic temperatures.) The cavities at INRIM are made of ULE. For a Fabry-Pérot cavity entirely made in ULE a temperature T_0 exists where the linear coefficient of thermal expansion (CTE) is zero, usually around room temperature. The relative length or the fractional frequency depends quadratically with the temperature in the neighborhood of T_0 [117]:

$$\frac{\Delta\nu}{\nu} = \frac{\Delta L}{L} \simeq \alpha (T - T_0)^2. \tag{5.2}$$

Here $\alpha \simeq 1 \times 10^{-9}\,\mathrm{K}^{-2}$ for ULE.

State of the art lasers stabilized on ULE cavity are limited to a fractional frequency instabilities on the order of few parts in 10^{-16} by fundamental thermal noise [118].

I present here the characterization of the stabilization to the clock laser to a cavity made in ULE 10 cm long. Details of our clock laser have been presented in [60, 119].

5.1 Thermal limit and finite element analysis

The thermal noise limit for ULE cavity has been calculated in [118, 120]. Following [120] the limit to thermal noise coming from contribution of the mirror substrates, of the mirror coating and of the cavity spacer are, expressed as Allan variance [7]

$$\sigma_{\mathrm{sb}}^2 = \frac{8 \ln 2 k_{\mathrm{B}} T}{\pi L_{\mathrm{sp}}^2} \frac{(1-\sigma^2)}{2\sqrt{\pi} E w)} \phi_{\mathrm{sb}}, \tag{5.3}$$

$$\sigma_{\mathrm{ct}}^2 = \sigma_{\mathrm{sb}}^2 \frac{2}{\sqrt{\pi}} \frac{1-2\sigma}{1-\sigma} \frac{d_{\mathrm{ct}}}{w} \frac{\phi_{\mathrm{ct}}}{\phi_{\mathrm{sb}}}, \tag{5.4}$$

$$\sigma_{\mathrm{sp}}^2 = \frac{8 \ln 2 k_{\mathrm{B}} T}{\pi L_{\mathrm{sp}}^2} \frac{L}{2\pi E (R_{\mathrm{sp}}^2 - r_{\mathrm{sp}}^2)} \phi_{\mathrm{sp}}. \tag{5.5}$$

Here k_{B} is the Boltzmann constant, T the temperature, σ and E are the Poisson's ratio and Young's modulus of ULE, L_{sp} and R_{sp} are the length and radius of the spacer (cylindrical), r_{sp} is the spacer central bore radius, d_{ct} is the coating thickness, w the spot radius on the mirror and $\phi_{\mathrm{sb}}, \phi_{\mathrm{sp}}, \phi_{\mathrm{ct}}$ are the mechanical losses for the substrate, coating and spacer. Since there are two mirror the final theoretical limit for the frequency stability is

$$\sigma_{\mathrm{lim}}^2 = 2\sigma_{\mathrm{sb}}^2 + 2\sigma_{\mathrm{ct}}^2 + \sigma_{\mathrm{sp}}^2. \tag{5.6}$$

The cavity is entirely (spacer and mirrors) made of ULE. The spacer is a notched cylinder 10 cm in length for 1.5 GHz of free spectral range (see fig. 5.1). The input mirror is flat while the second one has a radius of curvature of $R = 500$ mm. The mode waist on the flat mirror can be calculated [97] as $w_0 = 190\,\mu$m.

The thermal noise contributions for the cavity are

$$\sigma_{\mathrm{sb}} = 5 \times 10^{-16}, \tag{5.7}$$

$$\sigma_{\mathrm{ct}} = 2 \times 10^{-16}, \tag{5.8}$$

$$\sigma_{\mathrm{sp}} = 7 \times 10^{-17} \tag{5.9}$$

$$\tag{5.10}$$

for a thermal limit

$$\sigma_{\mathrm{lim}} = 8 \times 10^{-16}. \tag{5.11}$$

I have used $E = 6.74 \times 10^{10}$ Pa, $\sigma = 0.17$, $\phi_{\mathrm{sb}} = \phi_{\mathrm{sp}} = 1.7 \times 10^{-4}$ for ULE, and $\phi_{\mathrm{ct}} = 4 \times 10^{-4}$. The dimensions of the cavity are $L_{\mathrm{sp}} = 10$ cm, $R_{\mathrm{sp}} = 2.5$ cm, $r_{\mathrm{sp}} = 6.35$ mm and $d_{\mathrm{ct}} = 2\,\mu$m.

A proper design and proper suspension of the optical cavity result in a strong attenuation of the vibration sensitivity [109, 113]. Several strategies are possible. The cavity can be mounted vertically and held in the mid plane suppressing vertical vibrations

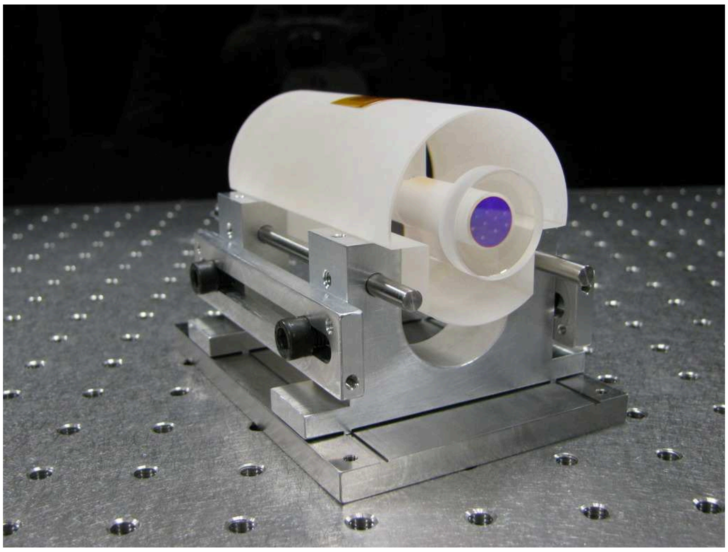

Figure 5.1: Picture of the ULE cavity.

[111, 115, 116]. Alternatively the cavity can be held horizontally [109, 113, 114, 121] and the position of the support can be chosen to minimize the sensitivity of the optical axis length to accelerations. In this case the cavity is said to be supported at the Airy points.

The cavity at INRIM is held horizontally at four points and is supported by 4 Viton pads on an aluminum structure. The spacer is a notched cylinder, similar to the one used in [121].

In general finite elements modeling (FEM) should be performed to investigate the elastic deformation of the Fabry-Pérot cavity under the action of gravity. In the low frequency regime this static condition can then be extrapolated to obtained the vibration sensitivity in the horizontal and vertical directions. For example fig. 5.2 shows FEM calculations for the variation of the cavity length. The variation is calculated as a function of vertical displacement from the mirror centers and for some possible pads positions. Pads position is set by the distance m from the mirror side of the spacer and the distance n from the internal side of the notch. Figure 5.3 shows the deduced vertical sensitivity, as a function of vertical distance from the optical axis and for different pads positions m and n. The lower vibration sensitivity is $4 \times 10^{-11}\,\mathrm{s}^2\,\mathrm{m}^{-1}$ when the pads are located at $m = 19\,\mathrm{mm}$ and $n = 2\,\mathrm{mm}$. As shown, a change in the pads position could result in a large increase of sensitivity even within 1 mm pads displacement along the axial direction.

5.2 Experimental setup

The physics package of the experiment is shown on fig. 5.4. The ULE cavity is held in a stainless steel vacuum chamber where an ion pump keeps the pressure below 1×10^{-4} Pa.

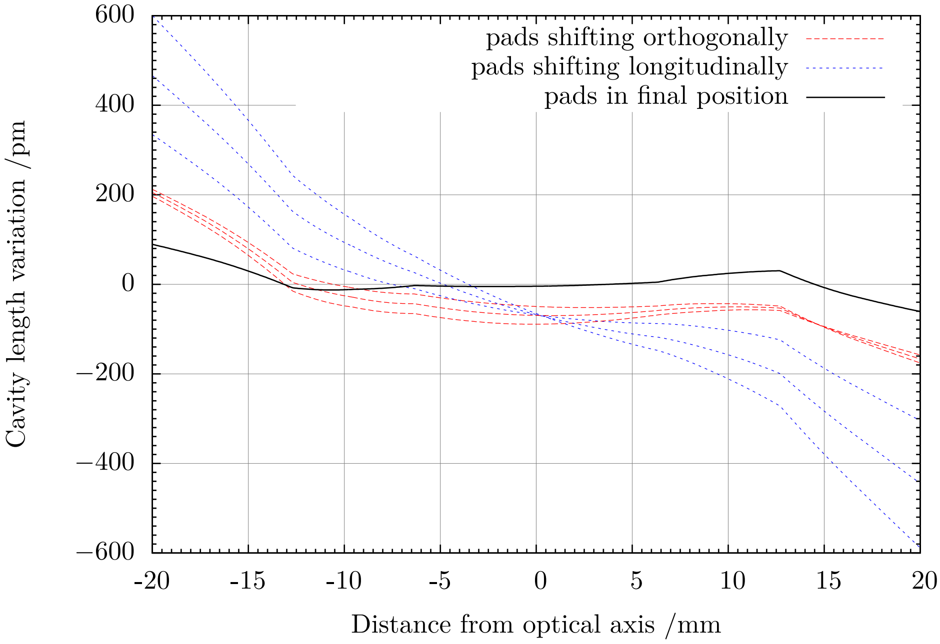

Figure 5.2: FEM calculations for the variation of the cavity length as a function of vertical displacement from the mirror centers and for some possible pads positions. Final position is $m = 19\,\mathrm{mm}$ and $n = 2\,\mathrm{mm}$.

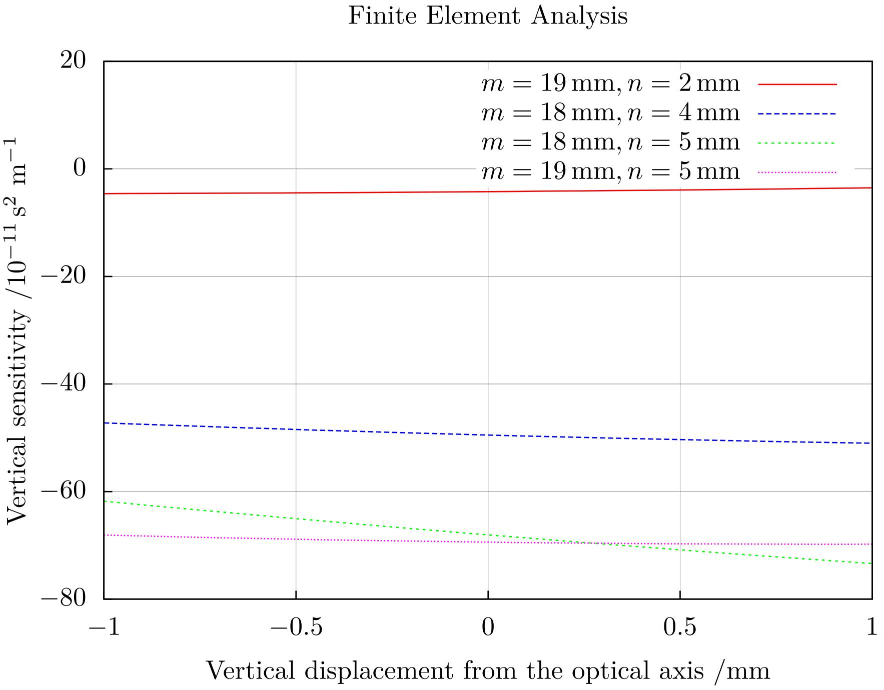

Figure 5.3: FEM calculations for the sensitivity to vertical accelerations for some possible pads positions.

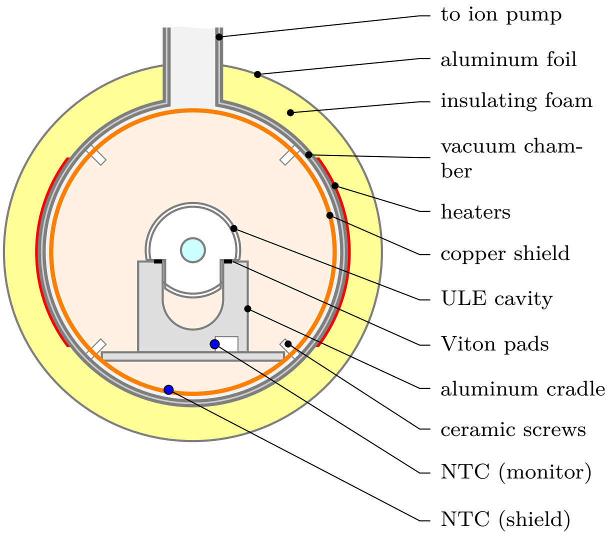

Figure 5.4: Schematic diagram of the vacuum chamber for the ULE cavity, highlighting the thermal isolation of the ULE cavity.

It is supported by 4 Viton pads on an aluminum structure. A copper radiation shield surrounds the cavity and it is held in place by 4 ceramic and 4 nylon screws. Putting the cavity inside one insulated shield, better if polished, achieves a better thermal homogeneity and stability. Two flexible heaters are applied externally on the stainless steel vacuum chamber. I have implemented a digital control of the temperature of the copper shield as described in section 5.3 and [122]. The cavity is well insulated (time constant $> 40\,000\,\mathrm{s}$) and we are relying on the passive thermal property of the system to stabilize the cavity temperature on the short term.

As for temperature, the cavity should be isolated to vibrations. The cavity setup, the vacuum chamber, and part of the optics are placed on top of a passive vibration isolation platform (Minus-k BM8). The Minus-k platform strongly attenuate noise above 0.5 Hz for the vertical direction and above 1.5 Hz for the horizontal directions. Moreover this platform is arranged in an acoustic isolation chamber.

5.2.1 Optical setup

In the acoustic enclosure are placed the optics necessary for the Pound-Drever-Hall stabilization technique as shown in fig. 5.5. The 578 nm laser is delivered in the acoustic enclosure through a PM fiber. A local oscillator at 7 MHz drives the electro-optic modulator (EOM) that modulate the phase of the laser adding sidebands to the carrier frequency. The polarization of the yellow light entering the EOM is cleaned with a $\lambda/2$ waveplate and a polarizing beam-splitter cube. A telescope surrounds the EOM to improve the modulation. The modulated beam is then launched in the stable cavity through some beam-steering optics and two mode-matching lenses. The beam is coupled with the fundamental TEM_{00} mode of the cavity. About 60 µW are impinging on

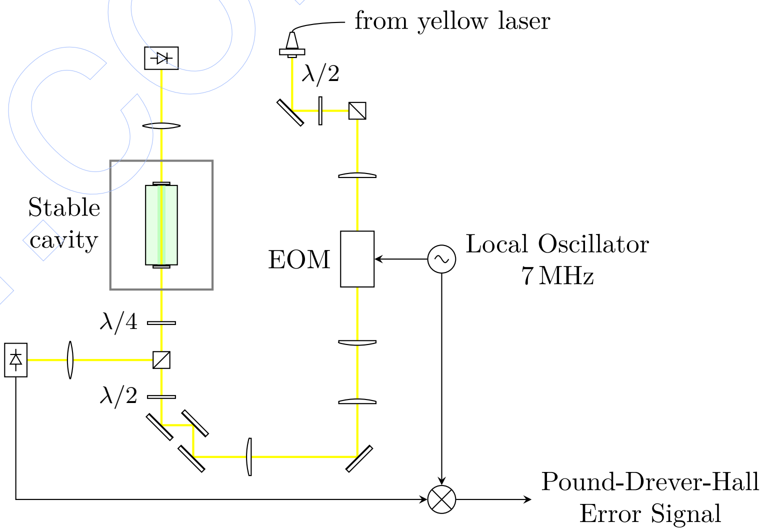

Figure 5.5: Schematics of the optics used for the Pound-Drever-Hall locking technique inside the acoustic enclosure.

the cavity. Before the cavity a $\lambda/2$ waveplate, a polarizing beam-splitter cube and a $\lambda/4$ waveplate form an optical isolator: the beam reflected from the cavity can then be extracted and delivered to a fast photodiode. The signal from this diode mixed with the frequency from the local oscillator gives the Pound-Drever-Hall error signal. The light transmitted from the cavity is monitored as well with another photodiode.

The frequency control is done with a double integrator scheme with two feedback channels (see fig. 5.6). The fast correction of the frequency of the laser is done with an AOM in double pass with a cat's eye retro-reflector [123]. The shifted laser beam is then launched in a PM fiber and delivered to the stable cavity. The slow control is obtained integrating again the signal from the proportional-integral-derivative (PID) controller sending it to the piezo of the 1030 nm fiber laser. The working point of the system is set giving a constant potential difference to the thermal control of the Nd:YAG laser at 1319 nm.

We have a second ULE cavity identical to the one described before. The second cavity comes with is own vacuum chamber, isolation platform, anti-acoustic chamber and optics for locking similar to the first one (fig. 5.7). Using two similar cavities allows us to measure the laser frequency noise, see section 5.5.

5.3 Temperature stabilization with ADRC

I describe here the application of a novel Active Disturbance Rejection Control (ADRC) to the temperature stabilization of the ultra-stable cavities. Details of this control have been presented in [122, 124].

ADRC was initially proposed by Han [125] using non-linear gains and then simplified

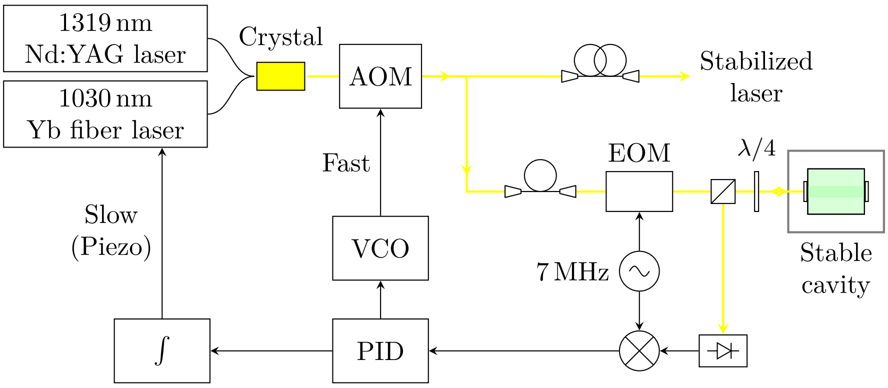

Figure 5.6: Schematics of the double-integrator servo for the Pound-Drever-Hall stabilization.

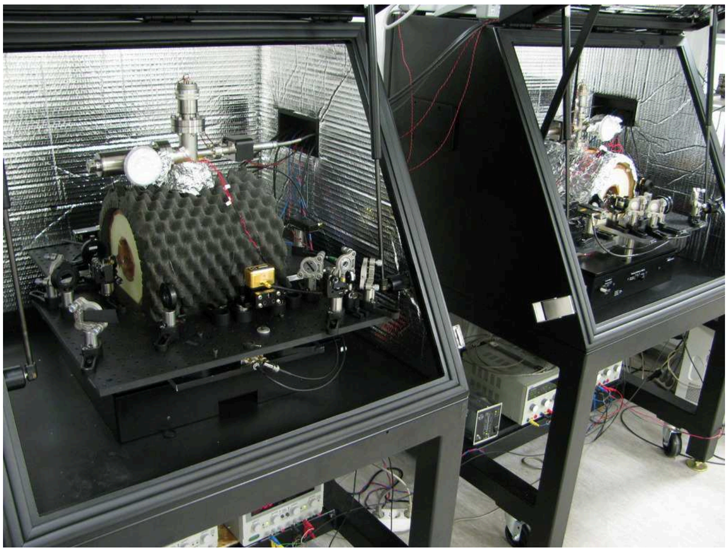

Figure 5.7: Picture of the two anti-acoustic chambers with the two setups for the ULE cavities.

by Gao [126, 127]. In its linear form, ADRC is a simple, easy, intuitive, and inherently robust form of control and can replace PID in most applications. I will show that ADRC is a feasible technology readily applied to problems related to the realization of clock lasers.

5.3.1 Active Disturbance Rejection Control overview

Before we analyze the thermal control it is convenient to review the theory behind ADRC. Consider a second order system, also known as plant, governed by the equation

$$\ddot{y} = bu + f(y, \dot{y}, u, \nu, t, \dots), \tag{5.12}$$

where y is the variable we want to control (output), u is the command (input), and b is a constant of the plant, at least approximately known. The function $f(y, \dot{y}, u, \nu, t, \dots)$, or simply f, is called the generic disturbance and can depend on the variable y and its derivative, the command, the time t, external noise ν and possibly other external variables. It accounts for internal dynamics of the plant, friction, noise, hysteresis, non-linearity, time dependencies, and it is generally unknown. Basically, the generic disturbance f accounts for any *uncertainty* in the system dynamics while ADRC only needs to know the order of the plant and coefficient b.

Equation (5.12) also describes a second order thermal system where y is the temperature, u is the power applied, and b parametrizes the fast frequency limit of the thermal transfer function.

The basic idea is that f can be estimated in real time and then it can be canceled in the command reducing the dynamics of the system to ta double integrator ($\ddot{y} \approx bu$).

We can rewrite the equation of our system $\ddot{y} = bu + f$ in a state equation for the vector $z = [y, \dot{y}, f]^\intercal$ where the state x is augmented by the presence of f. Then (5.12) becomes the matrix equation

$$\begin{aligned} \dot{x} &= Ax + Bu + Eh \\ y &= Cx \end{aligned} \tag{5.13}$$

where

$$A = \begin{bmatrix} 0 & 1 & 0 \\ 0 & 0 & 1 \\ 0 & 0 & 0 \end{bmatrix} \quad B = \begin{bmatrix} 0 \\ b \\ 0 \end{bmatrix} \quad E = \begin{bmatrix} 0 \\ 0 \\ 1 \end{bmatrix}$$

$$C = \begin{bmatrix} 1 & 0 & 0 \end{bmatrix}$$

and $h = \dot{f}$ is responsible for the unknown dynamics.

From this equation we construct a state observer for the variable $z = [\hat{y}, \hat{\dot{y}}, \hat{f}]^\intercal$, where $\hat{y}$, $\hat{\dot{y}}$ and $\hat{f}$ are the estimates of y, $\dot{y}$, and f respectively, that is

$$\begin{aligned} \dot{z} &= Az + Bu + L(y - \hat{y}) \\ \hat{y} &= Cz \end{aligned} \tag{5.14}$$

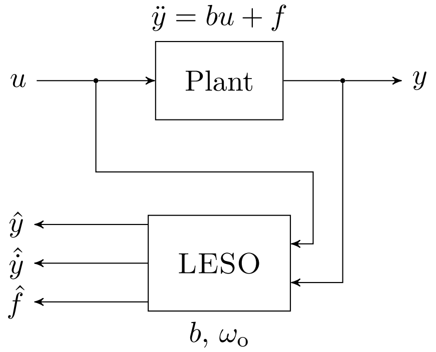

Figure 5.8: Schematic diagram of the physical system (plant) and of the linear extended state observer (LESO). The plant is assumed to be a second order system described by $\ddot{y} = bu + f$, where f is the generic disturbance. The LESO estimates the plant output $\hat{y}$, its derivative $\hat{\dot{y}}$ and the generic disturbance $\hat{f}$.

where the observer gain vector $L = [l_1, l_2, l_3]^\intercal$ replaces the unknown dynamic in (5.13). Equation (5.14) describes the extended state observer (ESO), or sometimes linear extended state observer (LESO) when we want to underline the use of linear gains (see fig. 5.8). When properly implemented, the state of the LESO z will track the state of the plant x [126, 127].

As shown by Gao [126], we can parametrize the LESO choosing the three gains in L so that all the observer eigenvalues are $-\omega_\mathrm{o}$. That is, imposing $\det\left[sI - (A - LC)\right] = (s + \omega_\mathrm{o})^3$, we obtain $L = [3\omega_\mathrm{o}, 3\omega_\mathrm{o}^2, \omega_\mathrm{o}^3]^\intercal$. The LESO is simply characterized only by the parameter b and by the observer bandwidth ω_o. The former is usually known or can be measured from the open loop response. The latter can be tuned looking for a compromise between performances and noise sensitivity.

Once the LESO is set up it is easy to design a controller for the plant. We write the control law as

$$u = u_0 - \hat{f}/b, \tag{5.15}$$

so that (5.12) becomes

$$\ddot{y} = bu + f = bu_0 - \hat{f} + f \approx bu_0. \tag{5.16}$$

We used $\hat{f}$ to cancel out the contribution from f thus reducing the system dynamics to approximately the double integral plant (5.16). This can be easily controlled by a proportional-derivative (PD) controller of the form

$$bu_0 = k_\mathrm{p}(r - \hat{y}) - k_\mathrm{d}\hat{\dot{y}}, \tag{5.17}$$

where r is the desired set point (see fig. 5.9). Equation (5.16) has a simple form and we can impose the gains

$$k_\mathrm{p} = \omega_\mathrm{c}^2, \quad k_\mathrm{d} = 2\omega_\mathrm{c}. \tag{5.18}$$

so that the closed loop poles of (5.16) lay at the control bandwidth ω_c. In fact, substituting (5.17) in (5.16) and assuming z tracking x we can write the closed loop transfer

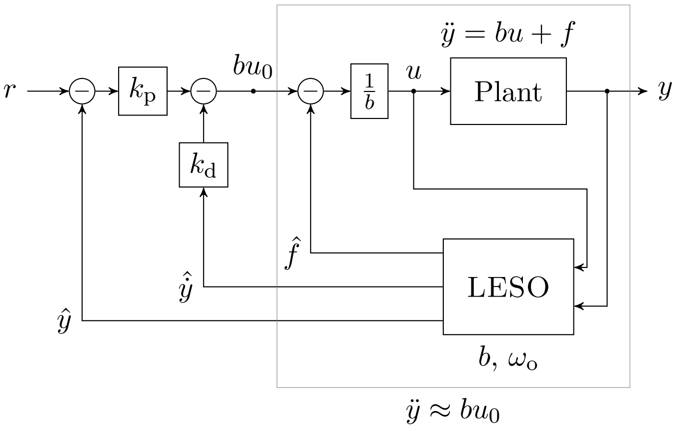

Figure 5.9: Schematic diagram of ADRC. Using $\hat{f}$ to cancel out the contribution from f, the plant is reduced to a simpler double integrator system and can be controlled by a PD controller parameterized by a single bandwidth ω_c.

function between r and y in the frequency domain ($s = j\omega$)

$$G(s) = \frac{k_\mathrm{p}}{s^2 + k_\mathrm{d} s + k_\mathrm{p}} = \frac{\omega_\mathrm{c}^2}{(s + \omega_\mathrm{c})^2}. \tag{5.19}$$

Note that this PD control is always, at least approximately, critically damped.

It should be remarked that design and tuning are model independent: only an approximate value of parameter b is needed. ADRC is easy to tune, acting only on the two parameters ω_o and ω_c, both of which have the simple physical meaning of bandwidths. Increasing ω_o increases the disturbance rejection at the expense of a greater sensitivity to noise. Increasing ω_c allows the control to follow the set point faster but increases sensitivity to noise and noise in the command.

Using estimate $\hat{f}$, the ADRC controller achieves zero steady-state error with constant set point without using an integrator. Instead of integrating the error signal, like in a traditional PID, ADRC integrates the difference between the measured output of the plant and the ideal response of the LESO

$$\hat{f} = \omega_\mathrm{o}^3 \int (y - \hat{y}) \mathrm{d}t. \tag{5.20}$$

This achieves zero steady-state error but avoids typical problems encounter with integral controls like integral windup and overshoot.

Stability and convergence of the LESO estimation error and of the ADRC closed-loop tracking error can be formally demonstrated assuming h is limited [128].

5.3.2 Implementation of the control

The control works on the temperature of the copper shield surrounding the ULE cavity. In the vacuum chamber there are two negative temperature coefficient (NTC) thermistors

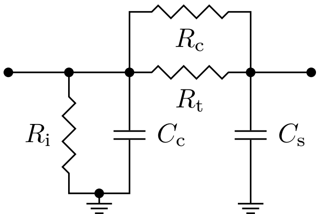

Figure 5.10: Equivalent circuit of the thermal properties of the system.

(see fig. 5.4). The first is thermally in contact with the copper shield and is the sensor in the control loop. The second thermistor is used as a monitor and is placed on a piece of glass below the cavity. No thermistor is placed on the cavity itself preserving the good mechanical property of the ULE glass.

We control the temperature of the copper shield with a PC program written in Python. A multimeter reads the resistance value of the thermistor. The software reads the instrument measurements through a GPIB interface every 2 s. It performs the ADRC calculations in discrete time, using a current estimator with a zero order hold approximation, designed as in Miklosovic et al. [129]. The commands calculated are then converted to analog signals that drive the heaters around the vacuum chamber. The sampling time of 2 s minimizes the dead time in the measurement of the thermistors.

5.3.3 Performances of the control

Tuning of ADRC involves an approximate knowledge of the fast frequency response parameter b. For example it can be estimated from a simple thermal equivalent circuit of the system (fig. 5.10). In the figure C_c is the thermal capacity of the vacuum chamber, R_i is the thermal resistance to the external world, C_s is the capacity of the thermal shield, R_c is the resistance between the shield and the vacuum chamber coming from the conduction through the support screws, and R_t is the resistance from thermal black body radiation. From this circuit, a second order equation in the form of eq. (5.12) can be obtained. The parameter b is then

$$b = \frac{1}{C_c R_p C_s}, \tag{5.21}$$

where R_p is the parallel between R_c and R_t.

Our initial estimate was $C_c = 9 \times 10^3\,\mathrm{J/K}$, $R_i = 6\,\mathrm{K/W}$, $C_s = 8 \times 10^2\,\mathrm{J/K}$, $R_c = 33\,\mathrm{K/W}$, $R_t = 29\,\mathrm{K/W}$ resulting in $b = 9 \times 10^{-9}\,\mathrm{K/(W\,s^2)}$.

I run computer simulations to study the system as ADRC depends only weakly on the characteristics of the plant. I used the simulations to learn the control and to obtain a first estimate of the parameters involved.

I also measured the value of b from the thermal transfer function of the system. I applied sinusoidal power to the heaters measuring at the same time the temperature of the thermistor. For each frequency a computer program allowed us to extract the in-phase and out-of-phase responses of the temperature and, sorting out transient behaviors,

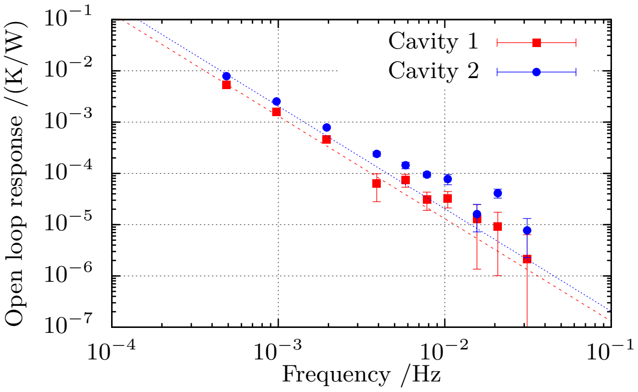

Figure 5.11: Thermal transfer function of the two setups. The lines show fits for the fast frequency response $b/(2\pi\nu)^2$, where ν is the frequency.

Table 5.1: Final parameters for the controls for the two setups.

	Cavity 1	Cavity 2
b	$5.2 \times 10^{-8}\,\mathrm{K/(W\,s^2)}$	$8.1 \times 10^{-8}\,\mathrm{K/(W\,s^2)}$
ω_o	$8 \times 10^{-3}\,\mathrm{rad/s}$	$6 \times 10^{-3}\,\mathrm{rad/s}$
ω_c	$15 \times 10^{-3}\,\mathrm{rad/s}$	$15 \times 10^{-3}\,\mathrm{rad/s}$

to reconstruct the transfer function. The results are shown on fig. 5.11: the two sets of data correspond to the two, practically identical, setups. The data are fitted with the function $b/(2\pi\nu)^2$ where ν is the Fourier frequency.

Table 5.1 shows the measures of b from the fit and the values of the bandwidths used in our control. A maximum command of 8 W is imposed to limit the current in the heaters. The total command is thus limited between 0 W and 8 W and the software applies the same limits to the input of the LESO. With these limits, we can set the temperature between 24 °C (approximately the temperature in the anti-acoustic chamber) up to 45 °C.

We can deduce the performances of the control applying steps in the set point. An example is shown in fig. 5.12 for a set point change of 400 µK. The temperature of the shield follows closely the set point and a simple exponential fit is shown. The time constant of the exponential decay is 172(7) s and is the correct order of magnitude for a second order system with bandwidth $\omega_\mathrm{c} = 0.015\,\mathrm{rad/s}$.

The same figure shows the behavior of the $\hat{f}$ output of the LESO and its contribution during the step. Moreover at around 8 h we opened the cover of the acoustic-isolation enclosure holding the experiment: $\hat{f}$ changes with the system keeping the temperature at the desired set point.

The command can saturate at 0 W or 8 W when applying greater changes in the set point (see fig. 5.13). When we want to change the temperature of the cavity with a step greater than 1 mK we use a smooth transition in the set point to prevent saturation. As suggested by Gao [126], using such a smooth motion profiles allows us to increase the

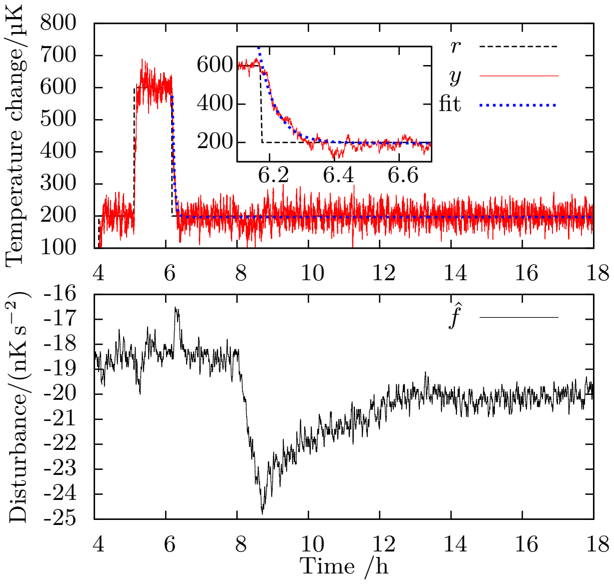

Figure 5.12: Response to the temperature of the shield to steps of 400 µK. The response of y follows closely that of r. The inset shows a detail of the second step, with a simple exponential fit. The bottom panel shows the estimate $\hat{f}$: at around 8 h the enclosure holding the cavity was opened and $\hat{f}$ reflects this change with little impact on the controlled temperature.

aggressiveness of the control without the command hitting its limit, while the system is effectively under control for the duration of the transition. Figure 5.13 shows set point, measured temperature, and command during three transitions. The insets show the end of the profiles: the ratio between the overshoot and the step is about 10^{-4}. The rise time of the smooth profile was 11 h. The spikes in the command are due to a bug in the GPIB communication with the digital multimeter: sometimes the software is unable to read the instrument and stops for two iterations. This bug happens only when the temperature is changing and does not affect the steady state performances of the control.

Figure 5.14 shows the instability of the temperature of the shield (measured in loop) expressed as overlapping Allan deviation [7, 130, 131]. The set point was 25.5 °C during the measurement, in quiet environment. The total measurement time was 11 days; data were recorded every 2 s by the computer program that performs the control. At averaging time $\tau = 2\,\mathrm{s}$ the noise of the multimeter limits the instability value. The control starts working between $\tau = 100\,\mathrm{s}$ and $\tau = 200\,\mathrm{s}$ (that is approximately $1/\omega_\mathrm{o}$) and the noise decreases with averaging time.

The same figure shows the instability of the monitor temperature (of the other thermistor in the chamber). This temperature usually varies less than 0.5 mK on a day by day basis. It has been measured for 100 h every 1 s. The overlapping Allan deviation is 150 µK at one day of integration time.

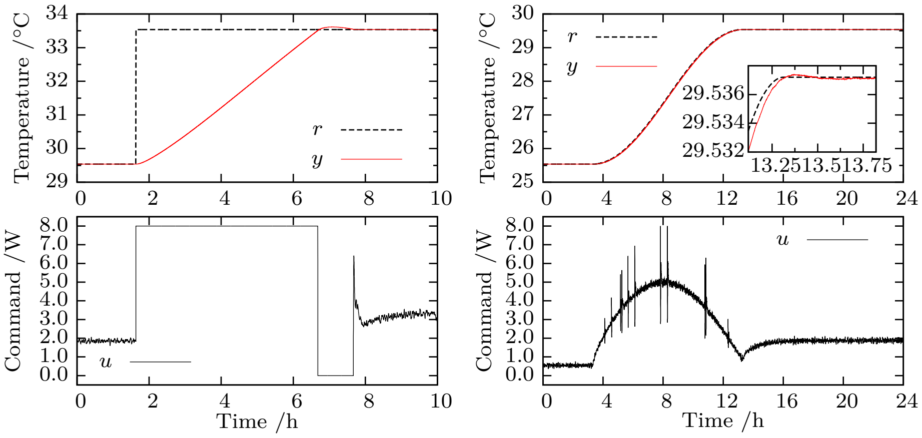

Figure 5.13: Responses to changes in the set point: left, response of temperature of the shield to a hard step in the set point; right, response of the temperature of the shield to a smooth step. The inset shows the end of the step. Bottom panels show the power applied during the transitions.

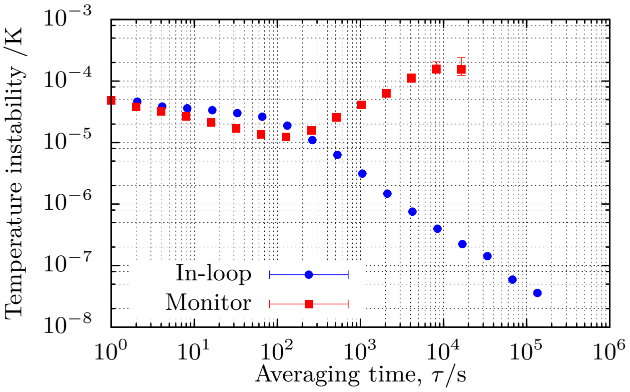

Figure 5.14: Overlapping Allan deviation of the temperature of the thermal shield (in-loop measurement) and of the monitor thermistor.

Table 5.2: Summary of the ring-down experiment result on both cavities.

	Cavity 1	Cavity 2
$\tau/\mu s$	16.0(1)	23.8(4)
$\Delta\nu$ /kHz	9.93(6)	6.69(12)
$\mathcal{F}$	$151(1) \times 10^3$	$224(4) \times 10^3$
Q	$5.22(3) \times 10^{10}$	$7.7(1) \times 10^{10}$

5.4 Measurements

5.4.1 Seismic and acoustic noise

The noise reduction effects of the isolation platform Minus-k and of the acoustic chamber are shown in fig. 5.15, as measured with a seismograph. Integrating the acceleration noise in a 100 Hz bandwidth we obtain a root mean square acceleration $a_{\mathrm{rms}} = 1.2 \times 10^{-4}$ m/s^2. The platform is effective at reducing the seismic noise above 1 Hz; it allows between 10 and 20 dB of insulation depending on the Fourier frequency.

5.4.2 Ring down time measurement

The finesse $\mathcal{F}$ of the stable Fabry-Pérot cavity can be measured with a ring-down experiment. The yellow laser is locked to the resonance of the Fabry-Pérot so that the standing wave is stored inside the cavity. An electronic switch is used to quickly turn off the the laser, shutting down the RF piloting the AOM (the switch responds in 40 ns, the AOM rise time is about 200 ns). The light transmitted by the cavity is monitored with a fast photodiode (bandwidth 5 MHz).

An example of the transmission data obtained is reported in fig. 5.16. The transmission decay is fitted with an exponential curve, so that the intensity of the transmitted light goes as $I \sim \mathrm{e}^{-t/\tau}$, where τ is the ring-down time of the cavity. We repeated the ring-down measure 5 time for both cavities. From the ring-down time we can compute the linewidth

$$\Delta\nu = \frac{1}{2\pi\tau},$$

the finesse

$$\mathcal{F} = \frac{\Delta\nu_{\mathrm{FSR}}}{\Delta\nu} = \frac{2\pi c}{L}\tau,$$

and the quality factor

$$Q = \frac{\nu}{\Delta\nu} = \frac{2\pi c}{\lambda}\tau,$$

where c is the speed of light, L the length of the cavity, and ν and λ frequency and wavelength of the yellow radiation. Results are summarized in table 5.2.

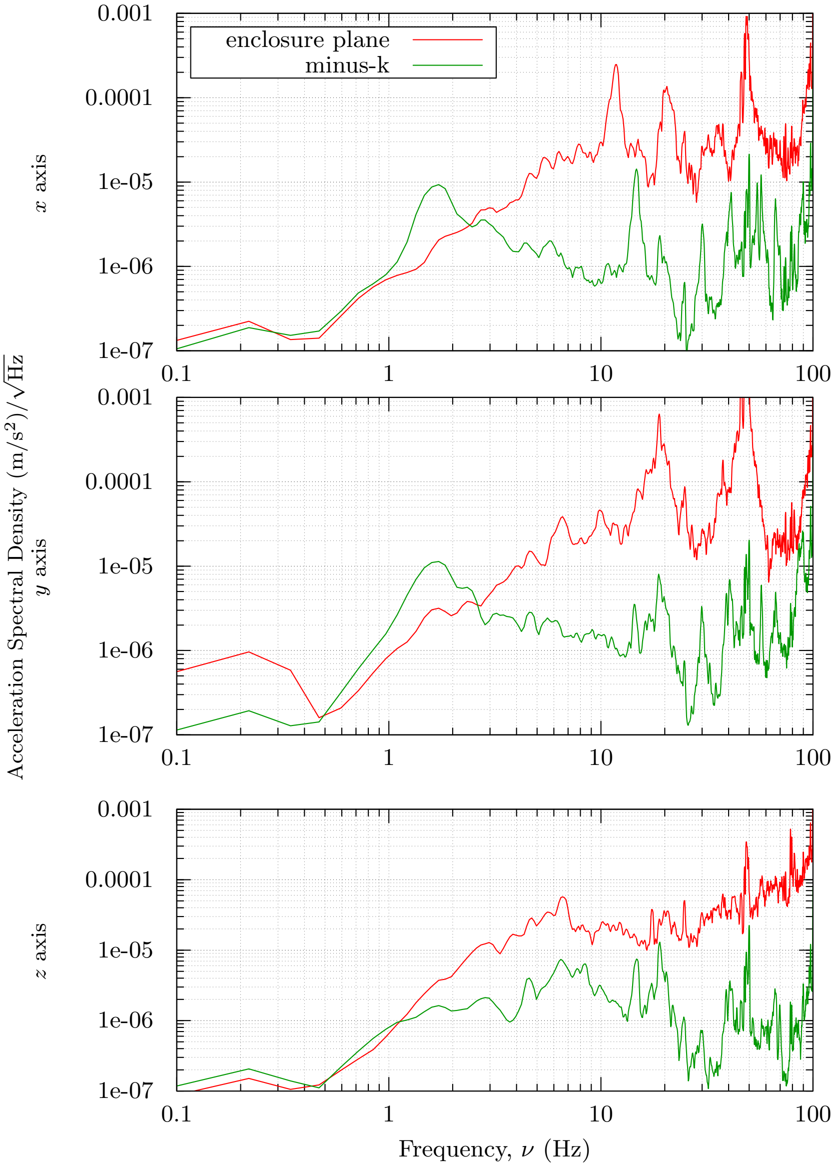

Figure 5.15: Acceleration spectral density along the horizontal axes (x and y) and along the vertical axis (z) showing the seismic noise on the chamber working plane and on top of the vibration isolation platform, with closed acoustic chamber.

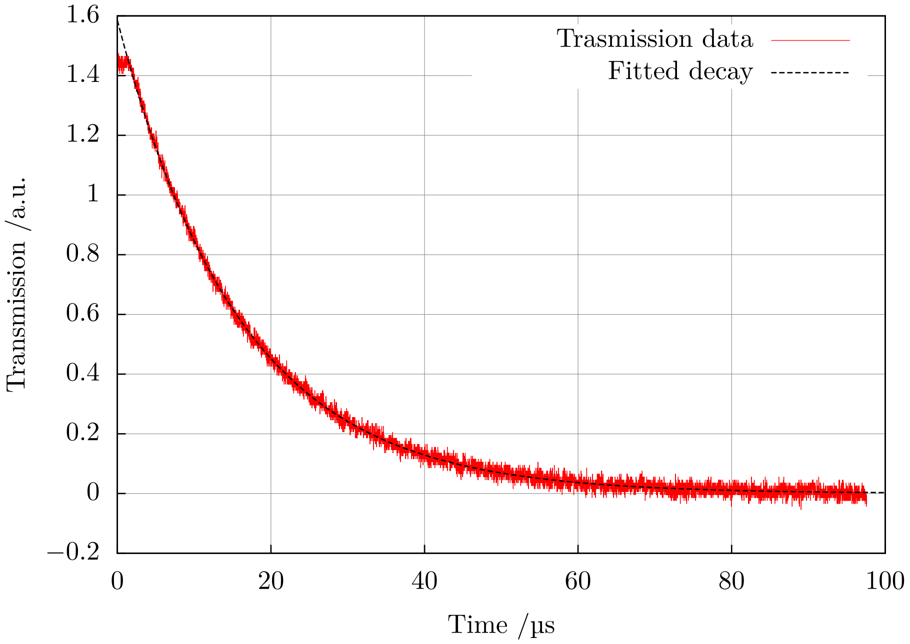

Figure 5.16: Example of a ring-down time measurement obtained with an oscilloscope. An exponential decay fit is shown.

5.4.3 Double pass AOM

The efficiency of the double pass and of the fiber launch is shown in fig. 5.17 as a function of the RF applied to the AOM. The observed bandwidth (full width at half maximum) is 40 MHz. It should be noted that, being the AOM used in double pass, the shift of the laser frequency is double that of the RF frequency. At center frequency the total efficiency of the system is 35 % resulting by, approximately, 85 % coupled in the first pass of the AOM, 60 % coupled with the second pass and 70 % of coupling with the fiber.

5.4.4 Pound-Drever-Hall signal

The transmitted mode of the cavity and the Pound-Drever-Hall error signal obtained sweeping the frequency of the laser with the AOM are shown in fig. 5.18. These plots show the sidebands added at 7 MHz by the EOM. The linewidth of this signals is around 20 kHz. Since the line of the cavity has a width of 10 kHz this suggests a linewidth of the yellow laser of the order of 10 kHz (combined from the linewidths of the 1319 nm and 1030 nm lasers). The peak-peak excursion of the Pound-Drever-Hall error signal is usually more than 200 mV and we estimate the maximum slope of the signal as $k_{\mathrm{PDH}} \simeq 20\,\mu\mathrm{V/Hz}$.

The beam impinging on the cavity has to be carefully aligned for good coupling with the fundamental mode of the cavity. The distribution of light in a laser beam is usually described by Hermite-Gaussian functions referred as transverse electromagnetic modes

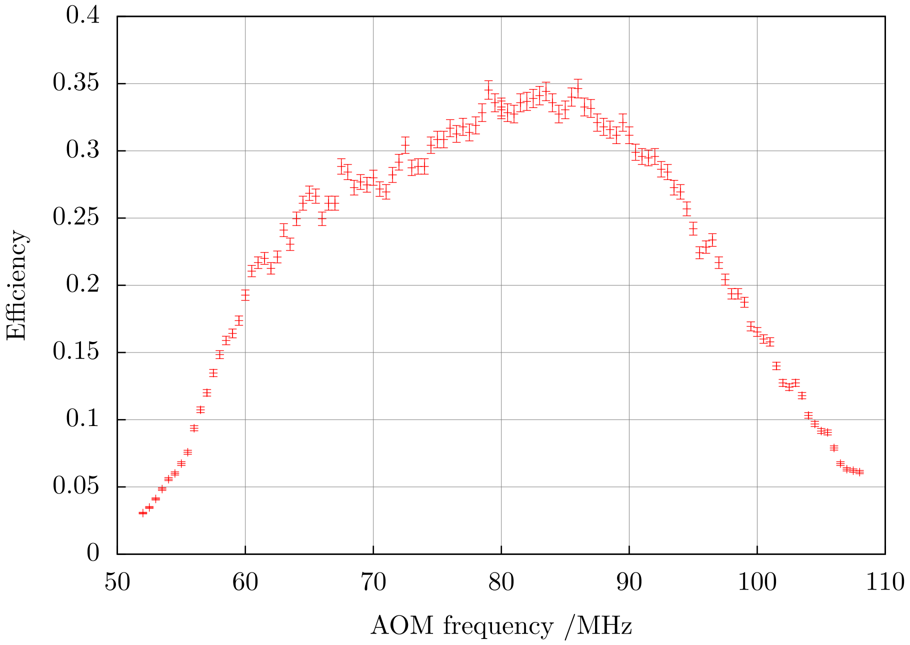

Figure 5.17: Diffraction efficiency of the double pass AOM and of the fiber launch.

(TEM)[71]. The fundamental mode is the TEM_{00}. A charge-coupled device (CCD) camera used to observe the transmitted light from the cavity is useful to recognize the correct mode; otherwise higher order mode can be observed and locked to (fig. 5.19).

5.4.5 Thermal characteristic

ULE has a zero in the CTE around room temperature. To roughly estimate its value a linear temperature ramp is applied to the shield of only one of the cavities while the other acts as reference. The beat note between the two cavities is measured as a function of temperature. Aside from an exponential transient and a time lag, the temperature of the cavity itself should vary linearly, as the temperature ramp. The beat note between the laser radiations locked on the two cavities is quadratic versus the temperature of the test cavity because it follows fromeq. (5.2), and the vertex of the parabola corresponds to the zero CTE point. A quadratic fit of the data allows evaluation of this temperature at about 20(1) °C, as shown in fig. 5.20. Unfortunately, this temperature is below room temperature, and hence it was not possible to tune the cavity to this temperature, because the implemented temperature control uses only heating components. A large uncertainty is given because the vertex of the parabola was not directly measured and the method needs further improvements; in particular a better measurement could result from a long acquisition of data for a week or more and using two ramps, one heating and one cooling the cavity [112].

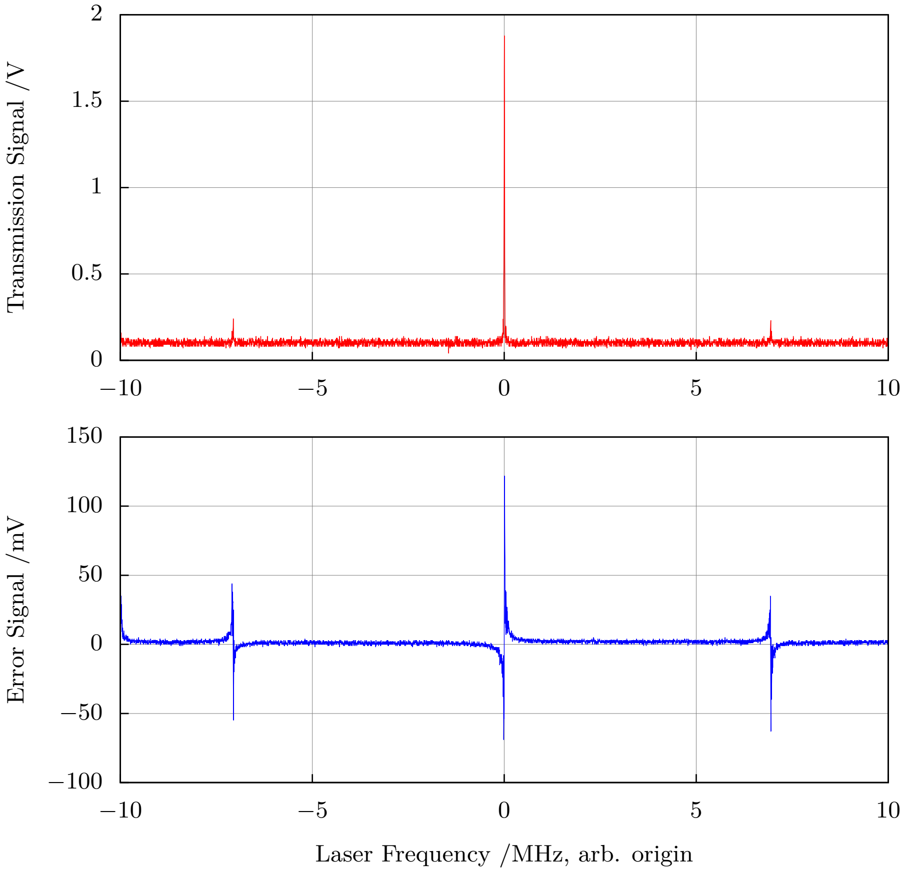

Figure 5.18: Transmission of the cavity showing the mode of the laser with the sidebands added at 7 MHz by the EOM and Pound-Drever-Hall error signal obtained modulating the frequency of the yellow laser with the AOM.

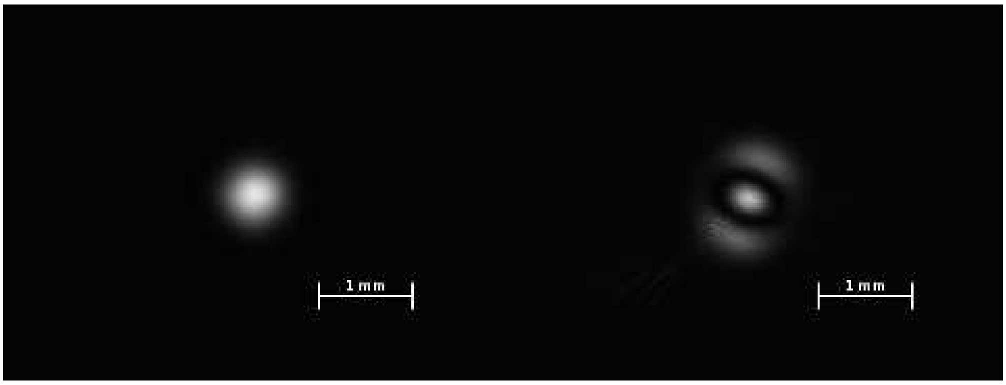

Figure 5.19: Transmitted cavity modes observed with a camera. Left, cavity well aligned in the TEM_{00} mode; right, higher order mode with prevalence of the TEM_{10} component.

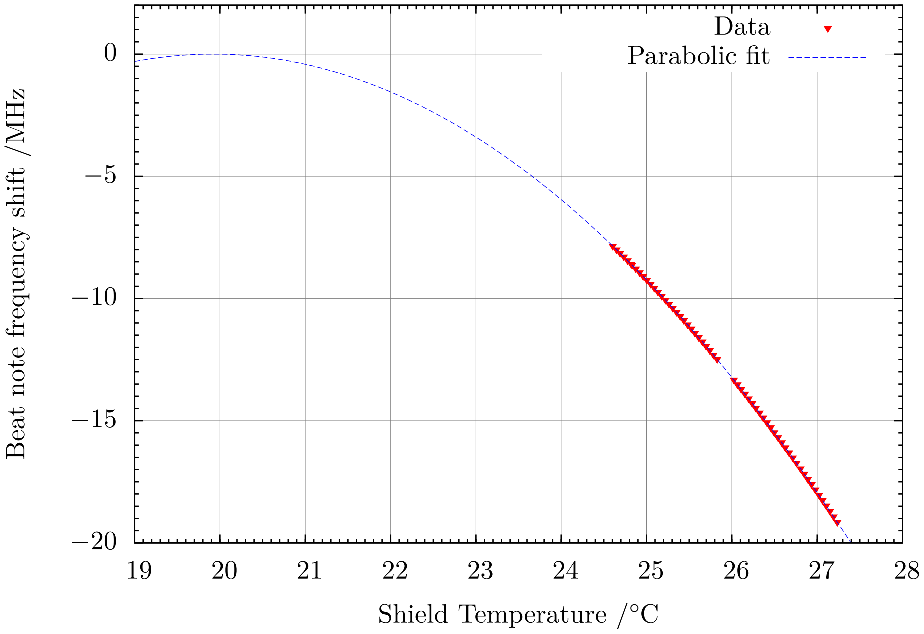

Figure 5.20: Frequency of the beat note, changing one cavity temperature to measure the cavity zero CTE point. Data in the graph are down-sampled with respect to raw data.

5.5 Characterization of the laser noise

The setup for the characterization of the laser noise is shown in figs. 5.21 and 5.22. Two different beams from the yellow laser generated by the PPLN crystal are stabilized on the two ULE cavities using two independent AOMs. The feedback from cavity 1 is used to correct the slow drift of the laser acting on the piezo of the 1030 nm fiber laser. A third AOM is used to bridge the frequency gap between the two cavities.

The two laser beams, stabilized against the two cavities, are extracted before the optical fibers delivering them to the acoustic-isolation chambers and are superimposed on a fast photodiode. The resulting beat note is then filtered, amplified, down-converted and counted using a hydrogen maser as a reference. The noise of the two lasers is independent within the bandwidth of the two controls.

The bandwidth of the control is about 120 kHz as measured observing the spectrum of the beat note reported in fig. 5.23 [132]. This bandwidth is limited by the delay introduced by the AOMs in the loop ($t_\mathrm{d} \approx 0.5\,\mu\mathrm{s}$). A close up scan of the beat note shows a lorentzian line profile of 3.8(1) Hz width that correspond to a single laser linewidth $< 2\,\mathrm{Hz}$ (fig. 5.24). The observed line broadens if the sweep time is increased; we choose the bandwidth that does not attenuate the peak power.

Figure 5.25 reports the overlapping Allan deviation of the beat note frequency [130, 131]. The measurements have been performed with and without the vibration isolation platform Minus-k using a counter. The Allan deviation shows that the presence of the

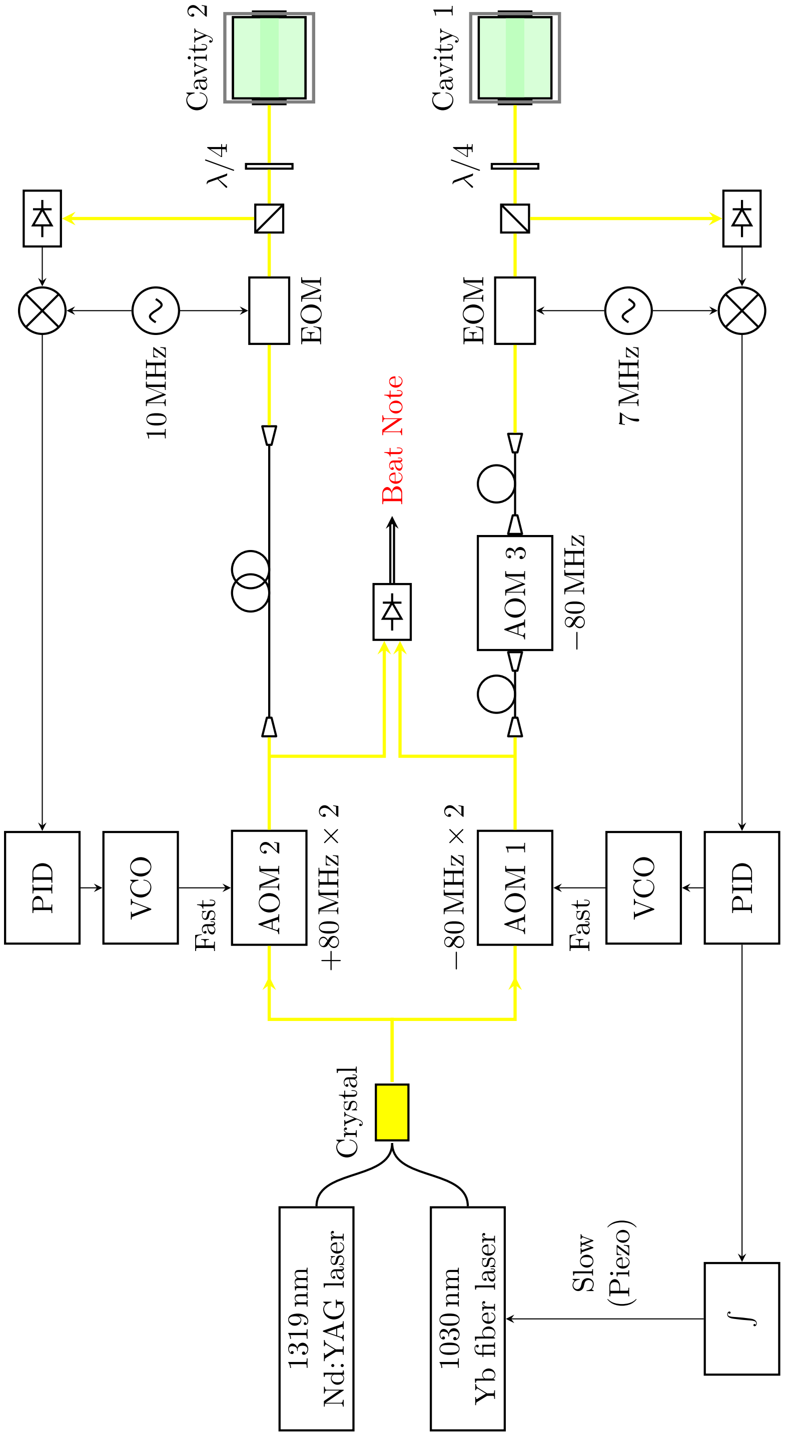

Figure 5.21: Scheme for the measurement of the frequency stability of the beat between two ULE cavities.

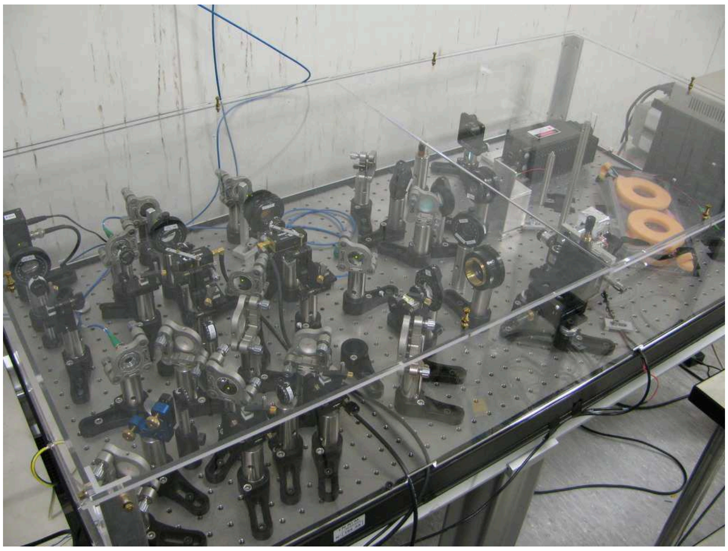

Figure 5.22: Picture of optical bench for the comparison of the two cavities.

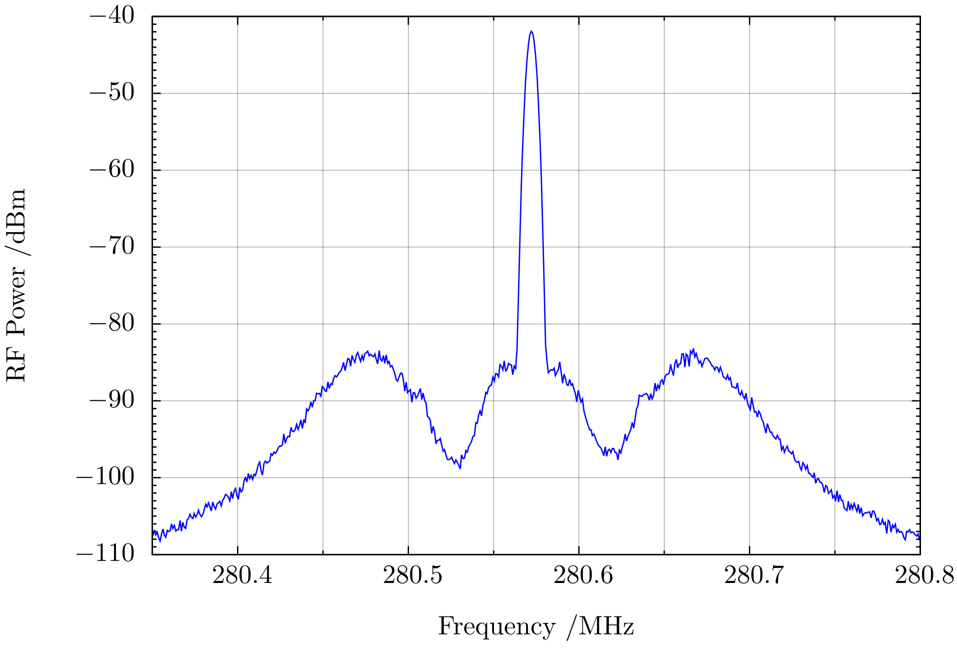

Figure 5.23: Beat note spectrum between the two independent locked lasers. Resolution Bandwidth 4.7 kHz, Span 500 kHz, Sweep Time 86 ms. The control loop bandwidth is evaluated to be 150 kHz.

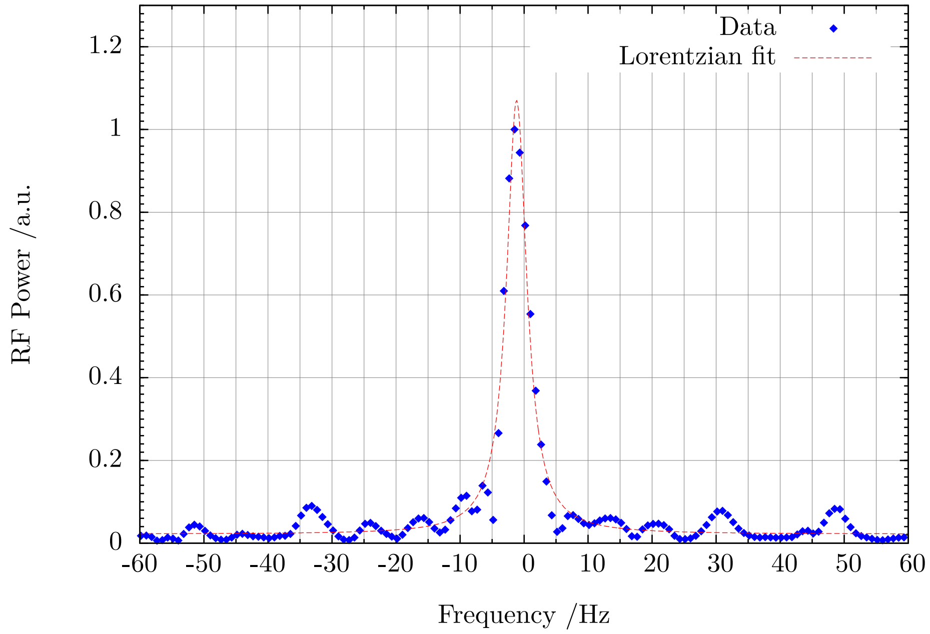

Figure 5.24: Beat note spectrum between the two independent locked lasers showing a linewidth of 3.8 Hz. Resolution Bandwidth 3 Hz, Span 500 Hz, Sweep Time 617 ms.

damping platform is outstanding for short integration time. The deviation shown for longer averaging time is consistent with a 0.8 Hz/s linear drift. After the drift removal, the flicker floor of the beat note instability is 4×10^{-15}. This corresponds to an estimated stability for each laser of 2.8×10^{-15}, assuming the two systems identical.

The drift is due to temperature non-uniformity in the chamber because we are not able to work at the zero CTE temperature of the cavities.

The measured flicker floor is about a factor of 4 higher than expected from thermal noise. The extra flicker noise is likely due to the optical power fluctuations in the Fabry-Pérot cavity. This phenomenon may be caused by a coating absorption or a radiation pressure effect [21, 133]. The frequency sensitivity $h(f)$ to absolute fluctuations of the power transmitted by the cavity at low frequencies ($f \ll \mathit{\Delta}\nu_{\mathrm{FSR}}$) can be approximated as

$$h(f) = L^{-1} K_P \mathcal{F} \nu_0, \tag{5.22}$$

where L is the length of the cavity, $\mathcal{F}$ its finesse, ν_0 the laser frequency and K_P a conversion parameter that depends on the details of the mirror and on the waist size.

The transmitted power is 12 µW (a fraction 20 % of the incident power). The relative power instability is evaluated to be $< 4 \times 10^{-3}$ for averaging time τ between 1 s to 20 s; this is limited by noise introduced by the PM fiber that bring the yellow laser on the cavities. The observed flicker floor instability is compatible with a frequency sensitivity $h(f) = 75\,\mathrm{Hz/\mu W}$ and a conversion parameter $K_P = 5.8 \times 10^{-20}\,\mathrm{m/\mu W}$. This latter value is larger than the values reported in [21], but it is consistent with the

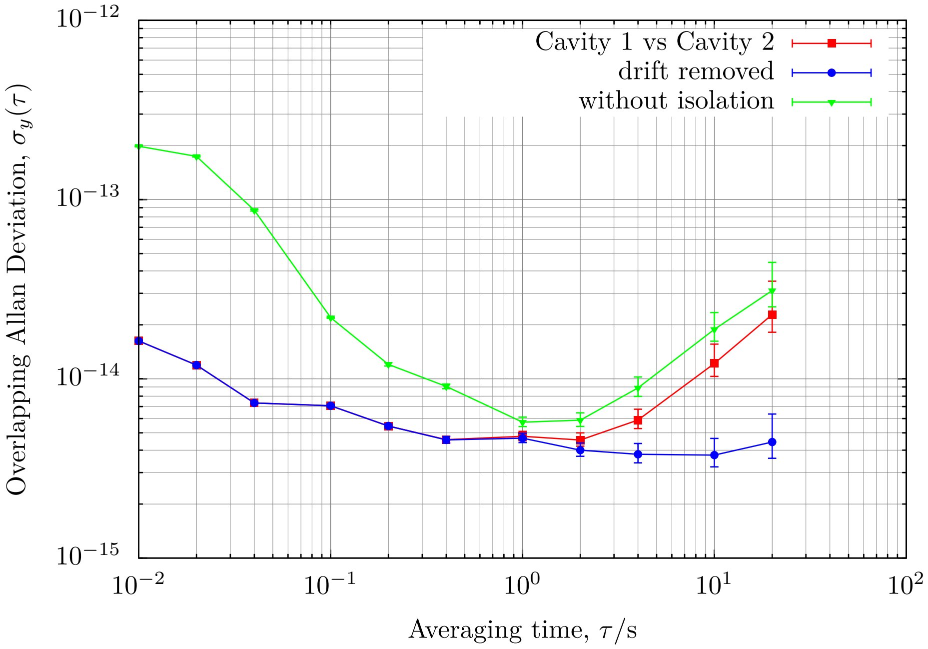

Figure 5.25: Allan deviation of the lasers beat note: with and without seismic damping table activate, with seismic damping and 0.8 Hz/s drift removed. Lines are here only to guide the eye.

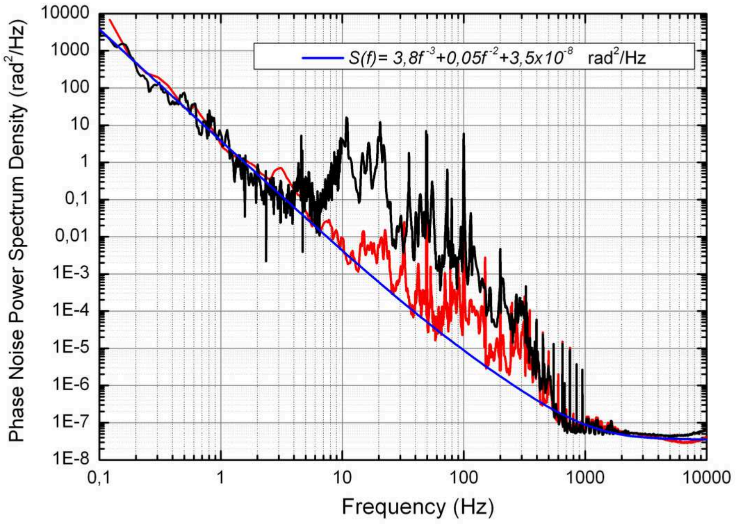

Figure 5.26: Phase noise power spectrum density of the beat note. Red, with seismic isolation platform; black, without seismic isolation platform; blue, base line fit.

value measured in in an experiment based on two Fabry-Pérot cavities resonating at 1542 nm with the same geometry and materials as the cavities I have described [62].

Figure 5.26 shows the phase noise power spectral density of the laser. The phase noise spectrum has been measured using a phasometer. A frequency divider (scale factor 40) is necessary to manage the high phase noise power at low Fourier frequencies. The baseline of the lower spectrum is fitted by the polynomial

$$S_\varphi(f) = b_{-3}f^{-3} + b_{-2}f^{-2} + b_0, \tag{5.23}$$

with $b_{-3} = 3.8\,\mathrm{rad}^2\ \mathrm{Hz}^2$, $b_{-2} = 5 \times 10^{-2}\,\mathrm{rad}^2$ Hz and $b_0 = 3.5 \times 10^{-8}\,\mathrm{rad}^2\ \mathrm{Hz}^{-1}$. For a power-law spectrum b_{-3} corresponds to flicker frequency noise, b_{-2} to white frequency noise, and b_0 to white phase noise [130]. The flicker frequency value is compatible with the 4×10^{-15} floor observed on the Allan deviation.

In the spectral range between 10 Hz and 1000 Hz is evident an excess of noise with respect to the fitting baseline due to acoustic and seismic noise. The noise increases in the 10 Hz to 1000 Hz range without the vibrations damping by the platform, . Two peaks at 10 Hz and 20 Hz are observed with a power of about $20\,\mathrm{rad}^2\ \mathrm{Hz}^{-1}$. These two peaks are caused by the seismic vibrations (fig. 5.15), where the measured acceleration spectrum of the cavity box floor shows peaks at the same frequencies along the x and y directions. Using these peaks, the experimental vibration sensitivity of the cavities is measured to be about $3 \times 10^{-10}\,\mathrm{s}^2\ \mathrm{m}^{-1}$ not the lowest possible as evaluated by the FEM. The discrepancy is probably due to imperfect contacts or a displacement of the supporting pads position from the optimum up to 1 mm.

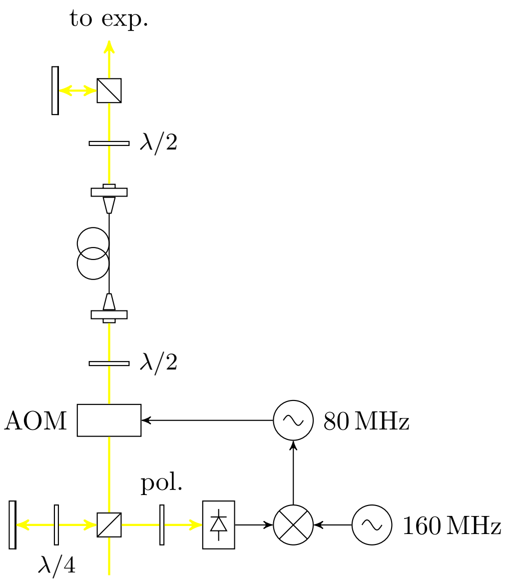

Figure 5.27: Setup for fiber noise cancellation.

5.6 Fiber link

Optical fibers introduce phase noise on the laser because of vibrations, temperature, and polarization variations [134]. We are using PM fibers to deliver the 578 nm laser to the cavities and I have studied the noise they introduce. This noise can be detected and cancelled reflecting back the laser at the fiber end and comparing it with the original source [61, 135]. I have implemented a simple cancellation of the fiber noise to transfer the clock across the lab. It should be noted that similar techniques have been extensively studied in recent years because they allow the accurate transfer of an optical frequency over long distances up to several hundreds of kilometres of fiber links [62, 105, 136, 137].

The setup used for fiber noise cancellation is shown in fig. 5.27. The setup is basically a small Michelson interferometer using a beam-splitter cube. On one arm of the interferometer, the 578 nm laser is sent in an AOM and coupled in a PM fiber. The polarization of light is aligned to the slow axis of the fiber using a $\lambda/2$ waveplate. After the fiber, part of the light is spilled and backreflected using a beam-splitter cube. The fraction of light transmitted and reflected can be changed using a $\lambda/2$ waveplate (see fig. 5.28). The other arm of the interferometer acts as a reference and it is simply made by a mirror and a $\lambda/4$ waveplate. The light backreflected from both arms is sent through a polarizer and beat on a fast photodiode.

The frequency of the beat note is twice the shift of the AOM, i.e., 160 MHz. This frequency is filtered, amplified, and down-converted using a local oscillator at 160 MHz. The down converted signal pilots the voltage-controlled oscillator (VCO) at 80 MHz that drives the AOM. In practice the beat note is phase-locked to the local oscillator.

In this configuration we can describe the noise cancellation introducing the Fourier

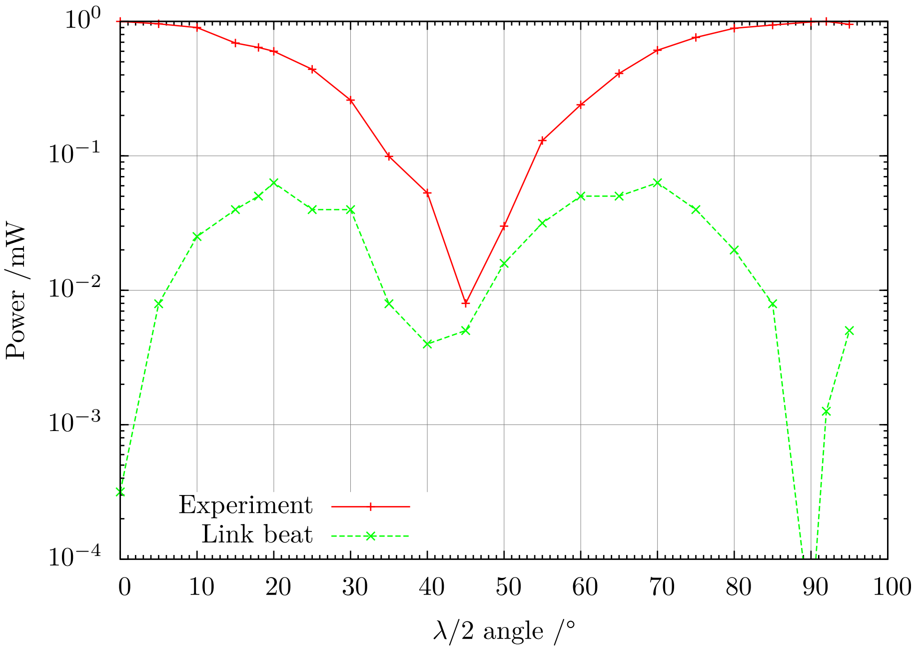

Figure 5.28: Power available for the experiment and power of the link beat note as a function of the angular position of the $\lambda/2$ waveplate. Lines are here to guide the eye.

transform of the phase noise introduced by the fiber $\phi_\mathrm{F}(f)$ and by the AOM $\phi_0(f)$, where f is the Fourier frequency. The phase noise at the end of the fiber is then $\phi_\mathrm{end} = \phi_\mathrm{F} + \phi_0$. The beat at 160 MHz contains twice the noise introduced by the fiber and the AOM so that the output of the mixer is proportional to $2(\phi_\mathrm{F} + \phi_0)$. The frequency that drives the AOM is $\nu_0 = -\mathrm{i} f \phi_0$, so when the loop is closed

$$- \mathrm{i} f \phi_0 = 2k(\phi_\mathrm{F} + \phi_0), \tag{5.24}$$

where k is a constant that depends on the characteristics of the mixer and of the VCO. We have then

$$\phi_0 = -\frac{G(f)\phi_\mathrm{F}}{1 + G(f)}, \tag{5.25}$$

with the the gain $G(f) = 2k/(\mathrm{i}f)$. At low frequency, for $G \gg 1$, $\phi_0 \simeq -\phi_\mathrm{F}$ so that the noise is cancelled also at the remote end of the fiber and $\phi_\mathrm{end} \simeq 0$.

To test the performances of the noise cancellation, I mounted both collimators of the fiber on the same table and beat the light passed through the fiber with the original laser on another fast photodiode. The stability of the fiber link, with and without noise cancellation, is shown in fig. 5.29 for a fiber length of 8 m. The fiber is placed along the wall of the lab, as the working conditions of the fibers used for the clock stabilization. Open loop, without noise cancellation, it is evident the excess of noise at 200 s caused by the cycle of the air conditioner of the lab. Close loop the noise is cancelled and the stability decrease with averaging time as white noise.

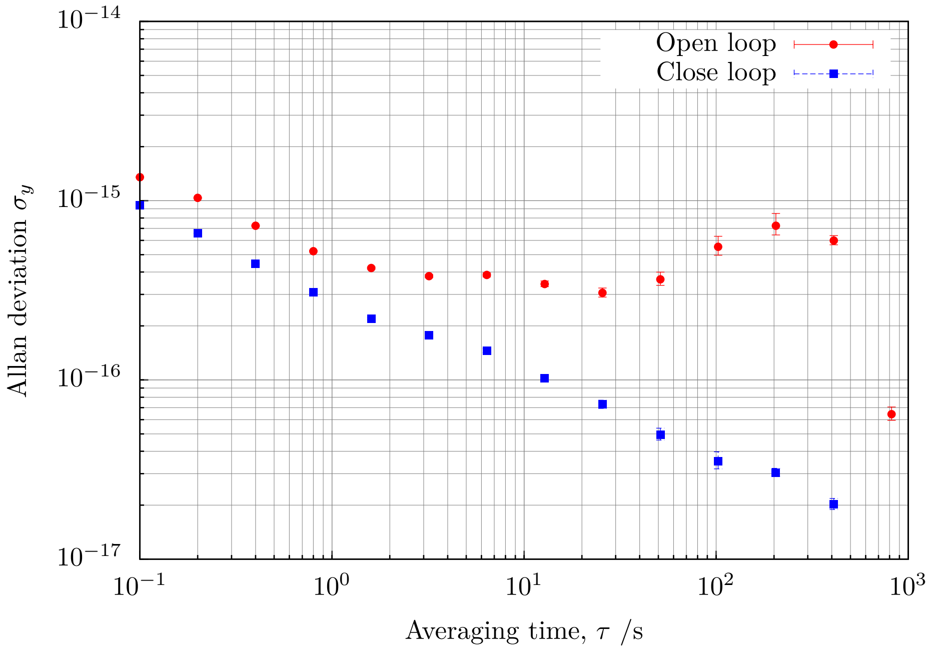

Figure 5.29: Stability of 8 m fiber link with the noise cancellation (close loop) and without (open loop).

Comparing fig. 5.29 and fig. 5.14 we conclude that the noise introduced by the fiber is not limiting the performances of the clock laser. However, we have observed that the noise strongly depends on the fiber placement. For example fig. 5.30 shows the noise introduced by 14 m fiber when coiled on the table or placed along two tables across the lab. In the second case the noise is much higher. In the future may be necessary to implement the fiber link in the lab to comply to different fibers or if better stability are required.

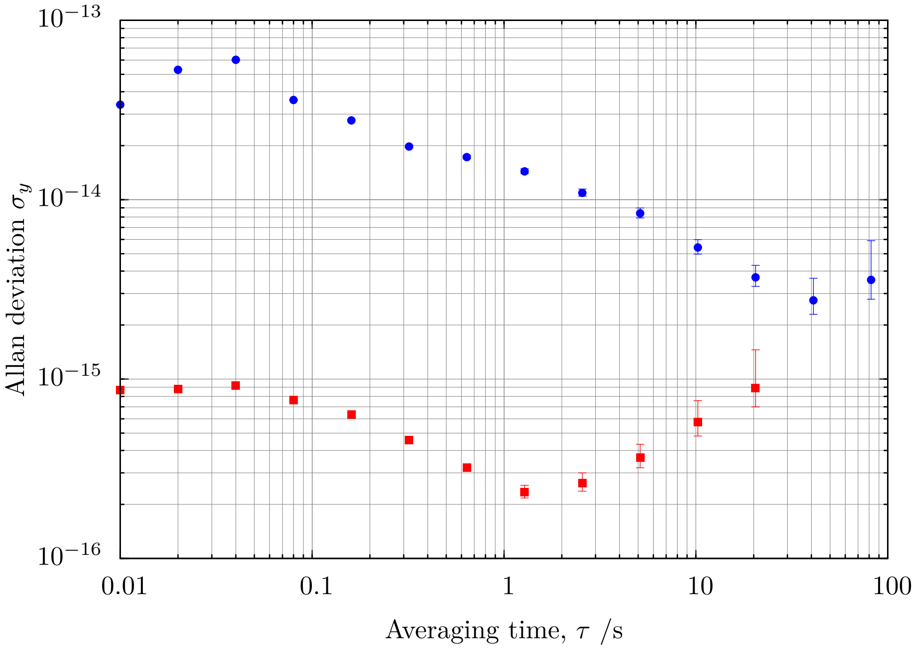

Figure 5.30: Stability of 14 m fiber link without noise cancellation for different placements of the same fiber.

6 Observation of the green MOT

6.1 Experimental setup

6.1.1 Vacuum chamber

The experimental setup is sketched in fig. 6.1 and shown in fig. 6.2. The ytterbium oven is an effusion oven directly connected to the vacuum chamber thermally controlled by an external heater. It has a multichannel nozzle made by 200 capillaries in Monel400 (internal diameter $D = 100\,\mu\text{m}$, length $L = 10\,\text{mm}$). The body of the oven is kept at a temperature of 360 °C while the nozzle is at 400 °C. This gradient prevents clogging of ytterbium in the capillaries.

The oven tip is 40 cm away from the trapping region center. Vacuum is kept by an ion pump with a pumping speed 40 L/s on the chamber side and an ion pump of 20 L/s on the oven. Differential vacuum is kept by a narrow tube. A titanium sublimation pump is used when needed on the chamber side. The vacuum pressure on he chamber side is about $1 \times 10^{-6}\,\text{Pa}$ ($1 \times 10^{-8}\,\text{mbar}$).

Midway from the oven and the trap there are 3 viewports that allows for transverse spectroscopy of the atomic beam.

The trapping structure is a custom spherical vacuum chamber with 16 viewports (on CF40 flanges). It has a diameter of 45 cm, from flange to flange. The window opposed to the oven is heated to 230 °C to prevent deposition of ytterbium.

A small pair of anti-Helmholtz coils are placed under vacuum to provide the magnetic field gradient of the MOT. The distance between the coils is $2D = 2\,\text{cm}$, the radius of the coils $R = 2.8\,\text{cm}$, and there are $N = 32$ turns. The magnetic field gradient for the MOT is obtained with a current between 3 A to 4 A.

A thin metal wire is placed 2.5 cm away from the MOT, on the atomic beam path, to avoid collisions from the atoms in the MOT and the beam. Loading of the MOT is done from the vapor of atoms scattering on the wire.

6.1.2 399 nm laser

The optical setup is summarized in fig. 6.3.

The 399 nm laser from duplication in the PPKTP crystal (section 4.1) is delivered to the chamber for the MOT (trapping beams), along the atomic beam for slowing (slower beam), and to the atomic beam for frequency locking (fig. 6.1). It is split using polarizing beamsplitter cubes and shifted by AOMs.

About 5 mW are used for spectroscopy on the atomic beam and frequency locking. This beam is sent perpendicular to the atomic beam and retro-reflected while the fluorescence

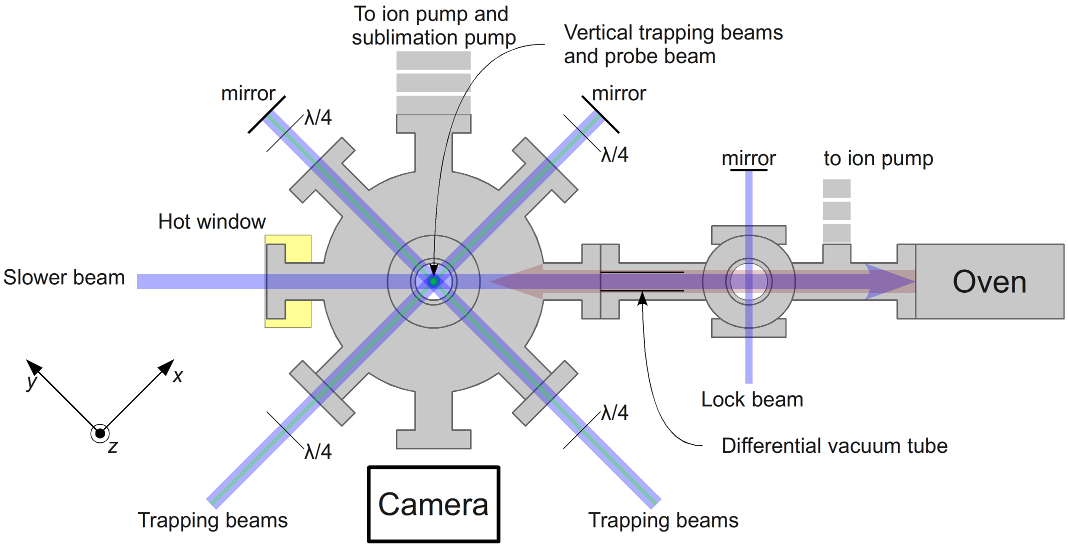

Figure 6.1: Scheme of the experimental setup.

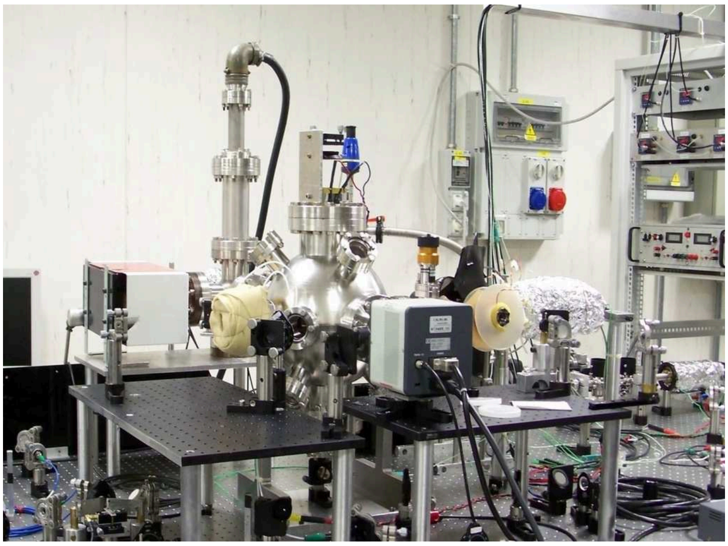

Figure 6.2: Picture of experimental setup.

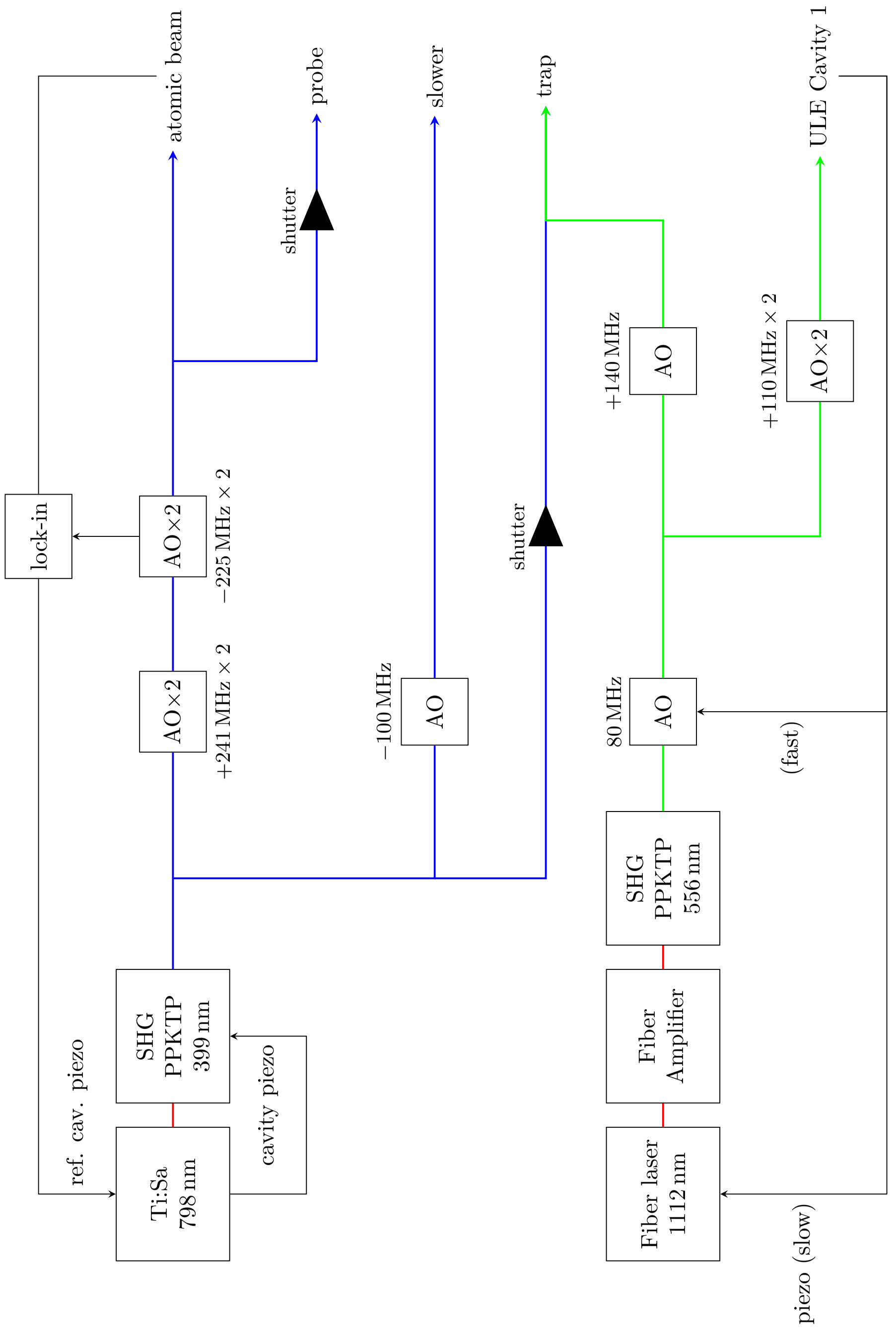

Figure 6.3: Summary of the optical setup for the blue and green MOTs. AO, acousto-optic modulator. AO×2, double pass acousto-optic modulator.

is monitored by a photodiode. The fluorescence signal is used to frequency lock the laser with the first harmonic technique using a lock-in amplifier [138]. The loop is closed acting on the reference cavity of the MBR laser, duplicated to 399 nm (see section 4.2).

Six laser beams are used for cooling and trapping in MOT. The radiation from the blue laser is divided in two horizontal beams and one vertical beam and all of them are retro-reflected. Each beam is about 5 mW and usually the vertical beam is slightly weaker than the horizontal ones. The diameter of the trapping beam at $1/e^2$ is about 2.7 mm measured near the vacuum chamber. Six $\lambda/4$ waveplates are used to control the polarization. These are dichroic $\lambda/4$ waveplates for both 399 nm and 556 nm wavelengths. The number of atom trapped is maximized when the trapping beams are detuned 32 MHz towards the red respect to the locking beam.

A seventh blue beam is sent counter-propagating to the atomic beam for additional slowing of the atoms. This slower beam has a fixed detuning from the resonance of 110 MHz toward the red. It has a typical power from 1 mW to 5 mW, as we shunt the blue power from the trapping beam to the slower beam to maximize the number of atoms trapped. The number of atoms trapped increases by $\simeq 10$ when using the slower beam.

A probe beam of ~ 1 mW is spilled from the locking beam and thus is in resonance with the atoms. It is superimposed to the vertical trapping beam. We can turn it on or off with a mechanical shutter.

6.1.3 556 nm laser

The green 556 nm laser is superimposed on the blue trapping beams using a dichroic mirror. Up to 3.4 mW of light are sent to the trap using a single-mode optical fiber. Steering of the green trapping beam can be done using two mirrors before superimposition with the blue laser. After that the green laser shares the same optical path, splitting, wave plates and retro-reflections of the blue laser.

The frequency of the laser is locked to an ultra-stable cavity using the Pound-Drever-Hall technique. The same setup used for locking the yellow laser is used with the green laser (see chapter 5). The frequency control is implemented using an AOM and the piezo actuator of the 1112 nm fiber laser.

To trap the atoms in the green MOT it is necessary to bridge the frequency difference between one of the resonance of the cavity and the frequency of the 556 nm transition of ytterbium. Since the cavity has a free spectral range of 1.5 GHz the shift could be up to 750 MHz and one or more AOMs are needed. We estimated the shifts between our two cavities and the different isotopes of ytterbium sending the green laser to the atomic beam (in place of the blue locking) and to the cavities.

With the AOMs available in the lab we were able to shift the frequency of the green laser locked to cavity 1 to the resonance of ^{172}Yb (fig. 6.4). No other combinations were tested.

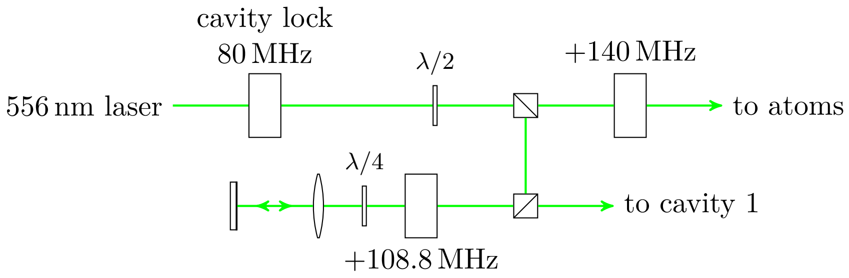

Figure 6.4: Setup for the green laser. The stated shifts of the AOMs are for the MOT with ^{172}Yb.

6.1.4 Timing and acquisition

Fluorescence signals and imaging of the MOT were performed using an electron multiply CCD camera Hamamatsu C9100-02. Its CCD has an effective area of 8.0 mm × 8.0 mm with 1000 × 1000 pixels and it is cooled to −50 °C. It has a quantum efficiency of 40 % at 400 nm and of 65 % between 550 nm to 700 nm. Data from the camera were acquired using Hamamatsu software (HCImage Live).

A blue filter (Thorlabs FB400-10) can be placed in front of the camera to record only the 399 nm radiation. The filter is centered at 400(2) nm, has a bandwidth of 10(2) nm, has a peak transmission of 41 % at 399 nm, and an attenuation of 39 dB at 556 nm.

Running of the experiment requires precision timing between the shutting of the lasers beams and the camera acquisition. Trigger signals were generated by a National Instrument board (NI-PCI 6221). Triggers are used for the mechanical shutter on the blue MOT beams, the mechanical shutter on the probe beam, the AOM on the slower beam and the camera shutter. The same board is able to generate an analog signals that drive the magnetic field gradient. The board is programmed in Visual Basic.

6.2 The blue MOT

Details of the blue 399 nm MOT has been reported in [139]. Four bosonic isotopes (^{170}Yb, ^{172}Yb, ^{174}Yb, ^{176}Yb) has been trapped and cooled to $T = 5(1)$ mK. Only one fermionic isotope (^{171}Yb) has been trapped and cooled to a lower temperature $T = 2(1)$ mK, because of sub-Doppler cooling [68]. Signals from ^{168}Yb are too weak to work with because of the low isotopic abundance. Working with ^{173}Yb is complicated by the small isotopic shift respect to ^{172}Yb.

The number of atoms trapped can be estimated from the fluorescence signal detected by the camera. Knowing the number of photons detected by the camera, we can compute the number of photons emitted by the atoms on the solid angle. The number of photons scattered by atoms is proportional to the number of atoms by a factor that includes laser beams intensities and shifts from resonance. The uncertainty in this factor is high ($u_\mathrm{r} \simeq 50\,\%$), because we cannot measure the laser beams right where the atoms are.

We trapped up to approximately 5×10^5 atoms of ^{174}Yb, up to 1×10^5 atoms of ^{172}Yb, and up to 2×10^5 atoms of ^{176}Yb or ^{171}Yb.

6.3 Experiments with a blue probe

The first observation of the green MOT was obtained using the blue probe resonant with the atoms. This is a powerful technique able to detect faint fluorescence signals from few atoms. We used the following procedure. The green beams were aligned on the blue ones using the beams spots. The green laser was locked to the ultra-stable cavity. We switched alternatively the blue trapping beams on and off thus loading and releasing the atoms in the blue MOT. The green trapping beams were left on, as was the magnetic field. The blue probe was pulsed 10 ms after the blue trapping beams were turned off. At the same time a picture of the 399 nm fluorescence was taken with the camera. After this short time no atoms from the blue MOT were usually detected. If the atoms were loaded from the blue in the green MOT the probe should sweep them away giving a 399 nm fluorescence signal.

We proceeded to sweep the frequency of the AOM working on the 556 nm trapping beams while monitoring the signal from the camera. At some point we got a signal similar to the one in fig. 6.5. In this false color image light blue is the dark background while the green rectangle highlights the signal from the vertical probe. The green MOT of ^{172}Yb was found to have a shift of -77.6 MHz respect to one resonance of ULE cavity 1.

6.4 Release and recapture

An approach similar to the probe one but that allows for quantitative measures is the “release and recapture” procedure [94]. The blue trapping beams were still switched on and off but we did not use the probe beam. We observed directly the 399 nm fluorescence signal from the trapping beams, as for example in fig. 6.6. When the green beams were off we observed the usual loading curve of the blue MOT. With the green beams on we observed a certain number of atoms in the blue MOT right from the start.

We took picture with the camera just before shutting down the blue trapping beams and just after turning them back on. The ratio between the two signals is a measurement of the fraction of atoms transferred in the second stage green MOT. We repeated this measurement for different values of the dark time without the blue beams. Figure 6.7 shows an example. Each data point is the mean of the ratio between 20 frames and uncertainty is given by the standard deviation of the mean. We fitted the data with a simple exponential and we measured a fraction transfer of 40.5(2) % for zero dark time and a lifetime of the green MOT of $\tau = 1.25(6)$ s.

6.5 Experiments with the green fluorescence

As a last test we set the camera to record the green 556 nm fluorescence signal directly from the atoms trapped in the green MOT instead of relying on blue beams. Fig-

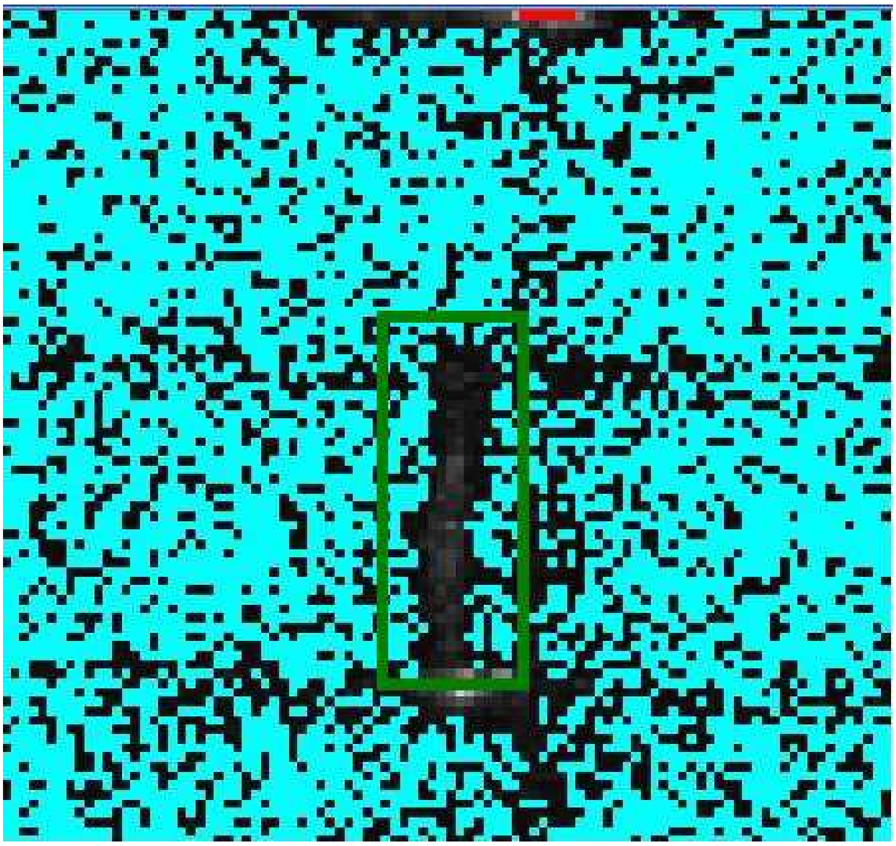

Figure 6.5: False color image taken with the camera of the blue probe on the green MOT. The signal highlighted by the green rectangle is blue light scattered by the atoms trapped in the green MOT that stands out respect to the dark background (light blue in the picture). Picture is roughly 5 cm × 5 cm.

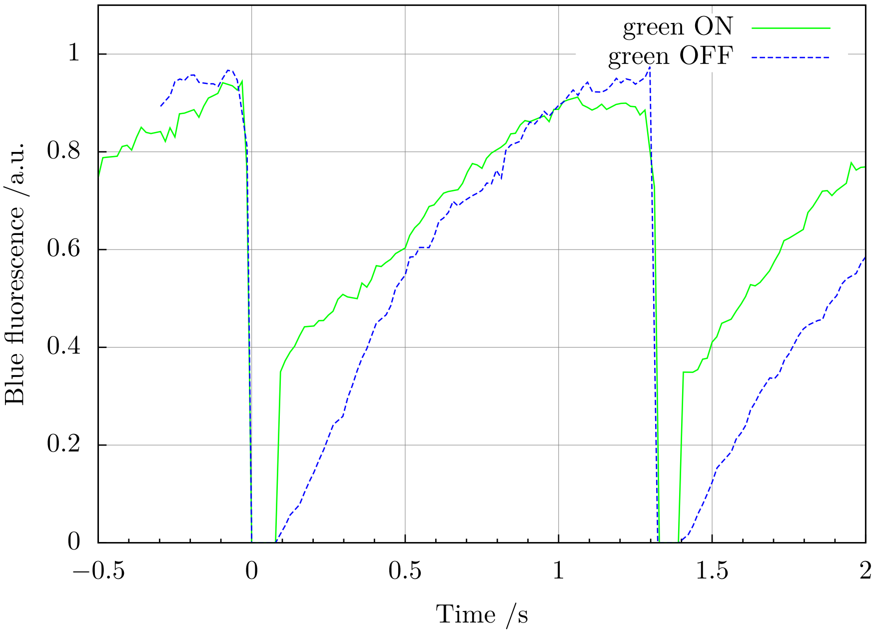

Figure 6.6: Release and recapture experiment.

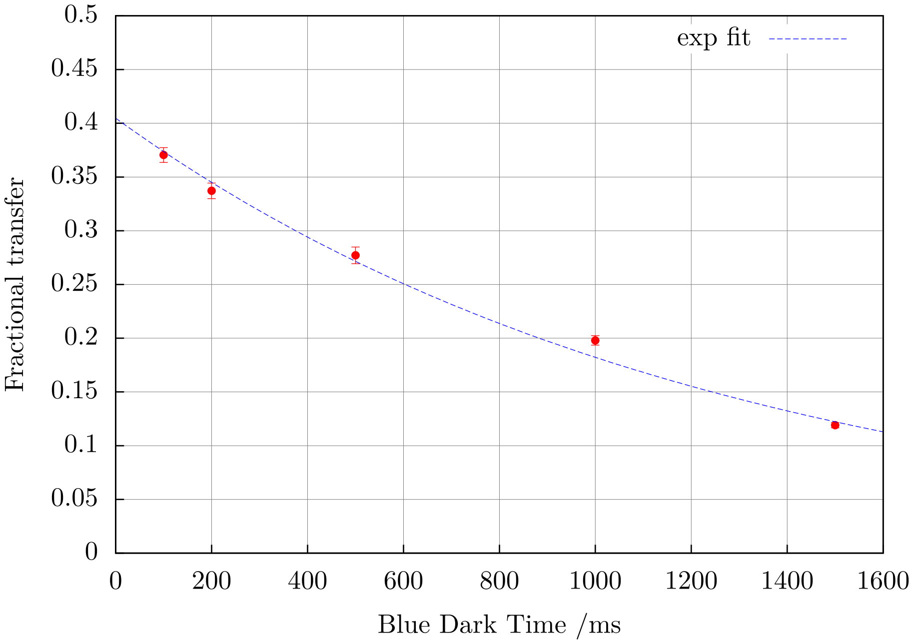

Figure 6.7: Decay of the green MOT measured by release and recapture.

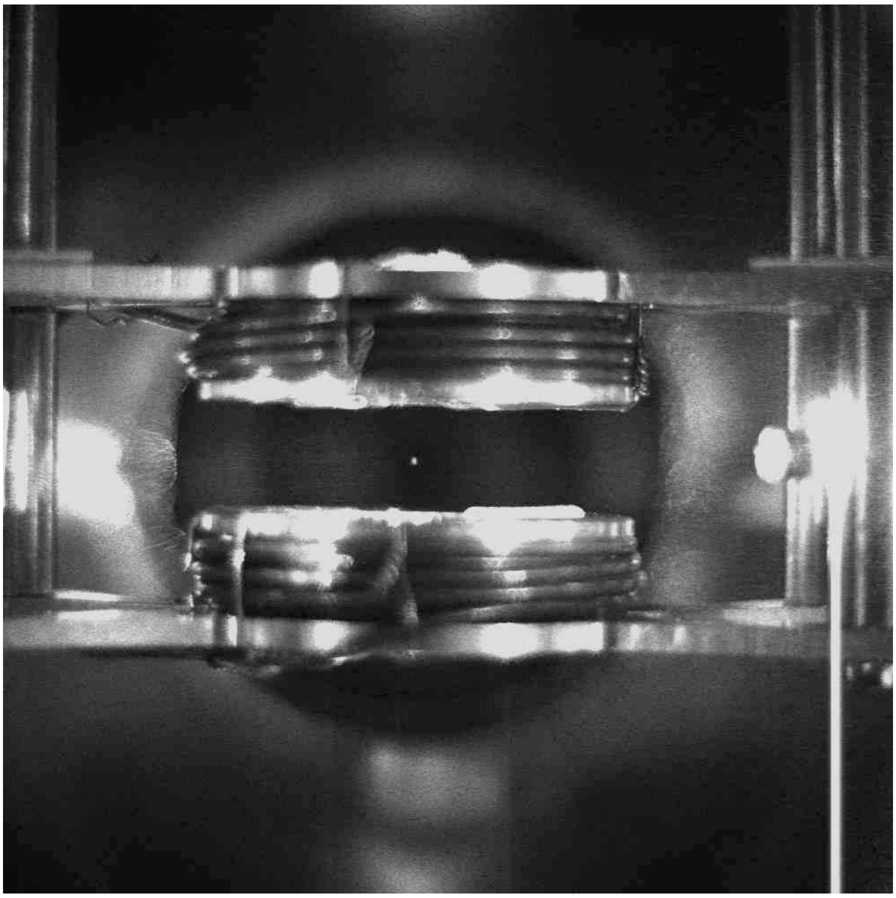

Figure 6.8: The green MOT as seen observing the 556 nm fluorescence. For reference the distance between the anti-Helmholtz coils is about 2 cm.

ure 6.8 shows a picture of the 556 nm fluorescence from the green MOT between the anti-Helmholtz coils. The green MOT is considerably smaller that the blue one when observed this way.

We measured the green MOT lifetime using the green fluorescence signal. As previously explained, we loaded the blue MOT with the 556 nm beams on. We shut the blue beams and after a prescribed delay we triggered the camera. No filter was placed in front of the camera that recorded the green fluorescence. Results are shown in fig. 6.9 for two sets of data and with a total power of the 556 nm trapping beams of 3.4 mW. We measured the lifetime of the trap $\tau = 0.8(2)$ s a result similar to the one obtained with the blue probe. The same figure show the decay of the green fluorescence when we reduced the green power to 1.4 mW. In this case $\tau = 0.9(2)$ s so no significant dependence of the lifetime on green power was observed.

The frequency of the 556 nm trapping beams can be changed to maximize the green fluorescence from the MOT or the fraction of atoms transferred in a release and recapture experiment. The optimal frequency for the two case is not the same and maximization of

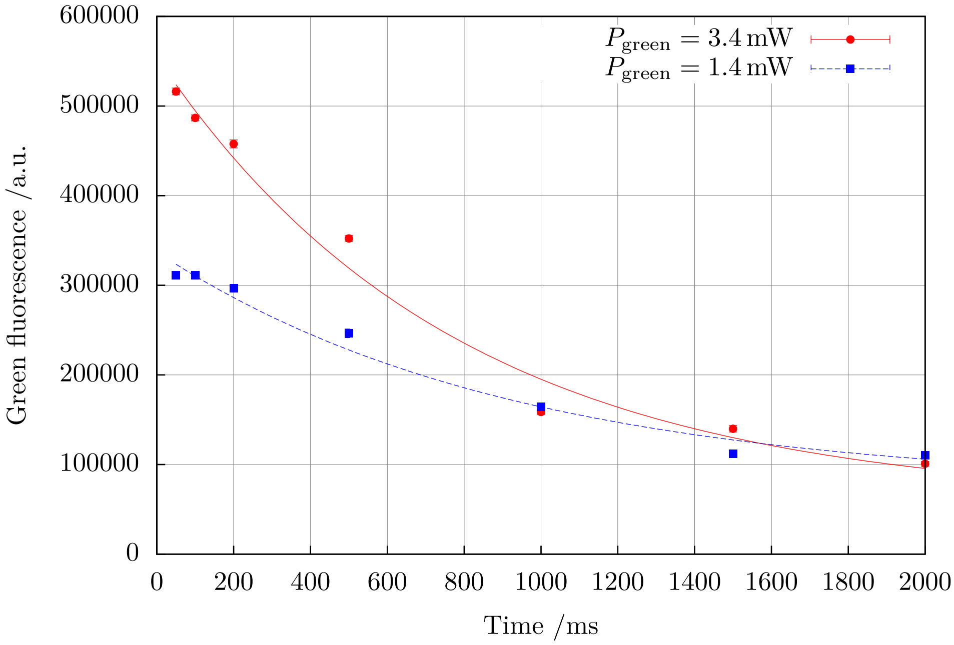

Figure 6.9: Decay of the green MOT measured with the green fluorescence.

the green fluorescence happens with the frequency shifted towards the blue by 6.0 MHz respect to the maximum transfer from the blue MOT. This shift in the green laser frequency is larger than the linewidth of the transition (182 kHz), as has been reported before [87].

7 Design of a new setup

Last months of 2012 were devoted to the design of an upgraded experimental setup to overcome some of the limitations of the current one. The new design comprehends a new vacuum chamber, a new atomic source, and a new pair of anti-Helmholtz coils to be externally mounted to the vacuum chamber.

In this chapter I will report the calculations and simulations that are at the base of the upgrade.

Several improvements are expected from the upgraded setup. Some of these also exploits the extra power at 399 nm available from the LBO crystal (section 4.2) that we have not yet tested on ytterbium atoms. The upgraded setup should

- trap a large number of atoms and reduce MOT loading time thanks to wider trapping beams and a higher-flux atomic source;
- have a lower vacuum pressure improving the lifetime in the green trap and being suitable for trapping in lattice;
- have a wide optical access on the atoms.

7.1 Vacuum system

Figure 7.1 shows a scheme of the new design and of some of its features. The core of the design is a custom aluminum chamber for the trapping region with 6 lateral viewports (diameter 40 mm) and two larger horizontal viewports (diameter 70 mm). The other components are standard stainless steel fittings.

A differential-vacuum tube divides the oven side of the structure from the clean trapping region. The design goals for the vacuum pressure in our system are 1×10^{-6} Pa (1×10^{-8} mbar) on the oven side and a few parts in 10^{-8} Pa (few parts in 10^{-10} mbar) on the clean side.

The atomic source for the new setup is an atomic oven designed at Physikalisch-Technische Bundesanstalt (PTB) and LENS [140, 141]. The oven is housed in a custom cross with a longer arm to fit the length of the oven. The oven is made by a stainless steel reservoir and heating elements and it works under vacuum (fig. 7.2). It is surrounded by a aluminum radiation shield and can be heated up to 500 °C. At the exit of the reservoir ~ 37 stainless steel capillaries are used to collimate the atomic beam.

Between the oven tip and the differential-vacuum tube is placed a shutter that can turn off the atomic beam. The shutter is based on a ferrofluid rotary feedthrough. The feedthrough has a shaft that can rotate at high speed and it is UHV compatible thanks to a series of seals made by ferromagnetic fluid.

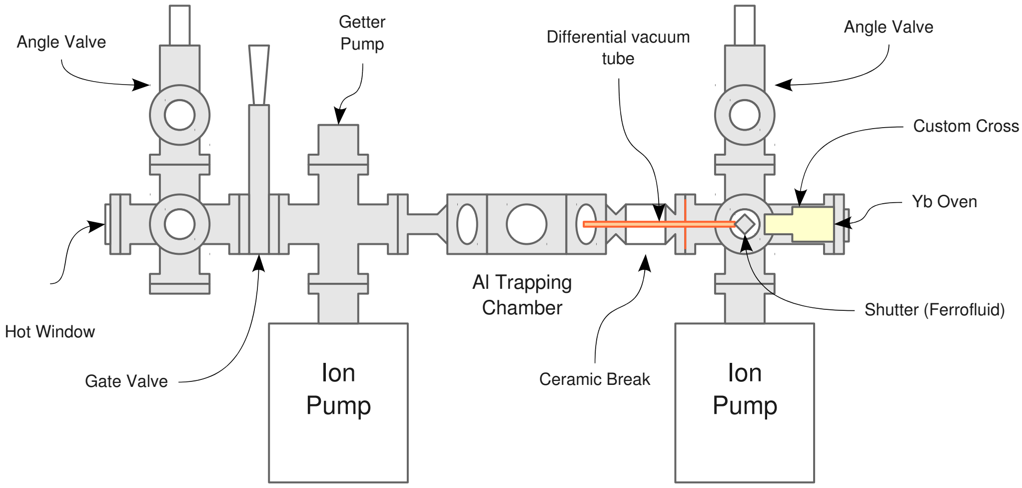

Figure 7.1: Scheme of the new vacuum chamber.

Figure 7.2: Picture of the atomic oven during assembling.

Figure 7.3: Picture of the custom aluminum chamber for the trapping region.

The aluminum chamber is shown in fig. 7.3. We opted for indium sealing on the aluminum chamber instead of Conflat flanged viewports or Kasevich-style sealing [142]. Indium sealing is a solution already used in the strontium optical clock at LNE-Syrte in Paris [143]. Viewports are sealed simply using an indium wire that is a soft material and allows for UHV compatible sealing. Indium is used also between a flat-flat mating achieved using a K flange transition for sealing together aluminum and stainless steel. This solution allows for a wide area of the viewports to be available for optical access but requires only a small retaining force reducing the induced birefringence in the glass. For this reason it is preferred to Kasevich-style sealing.

Using indium-sealing, all the surface of the viewports can be coated because no flange shadows the deposition of the coating. The anti-reflection coating of the viewports is made by ATFilms for all the wavelengths of interest (see fig. 7.4). The reflectivity for the blue 399 nm is $R = 0.08\,\%$ and for the green 556 nm $R = 0.1\,\%$. For the clock laser at 578 nm the reflectivity is $R = 0.03\,\%$. The anti-reflection coating is especially important for the magic wavelength 759 nm ($R = 0.05\,\%$), because we are going to use an enhanced cavity for the lattice, external to the chamber.

Facing the oven tip, on the clean side, a window is used for a slower laser beam, counterpropagating the atomic beam. The windows is flanged and uncoated because it should be heated at 230 °C to prevent deposition of ytterbium. If deposition still occurs the windows can be easily replaced closing the main clean chamber with a gate valve.

We can put another rotary shutter in front of the hot window. Closing the shutter avoids a direct line of sight between the hot window and the cold atoms and thus can simplify the evaluation of the blackbody radiation shift on the clock transition.

Two angle valves, on both the clean side and oven side of the structure, are used for connection to turbo-molecular pumps, to be used in the initial stage of vacuum pumping.

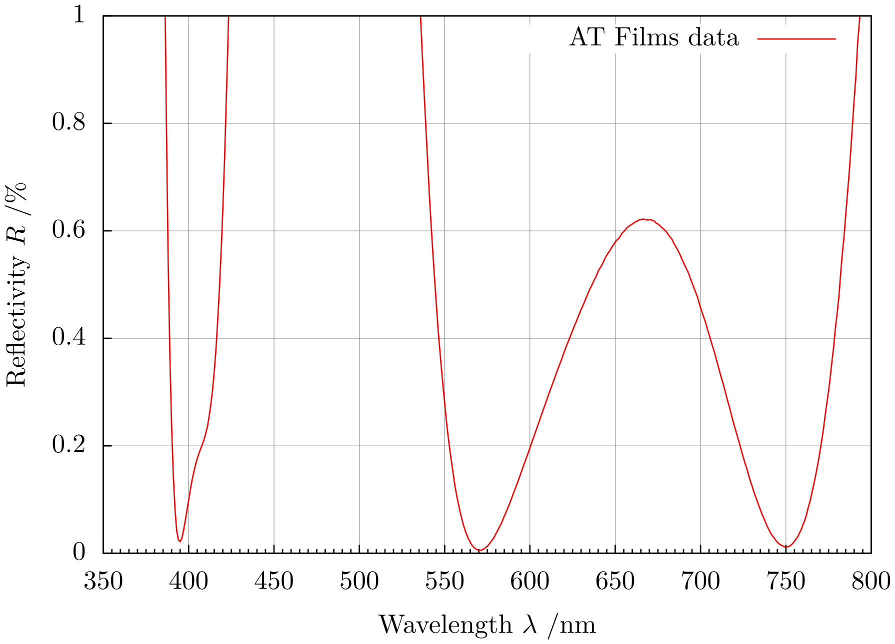

Figure 7.4: Reflectivity of one surface of the viewports for the trapping chamber, coated for 399 nm, 556 nm-578 nm and 759 nm. Courtesy of ATFilms.

On both sides there is an ion pump (Agilent VacIon 40) of nominally 40 L/s speed. On the clean side there is also a non-evaporable getter pump (Saes D50). The getter pump is a passive pump for hydrogen (H_2) but also pumps water and carbon oxide. The getter pumping speed for hydrogen is 50 L/s.

7.1.1 Differential vacuum

A differential-vacuum tube is necessary to establish a pressure ratio between the oven side, where the hot oven limits the ultimate pressure, and the trapping side that should be as clean as possible. The design of the differential-vacuum tube is critical for achieving the necessary ultimate vacuum pressure in the structure while allowing the flux of ytterbium from the the atomic beam.

The gas conductance for an aperture of area A at low pressure (molecular flow) is given by

$$C_{\mathrm{a}} = \frac{1}{4} A v_{\mathrm{av}}, \tag{7.1}$$

where $v_{\mathrm{av}} = \sqrt{8k_{\mathrm{B}}T/(\pi m)}$ is the average velocity of the molecules in the Maxwell-Boltzmann distribution with k_{B} the Boltzmann constant, T the temperature, and m the mass. For a duct of perimeter H, area A, and length L the conductance is reduced respect to a thin aperture by the probability of transmission of a molecule (Clausing factor). The conductance of the tube is then [144]

$$C = C_\mathrm{a} \left(1 + \frac{3}{16}\frac{LH}{A}\right)^{-1} . \tag{7.2}$$

For a circular tube of radius R and length L this is

$$C = \frac{\pi}{4} R^2 v_\mathrm{av} \left(1 + \frac{3}{8}\frac{L}{R}\right)^{-1} . \tag{7.3}$$

The differential-vacuum tube has $R = 2.5\,\mathrm{mm}$ and $L = 120\,\mathrm{mm}$. Its conductance can be calculated using eq. (7.3) but it depends on the molecular mass of the gas involved. For example we can use nitrogen, i.e., air, or hydrogen that is the most likely contaminant in a stainless steel vacuum chamber. For nitrogen (N_2) at room temperature the conductance of the differential-vacuum tube is then $C_{\mathrm{N}_2} = 0.12\,\mathrm{L/s}$. For hydrogen ($H_2$) the conductance is $C_{\mathrm{H}_2} = 0.46\,\mathrm{L/s}$ These values should be compared to the pumps speed on the clean side. (In a simple electrical circuit equivalent a vacuum pump is a resistance towards ground.) For nitrogen the pumping speed is simply the ion pump speed 34 L/s (nominally is 40 L/s). For hydrogen the pumping speed of a StarCell ion pump is 2.2 times that of nitrogen [145] or 75 L/s. We should add the pumping speed of the getter 50 L/s. With these numbers the pressure ratio than can be established across the differential-vacuum tube is 280 for nitrogen and 270 for hydrogen. This means that a vacuum pressure of 10^{-8} Pa (10^{-10} mbar) in the clean side of the chamber is compatible with a pressure of 10^{-6} Pa (10^{-8} mbar) on the oven side.

7.2 Atomic oven

The oven tip is a multichannel array made by 37 stainless steel capillaries with internal diameter $D = 280\,\mu\mathrm{m}$ and a length $L = 8\,\mathrm{mm}$ (see fig. 7.5). From the picture is clear that a good contribution to the total flux from the tip comes from the interstices between the capillaries. For the tip in fig. 7.5 there are 38 interstices, of which at least 17 of dimension comparable to the tube. For calculation purpose I will assume 50 capillaries with diameter $D = 280\,\mu\mathrm{m}$.

The divergence of the atomic beam from this capillaries should be taken in account since the distance between the trapping region ans the oven tip influence the flux of atoms that intersect the MOT beams. The normalized distribution function (dimensionless) of the flow of particles from a tube with given internal diameter D and length l is given in [146]:

$$J(\theta) = \xi_0 \cos\theta + \frac{2}{\pi}\cos\theta \left[(1-\xi_0)R(p) + \frac{2}{3}(\xi_1 - \xi_0)\frac{1-(1-p^2)^{3/2}}{p}\right] \qquad \text{for} \tan\theta \le \gamma \tag{7.4}$$

$$J(\theta) = \xi_0 \cos\theta + \frac{4\gamma}{3\pi}(\xi_1 - \xi_0)\frac{\cos^2\theta}{\sin\theta} \qquad \text{for} \tan\theta \ge \gamma, \tag{7.5}$$

Figure 7.5: Details of the multichannel array. From this picture we can count 37 channels and 38 interstices.

where θ is the divergence angle, $\gamma = D/L$ and

$$R(p) = \arccos(p) - p(1-p^2)^{1/2} \tag{7.6}$$

$$p = \frac{\tan\theta}{\gamma}. \tag{7.7}$$

In the formula ξ_0 and ξ_1 are the normalized wall collision rate at the exit and at the entrance of the tube (these are once again Clausing factors [147]). For long tubes

$$\xi_0 = \frac{3}{2}\gamma \text{ and } \xi_1 = 1. \tag{7.8}$$

Figure 7.6 reports the plot for the function $J(\theta)$ which is usually piqued at $\theta = 0$ where it has a cuspid. This formula is valid in the limit that no collisions between atoms occur in the tube or for a mean free path much larger than the length of the tube $\lambda_{\mathrm{mfp}} \gg L$ (clean channel).

Integrating $J(\theta)$ on the solid angle gives the total flux of atoms from the tube according to

$$Q = \nu_{\mathrm{r}} A K = \nu_{\mathrm{r}} A \int_0^{\pi/2} 2J(\theta)\sin\theta \mathrm{d}\theta, \tag{7.9}$$

where ν_{r} is the rate of atoms entering the tube per unit area, A the area of the tube, and K is the transmission probability. The rate of atoms is given by $\nu_{\mathrm{r}} = 1/4 n v_{\mathrm{av}}$, where n is the numerical density and v_{av} is the average speed in the reservoir. The probability K is equal to 1 for a thin aperture. Note that $J(\theta)$ is normalized so that $J(0) = 1$. The tube reduces the divergence of the beam but leaves unchanged the flux of atoms along the forward direction [148]. This increase the lifetime of the oven while leaving unchanged the flux of atoms reaching the MOT region.

Because of the divergence of the atomic beam most of the atoms leaving the oven will be lost before reaching the MOT region. We can use eq. (7.9) to calculate the fraction of atoms from the beam that intersect a circular target of radius B at a certain distance

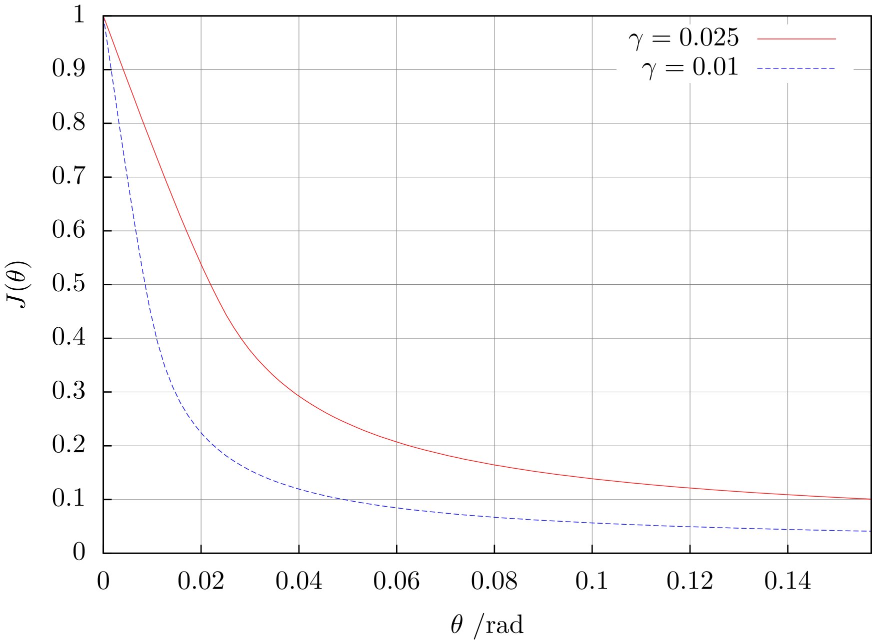

Figure 7.6: Example of the atomic beam divergence out of a capillary.

R along the axis. This can be simply done integrating J over the solid angle underlying the target region.

$$f = \frac{1}{Z}\int_0^{\theta_B} 2J(\theta)\sin\theta \mathrm{d}\theta, \text{ with } \theta_B = \arctan(B/R). \tag{7.10}$$

The factor $1/Z$ normalizes the result to 1. I performed a more complicated and time-consuming Monte Carlo simulation taking in account the finite dimensions of the oven tip but found the results consistent with the simpler approach of eq. (7.10). The results are shown in fig. 7.7.

With the parameter of the new oven, $K = 0.07$. The vapor pressure of ytterbium is 1×10^{-1} Pa assuming a temperature of the oven of 673 K (fig. 3.1). Using the ideal gas law we obtain a numerical density $n = 1 \times 10^{19}\,\mathrm{m}^{-3}$. The average velocity at this temperature is $v_{\mathrm{av}} = \sqrt{8k_{\mathrm{B}}T/(\pi m)} = 290\,\mathrm{m/s}$. The total area of 50 capillaries with a diameter $D = 280\,\mu\mathrm{m}$ is $A = 3.1\,\mathrm{mm}^2$. The total flux out of the oven is thus predicted to be

$$Q = \frac{1}{4} n v_{\mathrm{av}} A K = 1.5 \times 10^{14}\,\mathrm{s}^{-1}. \tag{7.11}$$

Between the oven and the MOT is the differential-vacuum tube (radius $B = 2.5\,\mathrm{mm}$). Its far end is at $R = 15\,\mathrm{cm}$ from the oven tip. The fraction of atoms from the beam transmitted by the tube is calculated using eq. (7.10) $f_{\mathrm{dvt}} = 3 \times 10^{-3}$. We can compute the fraction of atoms intersecting the trapping beam region of the MOT at a distance $R = 20\,\mathrm{cm}$ ignoring the differential vacuum tube. We assume a radius for the trapping

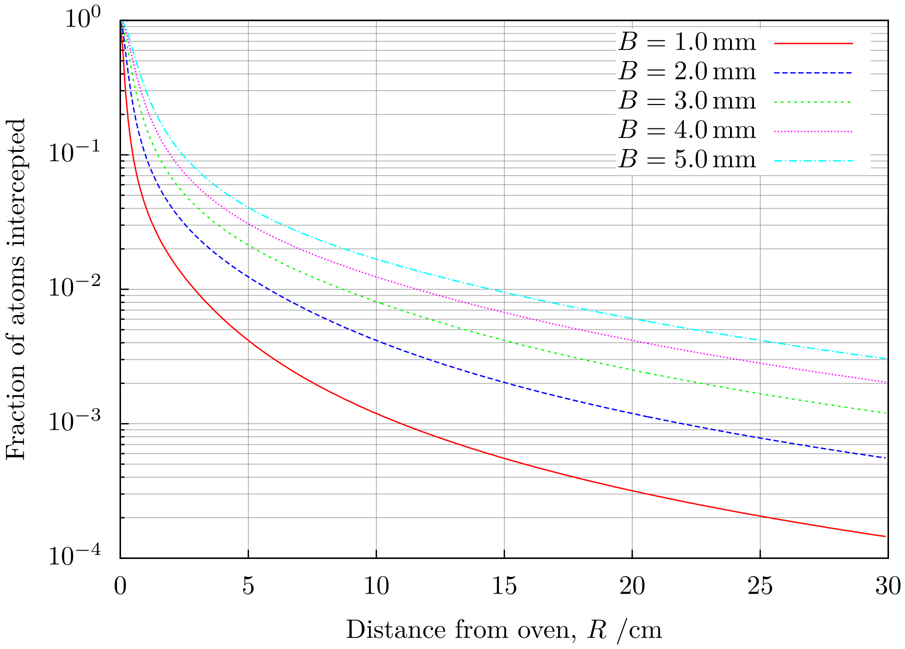

Figure 7.7: Fraction of atoms from the oven beam intercepted by a circular aperture of radius B as a function of the distance from the oven.

region of $B = 5$ mm; this is a reasonable assumption with wide 399 nm beams of 1 cm. The fraction of atoms intersected by the MOT is then $f_{\text{MOT}} = 6 \times 10^{-3}$. We should be limited by the differential vacuum tube aperture (slightly). We thus predict a flux of atoms $4 \times 10^{11}\,\text{s}^{-1}$ in the trapping region. Only the slowest atoms will be actually captured here as I am going to discuss later (see section 7.4).

7.3 MOT coils design

One important problem in the design of the system is the design of the pair of coils needed for the MOT. Smaller coils require less current and less power but they limit the optical access to the atoms. Putting the coils inside the chamber allows for compact coils but compromises the vacuum level in the chamber and the black body radiation shift evaluation. Our coils are placed around the big viewports of the chamber and housed in notch in the aluminum structure (see fig. 7.3).

7.3.1 Magnetic Field for circular coil pairs

Consider two circular loop coils of radius R perpendicular to the z axis and displaced at $z = \pm D$ (distance between the coils $d = 2D$). Then the magnetic field $\boldsymbol{B}$ generated by a current I in the loops in anti-Helmholtz configuration, in cylindrical coordinates (ρ,

ϕ, z), is $B_\phi = 0$ and near the origin [149]

$$B_z \simeq 3\mu_0 I \frac{DR^2}{(D^2+R^2)^{5/2}} z, \tag{7.12}$$

$$B_\rho \simeq \frac{3}{2}\mu_0 I \frac{DR^2}{(D^2+R^2)^{5/2}} \rho. \tag{7.13}$$

Note that the magnetic field gradient along the z axis is twice the gradient in the radial direction.

If we neglect the physical dimension of the loops we can write $I = NI_0$ where N is the number of turns and I_0 is the actual current in each coil. Fixing I_0 and the geometrical dimension R and D we can use eq. (7.12) we can compute the number of turns N we need to obtain a certain magnetic field gradient $A_z = \mathrm{d}B_z/\mathrm{d}z$. For example this is done on fig. 7.8 with $I_0 = 15\,\mathrm{A}$ and $A_z = 0.5\,\mathrm{T/m}$. Figure 7.8 shows the isoline in the R-D plane for the number of turns. The same plot shows in red the regions occupied by vertical and horizontal trapping laser beams of diameter $2w = 1\,\mathrm{cm}$ when considering diffraction ($d = 4.6w$ criterion gives intensity ripples $\simeq \pm 1\%$ [71]). We used fig. 7.8 in the initial design of the coils. For example it is clear that is better to grow the coils vertically rather than radially starting from $R = 49\,\mathrm{mm}$ and $D = 24\,\mathrm{mm}$.

The geometry of the problem is sketched in fig. 7.9 when we consider the physical dimension of the wire in the coils. We want to optimize the geometrical parameters D_0, R_0 and h, the number of coils N and the current I_0 keeping the gradient $A_z = 0.5\,\mathrm{T/m}$. I ran computer simulations written in Python to calculate the current in each coil, the power dissipated, and the voltage across each coil as a function of the number of coils. An example of such simulation is shown in fig. 7.10 corresponding to a new chamber. The parameter for the simulations were $R_0 = 49\,\mathrm{mm}$, $D_0 = 24\,\mathrm{mm}$ and $h = 21\,\mathrm{mm}$. We considered wire with an external diameter $\phi = 1.33\,\mathrm{mm}$ and a diameter of the copper conductor $\phi_{\mathrm{Cu}} = 1.25\,\mathrm{mm}$. I have assumed a resistivity for copper of $\rho_{\mathrm{Cu}} = 1.7 \times 10^{-8}\,\Omega\,\mathrm{m}$. The simulations predicts for $N = 130$

- a current of 11.6 A,
- a voltage across each of the two coils of 6.8 V,
- a power consumption of 80 W for each of the two coils and
- a thickness of the spool of wire < 1 cm.

The current and voltage values are well within the capabilities of the current supply (Kepco Bipolar Operational Power Supply BOP-20-20DL, voltage output from 0 V to 20 V and current output from 0 A to 20 A). The proportional constant between magnetic field gradient and current is $a = 0.043\,(\mathrm{T/m})/\mathrm{A}$. Water cooling of the coils with a chiller will be necessary to keep the vacuum chamber cool.

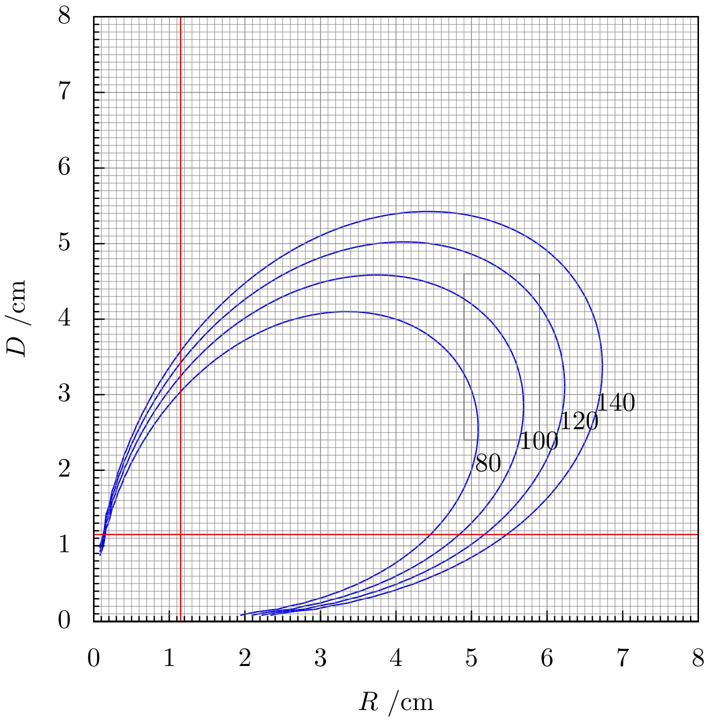

Figure 7.8: Constraints on the geometry of the coils: red, horizontal and vertical aperture that gives diffraction ripples $\simeq \pm 1\%$ for beam diameter $2w = 1\,\mathrm{cm}$; blue, contour line for the number of turns for $I_0 = 15\,\mathrm{A}$ and $A_z = 0.5\,\mathrm{T/m}$. Black rectangle is the final position of the coils.

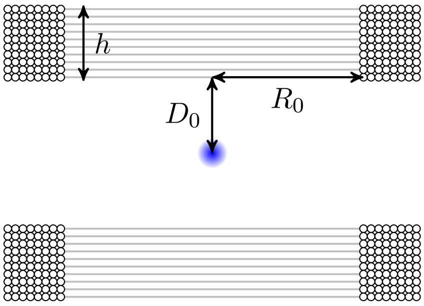

Figure 7.9: Geometrical parameters considered in the simulations of the coils.

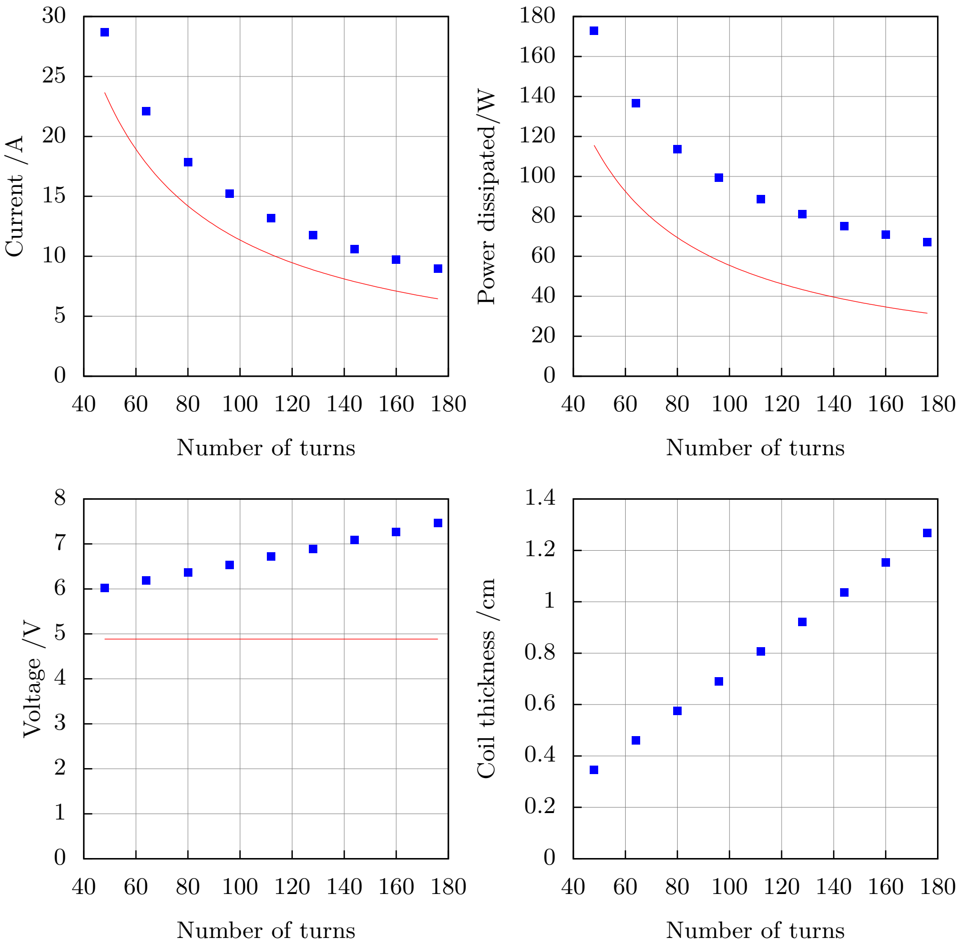

Figure 7.10: Numerical simulations for the current, power dissipated, voltage across each spool and thickness of the spool in function of the total number of coils (for one spool). This is the final setup with required magnetic field gradient $A_z = 0.5\,\mathrm{T/m}$, $R_0 = 49\,\mathrm{mm}$, $D_0 = 24\,\mathrm{mm}$, $h = 21\,\mathrm{mm}$ and $\phi = 1.33\,\mathrm{mm}$. For comparison the red lines shows the calculation ignoring the physical dimensions of the wires.

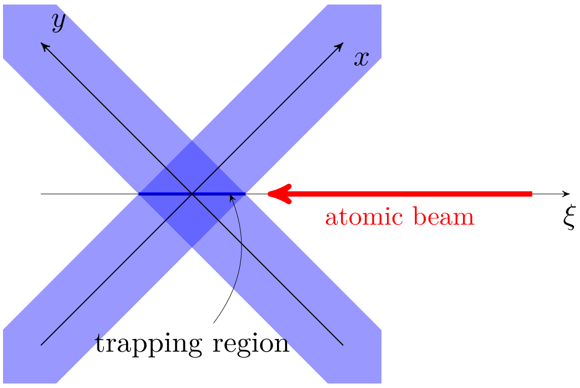

Figure 7.11: Simple, mostly 1D simulation of a MOT.

7.4 MOT simulations

We would like to predict the number of atoms attainable in MOT, the capture velocity, and the possibility to slow the atomic beam with a counter-propagating laser in our new setup.

The basic tool for calculations is the formula for the force on a two-level atom from radiation pressure eq. (2.1). The treatment of three-dimensional MOT is complicated by the relative polarization of 6 orthogonal laser beams and it is in general unpractical. We considered a simple 1D model of a MOT but we take into account the geometry of our beams in the experiment (refer to fig. 7.11). Atoms are simply moving only on one axis (ξ), with zero parameter of impact from the center of the MOT. The atomic beam intersects two horizontal trapping beams at 45° in the directions x and y. No vertical beam is considered. This model is used only to scale properly the dimensions of the beams and their intensities doing the math only along ξ.

The force used in the simulation is then

$$F_{\pm} = \pm\sqrt{2}\frac{\hbar k\gamma}{2}\frac{I/I_s}{1+4I/I_s+(2\delta_{\pm}/\gamma)^2} \tag{7.14}$$

where I is the intensity of the single beam, γ is the linewidth of the atomic transition, I_s is the saturation intensity,

$$\delta_{\pm} = \delta \mp \frac{kv}{\sqrt{2}} \pm \frac{\mu' A\xi}{\hbar}, \tag{7.15}$$

with δ the detuning from the atomic resonance, and A the magnetic field gradient along ξ.

For the 399 nm trap $\gamma = 2\pi \times 29.1\,\mathrm{MHz}$, $I_\mathrm{s} = 60\,\mathrm{mW/cm^2}$, $\delta = -\gamma/2$ and $A = 0.225\,\mathrm{T/m}$.

In the simplest approach the beams can be modelled by top-hat beams [71]. The diameter of the top-hat beam is related to the effective beam radius w of a gaussian beam by

$$d_\mathrm{th} = \sqrt{2}w.$$

Inside this diameter the intensity is constant (equal to the peak intensity of the equivalent gaussian beam)

$$I_{\text{th}} = \frac{2P}{\pi w^2},$$

with P is the total power of the beam. With top-hat beams the trapping region along ξ is long $\sqrt{2}d_{\text{th}}$ (fig. 7.11) and no force is applied outside.

We can define the capture velocity v_{c} as the initial velocity of an atom that, under the action of the trapping lasers, is stopped at the edge of the trapping region. Simulations of the capture velocity as a function of beam diameter and intensity are shown in fig. 7.12.

At the cost of extra complexity we can considered collimated beams described by a gaussian intensity profile

$$I(r) = \frac{2P}{\pi w^2} \exp\left(-\frac{2r^2}{w^2}\right). \tag{7.16}$$

With gaussian beams there the trap does not have sharp boundaries but we still assume the trap dimension proportional to w. Figure 7.13 shows the simulations with gaussian beams. These simulations behaves better at low beam diameters (high intensity) where the top-hat approximation results in fictitiously high force on all the trap region. The two approximations are otherwise similar and predict that it is necessary to work with large beams (diameter of the order of 1 cm). Much smaller beams reduce the capture velocity because of the shorter path available for deceleration. Much larger beams, at constant power, reduce too much the intensity of the beams and thus the force on the atoms.

For a beam radius of $w = 5\,\text{mm}$ and a power of each beam of 10 mW we then predict a capture velocity of $v_{\text{c}} = 30\,\text{m/s}$.

7.4.1 Slower beam

The number of atoms trapped can be enhanced increasing the number with velocity lower than the capture velocity. The atomic beam from the oven can be slowed using a counter-propagating, detuned to the red, laser beam [65]. In the absence of a magnetic field the effect of the beam is limited because, once slowed down, atoms goes out of resonance and are decelerated only for a short portion of their path. For this purpose a Zeeman slower is usually used; a space dependent magnetic field is engineered so that the atoms are always kept on resonance while decelerating [140, 150]. In the setup at INRIM a Zeeman slower is not used for simplicity. The simply addition of a slower beam usually improves a factor of ten the number of trapped atoms [87, 139]. Moreover a Zeeman slower is usually 50 cm long while without it is possible to keep the setup shorter.

Simulation of the slower beam is a direct application of the formula for the force by radiation pressure eq. (2.1) I performed a simple 1D simulation with the laser beam at constant intensity. The force depends on the portion of the path because of the magnetic field produced by the MOT coils that should be taken into account. The expression for the magnetic field of a coil of current anywhere in the space can be found in [151]. For the configuration presented in the previous section we expect a maximum magnetic field

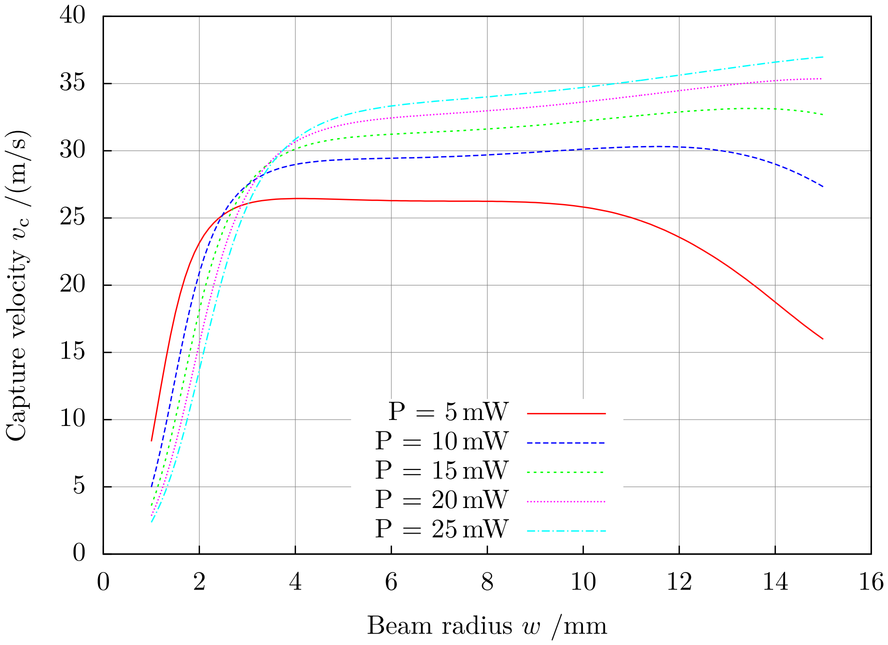

Figure 7.12: Numerical simulations of the capture velocity in the 399 nm MOT as a function of the beam radius w and the single-beam power P. Simulation using top-hat beams with $\delta = -\gamma/2$.

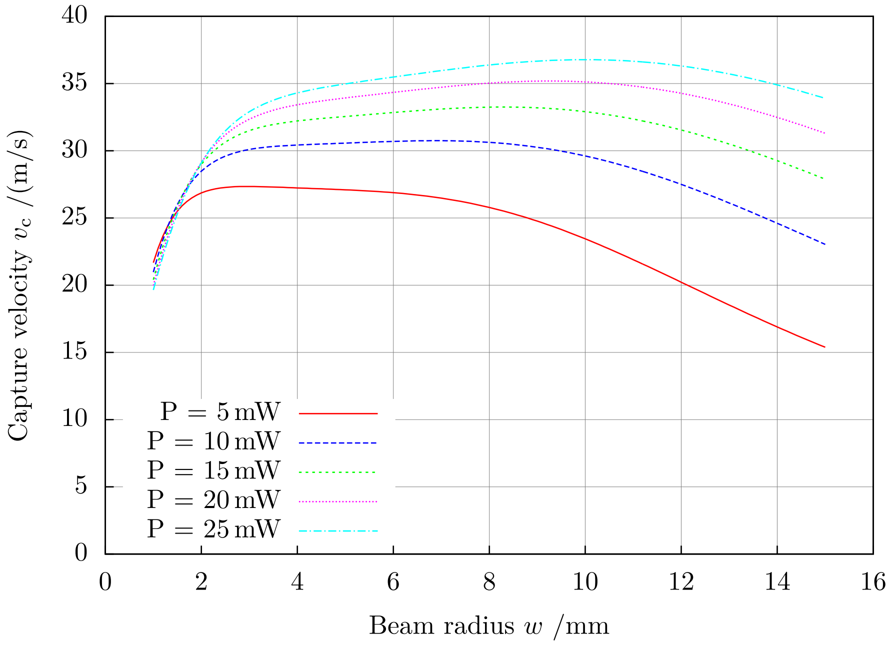

Figure 7.13: Numerical simulations of the capture velocity in the 399 nm MOT as a function of the beam radius w and the single-beam power P. Simulation using gaussian beams with $\delta = -\gamma/2$.

in the plane between the coils of 13 mT; this value is in good approximation the magnetic field gradient in the plane $A_r = 0.23\,\mathrm{T/m}$ times the mean radius of the coils 5.5 cm.

Two example of simulations are presented in fig. 7.14. The plots shows the trajectories in the phase space for atoms with different initial velocities 20 cm far away from the MOT center. The gray thick line shows the velocity at which the atoms are resonant with the light because of the magnetic field and thus is the locus of points in the phase space with the maximum deceleration. The top figure shows a simulation with $\delta = -2\pi \times 150\,\mathrm{MHz}$ and polarization σ^-. With this polarization the magnetic field from the coils pushes slower atoms out of resonance and the slower is effective only far away from the MOT center. There is not enough space to slow down faster atoms brought in resonance by magnetic field gradient of the MOT. This is a configuration similar to the one used on the current setup. In this configuration atoms with initial velocity $v_\mathrm{i} = 60\,\mathrm{m/s}$, usually not captured by the MOT, are brought to a velocity of $v_\mathrm{f} = 20\,\mathrm{m/s}$ that is below the capture velocity. The bottom figure shows a simulation with $\delta = -2\pi \times 330\,\mathrm{MHz}$, polarization σ^+. With this polarization the leaking magnetic field can be used to keep in resonance and slow down faster atoms. In practice, since our coils are large, we can exploit the leaking magnetic field of the MOT for Zeeman slowing without an actual Zeeman slower. Moreover the detuning in this configuration is larger and thus the slower beam should interfere less with the atoms captured in the MOT.

The simulations can be also used to predict the number of atoms slowed below the capture velocity. For this we can start from Maxwell-Boltzmann distribution in an atomic beam [11]

$$f_\mathrm{b}(v_z) = \frac{v_z^3}{2\tilde{v}^4} \exp\left(-\frac{v_z^2}{\tilde{v}^2}\right), \tag{7.17}$$

where

$$\tilde{v} = \sqrt{\frac{k_\mathrm{B}T}{M}}. \tag{7.18}$$

Numerical simulations are used to compute the final velocity v_f as a function of initial velocity v_i. The number of atoms is constant so the distribution of the final velocity can be calculated from

$$f(v_\mathrm{f}) = f_\mathrm{b}(v_\mathrm{i}) \frac{\mathrm{d}v_\mathrm{f}(v_\mathrm{i})}{\mathrm{d}v_\mathrm{i}}. \tag{7.19}$$

Numerically integrating $f(v_\mathrm{f})$ from zero to the capture velocity v_c gives the fraction of trappable atoms. For example assuming $v_\mathrm{c} = 30\,\mathrm{m/s}$, $T = 673\,\mathrm{K}$, and the fraction of atoms trapped from a thermal beam is without slowing is

$$g = \int_0^{v_\mathrm{c}} f_\mathrm{b}(v)\mathrm{d}v = 3.9 \times 10^{-4}. \tag{7.20}$$

For the two examples with a slower beam shown in fig. 7.14 the number of atoms captured is increased at $g = 2.0\,\%$ (gain of 50) in the first case and $g = 7.6\,\%$ (gain of 200) in the second.

With the former calculations (section 7.1) we can finally predict the number of atoms in the MOT. For example I assume an oven flux of $1 \times 10^{14}\,\mathrm{s}^{-1}$, of which 14 % of

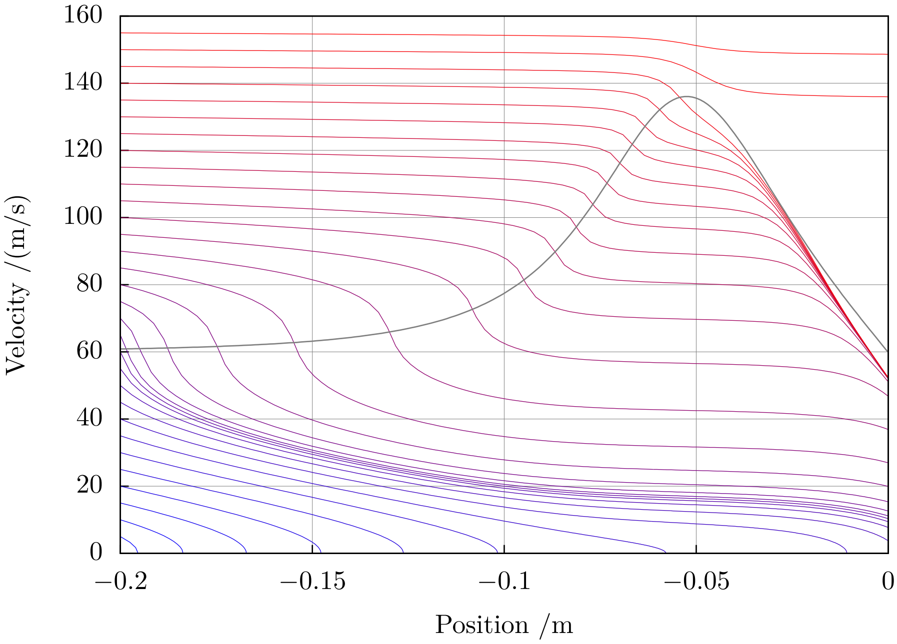

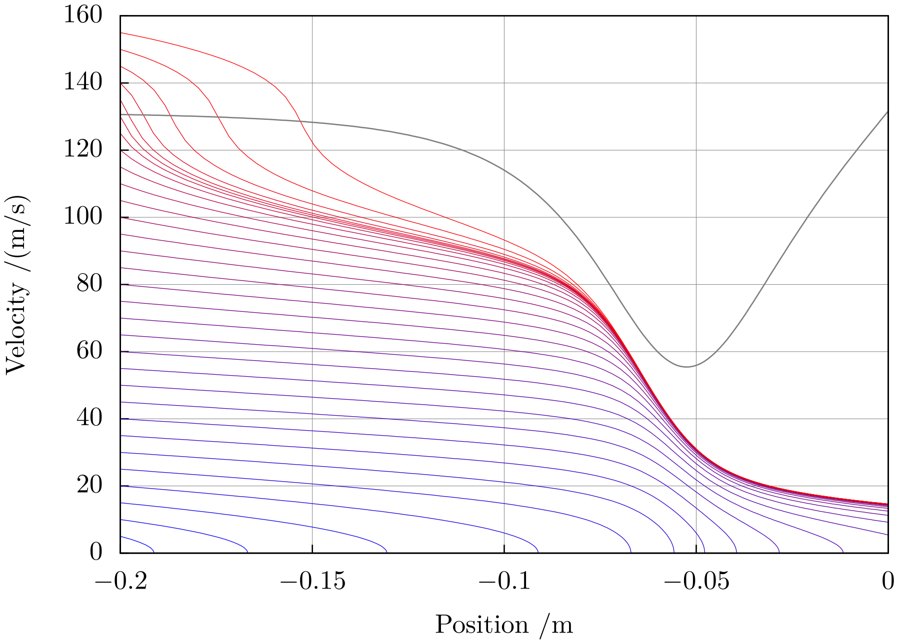

Figure 7.14: Numerical simulation of the trajectories in the phase space for atoms slowed by a beam with: top, $P = 8\,\mathrm{mW}$, $w = 4\,\mathrm{mm}$, $\delta = -2\pi \times 150\,\mathrm{MHz}$, polarization σ^-; bottom, $P = 20\,\mathrm{mW}$, $w = 4\,\mathrm{mm}$, $\delta = -2\pi \times 330\,\mathrm{MHz}$, polarization σ^+. The gray thick line shows the velocity at which the atoms are resonant with the light, modulated by the total magnetic field of the MOT coils.

^{171}Yb, a loss of 3×10^{-3} because of diffraction of the beam and the finite dimension of the differential-vacuum tube, and a fraction 2.0 % of atoms below the capture velocity. Then the total predicted capture rate is

$$R = 8 \times 10^{8}\,\mathrm{s}^{-1}. \tag{7.21}$$

In a simplified model the number of atom in MOT follows the equation $\dot{N} = R - \alpha N$, where $\alpha \approx 2\,\mathrm{s}^{-1}$ is the linear loss rate. This predict a maximum number of trappable atoms of $N_{\mathrm{max}} = R/\alpha = 2 \times 10^{8}$. The predicted value is 10 better than current state-of-the-art trap of alkaline-earth atoms, suggesting we are leaning on the safe side while designing our system.

8 Ytterbium optical clocks at NIST

Optical Frequency Measurement group at National Institute of Standards and Technology (NIST) laboratories in Boulder, Colorado has run a ytterbium optical frequency standard since 2005 [44, 45, 52, 72, 86, 152, 153]. I have been guest researcher of the NIST Optical Frequency Measurement group for six months in 2011. During my visit I helped with the laser setup for a second ytterbium optical clock and contributed to the measurement of the Stark effect in ytterbium.

This chapter is organized as follows. I will give a brief description of the first NIST ytterbium clock, as in [45]. Then I will describe the measurement of the Stark effect with this system and the consequent reduction of the blackbody radiation shift uncertainty. Finally I will give some details of setup for the second ytterbium clock.

8.1 First system

The experimental setup of the NIST ytterbium optical frequency standard is shown in fig. 8.1 The ytterbium source is an effusion oven externally heated. The oven is typically heated to temperatures between 450 °C and 500 °C [87] and a small hole in the oven creates a thermal atomic beam. The beam passes through a 3 mm aperture that allows for differential pumping before reaching the trapping region. The trapping chamber is a commercially available octagonal chamber. A window is placed opposed to the oven and is heated to prevent deposition of ytterbium.

The blue light at 399 nm is obtained by SHG of a diode laser in a PPKTP crystal using a duplication cavity. The green light at 556 nm is obtained by SHG from a ytterbium-doped fiber laser in a PPLN crystal working in single pass. The clock laser at 578 nm is obtained by SFG in a single-pass PPLN starting form a 1319 nm Nd:YAG laser and a 1030 nm erbium-doped fiber laser [100]. The clock laser is stabilized on either of two ultrastable ULE cavities, 29 cm long [114]. The lattice laser is a injection-locked Ti:sapphire laser. The frequency of the master laser (a diode laser) is locked to a ULE cavity.

When using ^{171}Yb, the NIST ytterbium optical frequency standard operates as follows (see fig. 8.2). Ytterbium atoms are trapped and cooled with the strong blue transition $^1\mathrm{S}_0{-}^1\mathrm{P}_1$ in the blue MOT, they are then transferred in the green MOT resonant with the intercombination transition $^1\mathrm{S}_0{-}^3\mathrm{P}_1$. Typically 1×10^5 atoms are captured and cooled to 15 µK in 350 ms. Atoms are then loaded into a 1D optical lattice at the magic wavelength 759 nm.

The lattice is obtained focusing 1 W of infrared light on a 30 µm waist. The lattice depth is typically $500E_\mathrm{r}$, where E_r is the recoil energy. Approximately 3×10^4

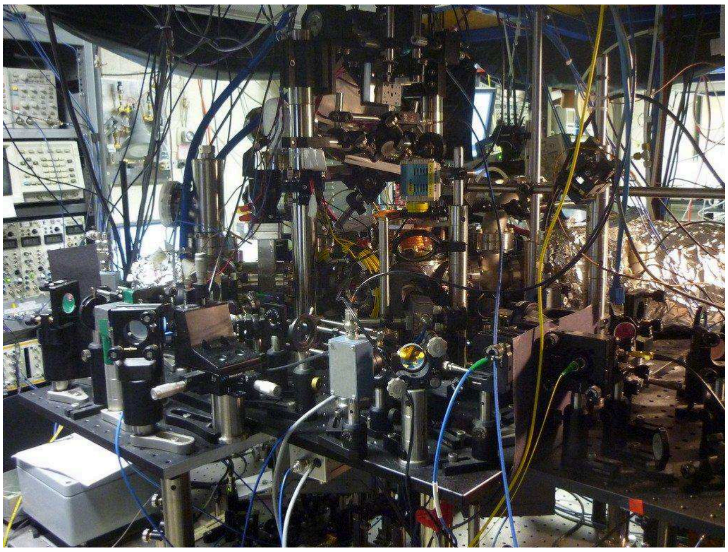

Figure 8.1: Setup of the first NIST ytterbium clock.

atoms with a temperature of 15 µK are captured. The atoms lifetime in the lattice is 300 ms, limited by the vacuum level in the trapping region (pressure 1×10^{-8} mbar or 1×10^{-6} Pa).

For the spectroscopy of ^{171}Yb an external magnetic field ($B = 0.11\,\mathrm{mT}$) is applied. This isotope has nuclear spin $I = 1/2$ while both states of the clock transition $^1\mathrm{S}_0{-}^3\mathrm{P}_0$ have $J = 0$ (total spin $F = I + J = 1/2$). The external magnetic field split both states with the total spin projection along the field $m_F = \pm 1/2$ (see fig. 8.3) The spectrum of the transition, for a linear polarized light, splits the transition in the two Zeeman components, as in fig. 8.4. Optical pumping using the green 556 nm transition is used to perform a state selection and brings all atoms in the $m_F = -1/2$ or $m_F = +1/2$ ground state.

Atoms are then probed by a 80 ms pulse of the clock laser, resulting in a Fourier limited linewidth of 10 Hz. The fraction of excited atoms are measured using three pulses of light at 399 nm resonant with the $^1\mathrm{S}_0{-}^1\mathrm{P}_1$ transition. The 399 nm fluorescence is recorded using a photomultiplier tube. The first pulse measures the atoms left in the ground state $^1\mathrm{S}_0$. The second pulse is used to detect the background laser scatter since no atoms should be left resonant with the blue light. Before applying the third pulse, atoms from the $^3\mathrm{P}_0$ state are pumped in the $^3\mathrm{D}_1$ state using a laser at 1389 nm on the $^3\mathrm{P}_0{-}^3\mathrm{D}_1$ transition. Atoms from the $^3\mathrm{D}_1$ state decay in the $^3\mathrm{P}_1$ state and here to the ground state where they are measured by third blue pulse. A small fraction of atoms ($\sim 3\,\%$) is lost in the metastable $^3\mathrm{P}_2$ state. The signal recorded from the 3 pulses is used to obtain a normalized excitation probability.

The clock laser is used to probe alternately the sides of the of the line of the two Zeeman components $m_F = \pm 1/2$. The clock laser is locked to the average of the two resonances, to be insensitive to the Zeeman effect.

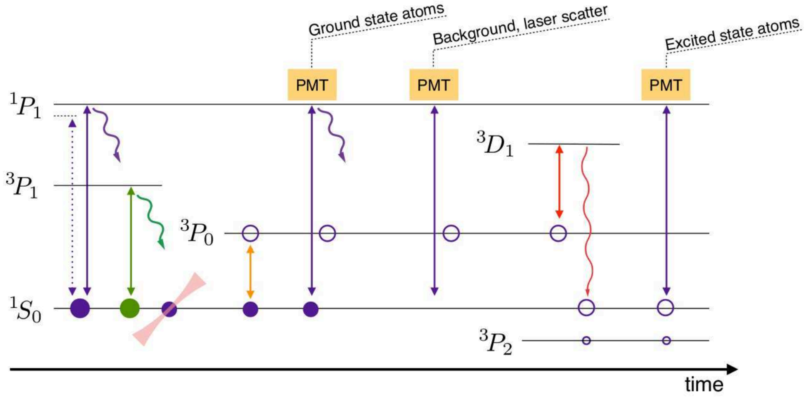

Figure 8.2: Sequence of operation for the NIST ytterbium clock [154].

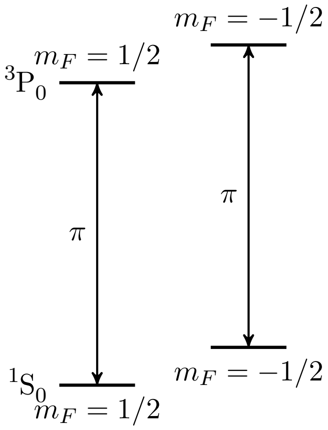

Figure 8.3: Zeeman components of the clock transition $^1\mathrm{S}_0$–$^3\mathrm{P}_0$ of $^{171}\mathrm{Yb}$ ($I = 1/2$) with an external magnetic field.

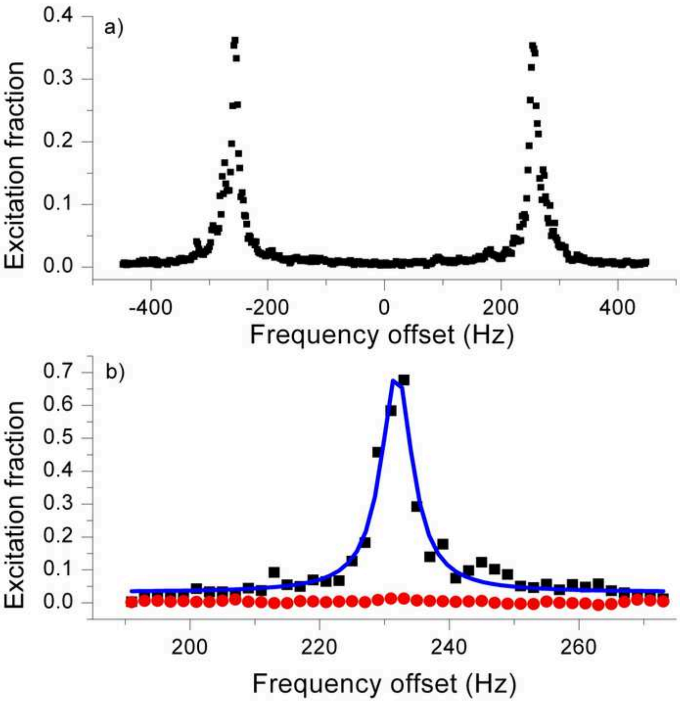

Figure 8.4: Spectrum of the clock transition $^1\mathrm{S}_0$–$^3\mathrm{P}_0$ of ^{171}Yb ($I = 1/2$) with an external magnetic field [45]: a, Zeeman split of the line (split 2.1 kHz/mT); b, close-up scan of one of the line with atoms pumped in (square) or away (circle) the $m_F = -1/2$ state. Solid line is a Lorentzian fit.

A detailed study of the uncertainty of the NIST ytterbium clock is reported in [45] and table 8.1 shows the stated uncertainty budget.

Table 8.1: Uncertainty budget of the NIST ^{171}Yb lattice frequency standard [45].

Effect	Shift/10^{-16}	Uncertainty/10^{-16}
Blackbody	-25.0	2.5
Lattice polarizability	0.4	2.0
Lattice hyperpolarizability	3.3	0.7
Cold collisions	-16.1	0.8
First-order Zeeman	0.4	0.4
Second-order Zeeman	-1.7	0.1
Probe light	0.05	0.2
Others	0	0.1
Total	-38.7	3.4

The major contribution to the total uncertainty reported in [45] comes from the blackbody radiation shift.

The electric field of blackbody radiation at temperature T is given by the Planck's law of radiation

$$E^2(\omega)\mathrm{d}\omega = \frac{\hbar}{\pi^2\epsilon_0 c^2}\frac{\omega^3\mathrm{d}\omega}{\mathrm{e}^{\hbar\omega/k_\mathrm{B}T}-1}, \tag{8.1}$$

where ϵ_0 is the vacuum permittivity. Blackbody radiation causes an ac Stark shift on the clock transition [6]:

$$\Delta\omega_0|_\mathrm{bb} = -\frac{1}{2\hbar}\int_0^\infty \alpha_0(\omega)E^2(\omega)\mathrm{d}\omega, \tag{8.2}$$

where $\alpha_0(\omega) = \alpha_\mathrm{e}(\omega) - \alpha_\mathrm{g}(\omega)$ is the differential polarizability of the clock transition and $\alpha_\mathrm{e,g}(\omega)$ are the polarizability of the excited and ground state at ω frequency. The maximum of $E^2(\omega)$ is given by Wien's displacement law

$$\omega_\mathrm{max} = 2\pi b' T, \tag{8.3}$$

where b' is the Wien frequency displacement law constant and at $T = 300\,\mathrm{K}$ $\omega_\mathrm{max} = 2\pi \times 17.6\,\mathrm{THz}$. In ytterbium the dipole-allowed transition from the ground state of lowest frequency is the green $^1\mathrm{S}_0$–$^3\mathrm{P}_1$ with a frequency $2\pi \times 752\,\mathrm{THz}$; from the clock state the lowest frequency corresponds to the transition $^1\mathrm{P}_0$–$^3\mathrm{D}_1$ at $2\pi \times 218\,\mathrm{THz}$. The main contribution to the blackbody radiation shift comes then from the static polarizability $\alpha_0(0)$, that is

$$\Delta\omega_0|_\mathrm{bb} \approx -\frac{1}{2\hbar}\alpha_0(0)\int_0^\infty E^2(\omega)\mathrm{d}\omega, \tag{8.4}$$

The integral gives the mean squared electric field

$$\langle E^2_\mathrm{bb}(t)\rangle = \int_0^\infty E^2(\omega)\mathrm{d}\omega = \frac{4\sigma T^4}{\epsilon_0 c}, \tag{8.5}$$

where $\sigma = \pi^2 k_\mathrm{B}^4/(60\hbar^3 c^2)$ is the Stefan-Boltzmann constant. Last formula gives $\langle E_\mathrm{bb}^2(t)\rangle = (8.319\,\mathrm{V/cm})^2$ at $T = 300\,\mathrm{K}$. The blackbody radiation shift can then be written

$$\Delta\omega_0|_\mathrm{bb} = \frac{2\sigma}{\epsilon_0 c\hbar}\alpha_0(0)T^4(1+\eta(T)) \tag{8.6}$$

where η is a small dynamic correction [155].

Theoretically calculations [155] gives $\alpha_0(0)/\hbar = 39(4)\,\mathrm{kHz(kV/cm)^{-2}}$ and $\eta(300\,\mathrm{K}) = 0.0145(15)$. The shift at $T = 300\,\mathrm{K}$ is then $\Delta\omega_0|_\mathrm{bb}/2\pi = -1.34(13)\,\mathrm{Hz}$ or in relative frequency $-2.50(25)\times 10^{-15}$ as reported in table 8.1. The uncertainty comes from the uncertainty in the theoretical value of $\alpha_0(0)$. This suggests that an experimental measurement of $\alpha_0(0)$ can bring a reduction in the uncertainty caused by blackbody radiation, as I am going to explain in the next section.

The second leading contribution to the uncertainty of the clock come from the lattice light shift (see eq. (2.26)). The magic wavelength has been measured varying the lattice laser intensity for different lattice frequencies. The magic frequency was determined 394 798 329(10) MHz. For a lattice depth of $500E_\mathrm{r}$ the sensitivity of the clock frequency on the lattice frequency around the magic wavelength is $-11(1)\,\mathrm{Hz/GHz}$ so this result in 2×10^{-16} uncertainty [45]. Another contribution comes from the lattice hyperpolarizability coming from two-photons resonances near the magic wavelength, as extensively studied in [72]. These evaluations are limited by the statistics on the magic frequency measurement; a reduced uncertainty at the level of 10^{-18} is feasible if needed [86].

The fourth large contribution comes from cold collision. If two or more atoms are captured in a single site of the optical lattice the interaction between them causes a frequency shift. The collision shift can be measured operating the clock alternating low and high number of atoms in the trap and using the ultrastable ULE cavity as a flywheel. A detailed study of the cold collision has been reported in [152]: using a Ramsey interrogation scheme [10] and varying the excitation fraction of the atoms in the lattice is possible to cancel to a large extent the collision shift, thus reducing its contribution down to 5×10^{-18}.

The instability of the NIST clock has been evaluated using the atomic transition [114]. Figure 8.5 shows the instability of the laser locked to the ULE cavity (local oscillator) using the atomic excitation as discriminator (out of loop). The instability is 4×10^{-16} at 1 s thanks to the large ULE spacer [114]. The same figure shows the in-loop stability when the stable laser is locked to the atomic transition, deduced from the error signal, the instability of interleaved measures used for example to evaluate the collision shift. This two measures are mostly limited by the Dick effect [101], the aliasing of the high frequency noise of the laser in a clock cycle time.

8.2 Atomic polarizability measurement

The leading contribution to uncertainty in the ytterbium clock evaluated at NIST comes from the blackbody radiation shift. This shift depends on the static atomic polarizability $\alpha = \alpha_0(0)$ whose theoretical knowledge is limited to a relative uncertainty of 10 %.

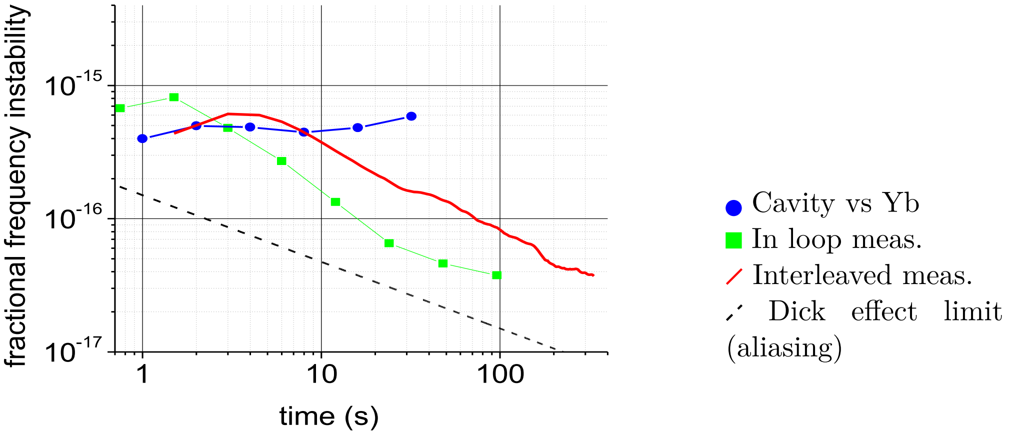

Figure 8.5: Instability of the NIST clock [114].

In 2011 the static atomic polarizability α has been measured to reduce the uncertainty coming from blackbody radiation [153, 156].

The polarizability can be measured recording the clock shift in an external electric field. The electric field could be that of a capacitor. For a voltage V across a capacitor made by two plane electrodes separated by a distance d the electric field is

$$\boldsymbol{E}_\mathrm{a} = \frac{V}{d}\boldsymbol{z}, \tag{8.7}$$

where $\boldsymbol{z}$ is the direction normal to the electrodes. The measures of the polarizability requires the accurate measure of V and d.

The experiment is similar to one done before with caesium [157]. Two flat transparent electrodes (fig. 8.6) are placed in the chamber of the NIST optical clock. Ytterbium atoms are trapped and probed in the optical lattice between the two plates.

The plates are made in fused silica and have a transparent conductive coating on the inner surface made in indium-tin-oxide (ITO). The plates have a diameter of 10 cm. The separation and parallelism of the plates is given by 3 precision fused silica spacers ($d \simeq 15$ mm, length deviation ~ 200 nm). The spacers are bond to the plate by hydroxide catalysis [158]. The spacer ends are wet with potassium hydroxide and contacted to the plates; the hydroxide etches the silica forming a solution that solidifies over time, resulting in a strong yet thin bond. Four metallic pads are deposited on each inner surface of the plates where they form 4 planar Fabry-Pérot etalons. The four etalons are used to measure the separation of the plates d and to check the parallelism of the plates. The validity of eq. (8.7) has been checked by FEM to ensure negligible deviation.

The voltage V across the capacitor has been measured with commercially available voltmeter with a relative uncertainty of few parts in 10^{-6}. A voltage up to 1 kV can be applied. The distance d should be measured with similar uncertainty by interferometric techniques. The free spectral range of the Fabry-Pérot etalons between the metallic pads

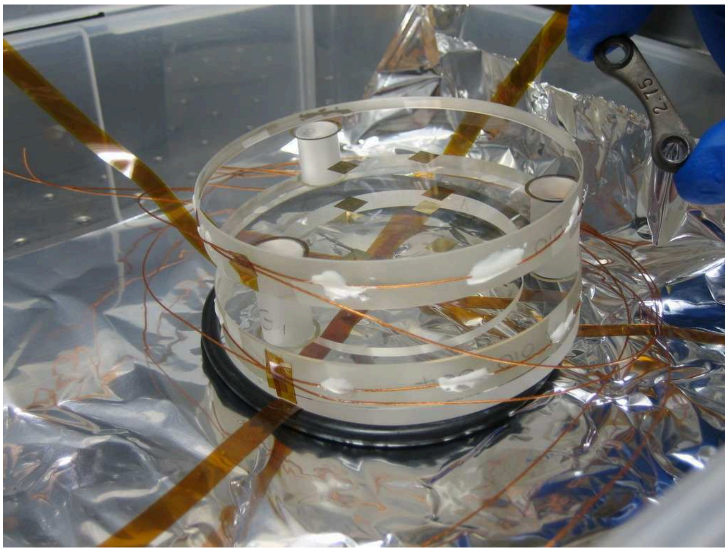

Figure 8.6: Transparent electrodes for the ytterbium polarizability measurement.

is

$$\mathit{\Delta}\nu_{\text{fsr}} = \frac{c}{2d} \simeq 10\,\text{GHz}. \tag{8.8}$$

The etalons have a finesse $\mathcal{F} \simeq 20$ or a linewidth of 500 MHz. The free spectral range can be measured by difference

$$\mathit{\Delta}\nu_{\text{fsr}} = \frac{\nu_N - \nu_0}{N} = \frac{\mathit{\Delta}\nu_N}{N}, \tag{8.9}$$

where ν_0 and ν_N are the frequency of one resonance and that of a resonance N fringes away. Measuring the frequencies ν_0 and ν_N with an uncertainty u (for example with a wavemeter) results in an uncertainty on the free spectral range that scales as $1/N$, $u_{\text{fsr}} = \sqrt{2}u/N$. Using a wavemeter the center of the fringe can be measured with an uncertainty $u = 50\,\text{MHz}$. An external cavity diode laser has been tuned for 17 THz around a central wavelength 766 nm so that $N_{\text{f}} \simeq 1700$. In principle one should count the number of fringes N continuously scanning the diode laser frequency. In practice another approach is simpler.

We can start measuring the free spectral range tuning the laser to two near fringes ($N = 1$) or from a priori knowledge of the spacer length. Suppose this measure has an uncertainty $u^{(0)}_{\text{fsr}}$. From another measure of a resonance ν_N, we can determine N without counting it $N = \mathit{\Delta}\nu_N/\mathit{\Delta}\nu_{\text{fsr}}$ with an uncertainty

$$u_N = \frac{u^{(0)}_{\text{fsr}}}{\mathit{\Delta}\nu^2_{\text{fsr}}}\mathit{\Delta}\nu_N + \frac{\sqrt{2}u}{\mathit{\Delta}\nu_{\text{fsr}}}, \tag{8.10}$$

where for simplicity sake I have neglected the possible correlation between $\mathit{\Delta}\nu_{\text{fsr}}$ and $\mathit{\Delta}\nu_N$. The second addend in the last equation does not depend on N and is $\simeq 7 \times 10^{-3} \ll$

1. The first addend scales as N, $u_N \sim N u_{\mathrm{fsr}}^{(0)}/\Delta\nu_{\mathrm{fsr}}$. For $N \ll \Delta\nu_{\mathrm{fsr}}/u_{\mathrm{fsr}}^{(0)}/$ the uncertainty is $u_N \ll 1$. Since we know N is an integer, under this condition N is determined exactly (this is an application of the Bayes theorem [159]). An updated measure of the free spectral range can be obtained $\Delta\nu_{\mathrm{fsr}} = \Delta\nu_N/N$ with reduced uncertainty $u_{\mathrm{fsr}}^{(1)} = \sqrt{2}u/N$. This procedure can be iterated, jumping to another resonance that can be further away because of the smaller starting uncertainty on the free spectral range. The number of fringes measured can increase exponentially for each jump. The statistically rigorous measure of the free spectral range can then be obtained by least-square fitting of the N, ν_N data.

For the NIST experiment one run on $N_{\mathrm{f}} \simeq 1700$ gives $\Delta\nu_{\mathrm{fsr}} = 9.9687(2)\,\mathrm{GHz}$ and $d = 15.0368(3)\,\mathrm{mm}$. The value of d has been obtained by averaging on 3 pairs of metallic pads.

The clock laser is locked to the ytterbium atoms kept between the plates in 3 interleaved cases: with both electrodes grounded (case A) and with one electrode grounded and the other at high voltage (case B and C). For the three conditions the Stark shifts of the clock transition are

$$\Delta\omega_{\mathrm{A}} = -\frac{\alpha}{2\hbar}\left|\boldsymbol{E}_{\mathrm{s}}\right|^2, \tag{8.11}$$

$$\Delta\omega_{\mathrm{B}} = -\frac{\alpha}{2\hbar}\left|\boldsymbol{E}_{\mathrm{a}} + \boldsymbol{E}_{\mathrm{s}}\right|^2, \tag{8.12}$$

$$\Delta\omega_{\mathrm{C}} = -\frac{\alpha}{2\hbar}\left|\boldsymbol{E}_{\mathrm{a}} - \boldsymbol{E}_{\mathrm{s}}\right|^2, \tag{8.13}$$

$$\tag{8.14}$$

where $\boldsymbol{E}_{\mathrm{a}}$ is the applied field, $\boldsymbol{E}_{\mathrm{s}}$ takes into account a possible stray field. For measuring the Stark shift the shift

$$\Delta\omega = \frac{1}{2}(\Delta\omega_{\mathrm{B}} + \Delta\omega_{\mathrm{C}}) - \Delta\omega_{\mathrm{A}} = -\frac{\alpha}{2\hbar}\left|\boldsymbol{E}_{\mathrm{a}}\right|^2 \tag{8.15}$$

gives a measure independent of the stray field. The component of the stray field parallel to the applied field can be measured by

$$\Delta\omega_{\mathrm{B}} - \Delta\omega_{\mathrm{C}} = -\frac{\alpha}{2\hbar}4\boldsymbol{E}_{\mathrm{s}}\cdot\boldsymbol{E}_{\mathrm{a}}. \tag{8.16}$$

In the NIST setup $\boldsymbol{E}_{\mathrm{s}}\cdot\boldsymbol{z} \simeq 0.1\,\mathrm{V/cm}$. This approach cancels a static stray field but not one varying synchronously with the applied field. For example charges can accumulate under the applied field but this effect has been checked varying the settling time of the field.

Figure 8.7 shows the Stark shift of eq. (8.15) as a function of the applied field magnitude. A quadratic fit is also shown with its residuals. Uncertainty in the shift come from the statistical average of the clock interleaved measures averaged for 1800 s. Fit is consistent with no quartic, cubic, linear or offset term. The resulting value for the polarizability is $\alpha/\hbar = 36.2612(7)\,\mathrm{kHz(kV/cm)^{-2}}$ in agreement with theoretical prediction [155] and where uncertainty is dominated by the systematic uncertainty in the measure of the voltage [153].

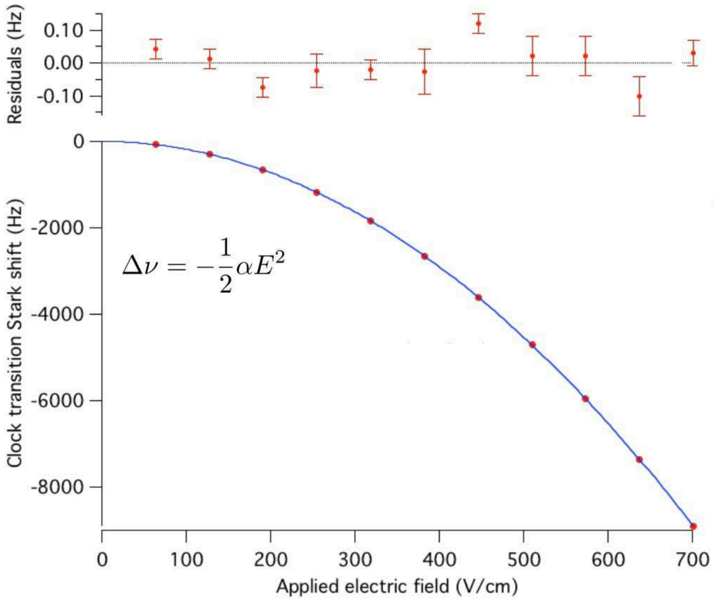

Figure 8.7: Quadratic Stark effect on the clock transition of ^{171}Yb. Data point are fitted with a parabola; upper plot shows the residuals.

Using this measure the evaluation of the blackbody radiation shift on the clock transition at $T = 300(1)\,\mathrm{K}$

$$\Delta\omega_0|_{\mathrm{bb}} = \frac{2\sigma}{\epsilon_0 c\hbar}\alpha T^4(1+\eta(T)) = -1.273(17)\,\mathrm{Hz}. \tag{8.17}$$

The uncertainty in the room temperature is the dominant term and an effective 1 K uncertainty results in a fractional uncertainty of the clock transition of 3×10^{-17}. A further reduction in uncertainty can be achieved in a cryogenic environment [13, 160]. At $T = 77(1)\,\mathrm{K}$ the uncertainty from the blackbody radiation shift reduce to 1×10^{-18}. A recent measurement of the lifetime of the $^3\mathrm{D}_1$ state of ytterbium reduced the uncertainty related to the dynamic correction η down to 1.1×10^{-18} (assuming an ideal blackbody environment at 300 K) [156].

8.3 Building a second clock

Having a second system has several advantages. First it allows an evaluation of the clock instability. The instability can be rigorously measured only against another standard of lower instability or building two similar systems. Then a second system can be used to check for systematic effects and for easy measurement of shifts. In particular comparing two clocks one can measure shifts not readily obtained by interleaved measured, for example the blackbody shift or Stark shift coming from stray charges [161].

Another possibility opened by running two clock side by side is comparison beyond the Dick limit [162]; when both system are probed at the same time by the same clock

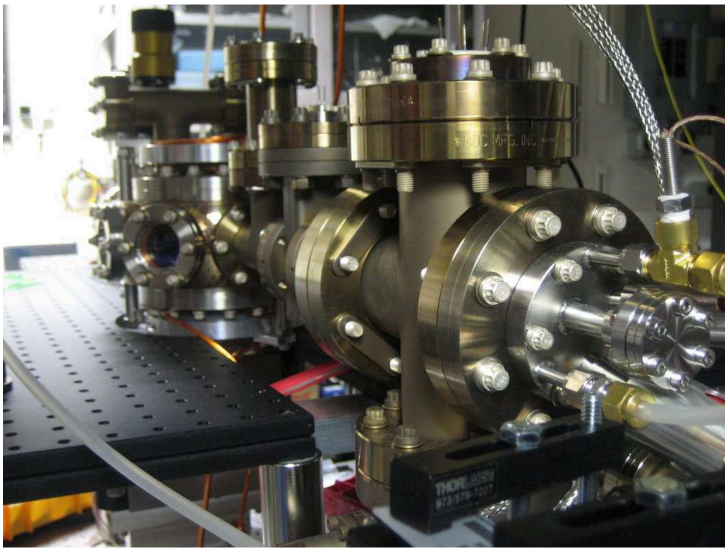

Figure 8.8: Vacuum chamber of the second ytterbium clock at NIST.

laser, the high-frequency noise of the laser is in common mode and can be rejected. Alternatively the Dick effect can be reduced by interleaving the two clocks: the atoms in one system can be probed while the atoms in the other are loading, greatly improving the duty cycle.

8.3.1 Experimental setup

The physic package of the second system in shown in fig. 8.8. The structure is divided in two parts: on one side the oven and on the other side a cleaner trapping region.

The oven is a commercial dual filament effusion cell, usually employed in molecular beam epitaxy setups. A $5\,\mathrm{cm}^3$ crucible contains the ytterbium ingot and the atomic beam is obtained by a small effusion hole. A shutter (usually sold for laser beams) is placed under vacuum to turn off the atomic beam when needed.

The trapping region is a commercial octagonal chamber with 7 viewports, mounted with Kasevich seals [142] for maximum optical access. As in the first setup a hot window is placed on the other side of the oven far from the trapping region.

Two coils with 30 loops each generates the magnetic field gradient for the MOT with a current of 100 A. The wire for the coils are hollow, with a square cross-section, and water flows in it for cooling.

A differential-vacuum tube, long 15 cm and with an internal diameter of 5 mm (fig. 8.9) is used to keep a pressure ratio between the oven side and the trapping side. On both sides there is an ion pump (pumping speed 40 L/s). A non-evaporable getter pump for hydrogen is placed on the trapping side, as close as possible to the MOT, because collisions with hydrogen gas (H_2) is thought to be responsible for the lifetime of atoms in the lattice of the first system. Pressure in the MOT chamber has been measured 5×10^{-10} mbar (5×10^{-8} Pa); this is a factor of 20 better than the first system and

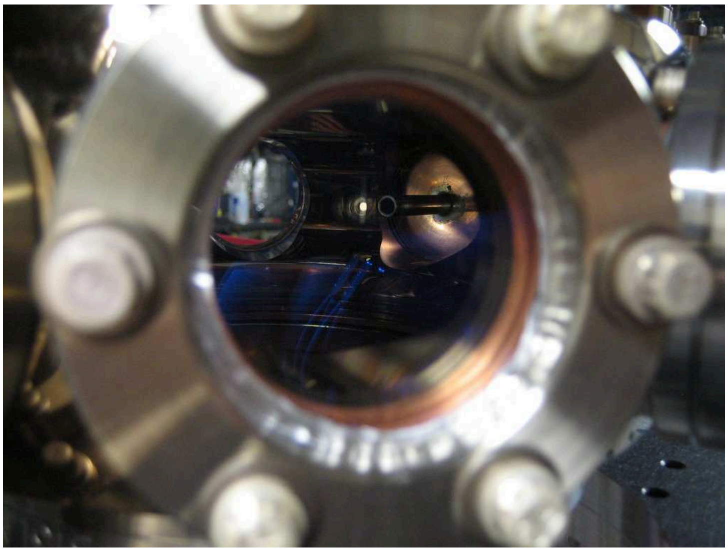

Figure 8.9: The differential vacuum tube in the second ytterbium clock at NIST.

should allow for several seconds of lifetime in the lattice. Pressure on the oven side is 1×10^{-8} mbar (1×10^{-6} Pa).

8.3.2 Blue and green laser

Commercially available lasers at 399 nm and at 556 nm are used for the double stage MOT.

The 399 nm laser is a Toptica TA SHG Pro laser. It is a infrared diode laser with a built-in tapered amplifier and duplication cavity. It has an output of 150 mW at 399 nm.

The blue laser is used for the MOT trapping beams, for a slower beam and for a probe beam (fig. 8.10). The laser is frequency locked to the ytterbium resonance in a hollow cathode lamp, where saturated absorption spectroscopy is performed with the modulation transfer technique [163, 164].

The 556 nm light is obtained from a 1112 nm fiber laser, the Menlo Orange One, that has its own SHG stage. The output power at 556 nm is 100 mW, much more than needed for the green MOT that requires ~ 10 mW. The same laser can be used for the second stage MOT of both the old and the new system. Its frequency is locked to a ULE cavity and it is used for trapping and optical pumping of the atom state (fig. 8.11).

The blue and green trapping beams are delivered to the vacuum chamber as in fig. 8.12. Both are fiber-coupled and collimated to a large diameter with an achromatic lens. For the blue the lens has a focal of $f = 60$ mm and the beam a diameter of 10 mm. For the green the lens has a focal of $f = 40$ mm and the beam a diameter of 7 mm. Both lasers polarizations are cleaned with a polarizing cube. Then they are split in 3 beams using 2 $\lambda/2$ waveplates and 2 polarizing cubes. The blue and green beams are superimposed on 3 dichroic mirrors, one for each axis of the MOT. This allows independent alignment of the green and blue beams on the MOT.

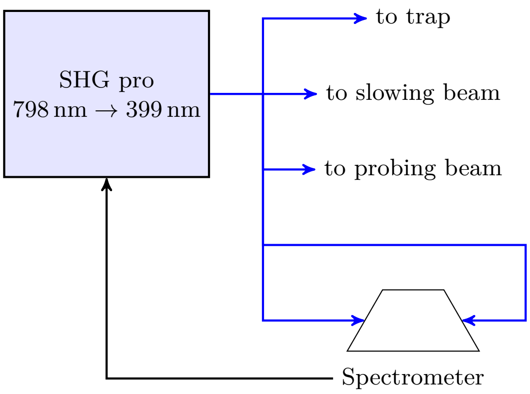

Figure 8.10: Scheme for the blue 399 nm radiation in the second system.

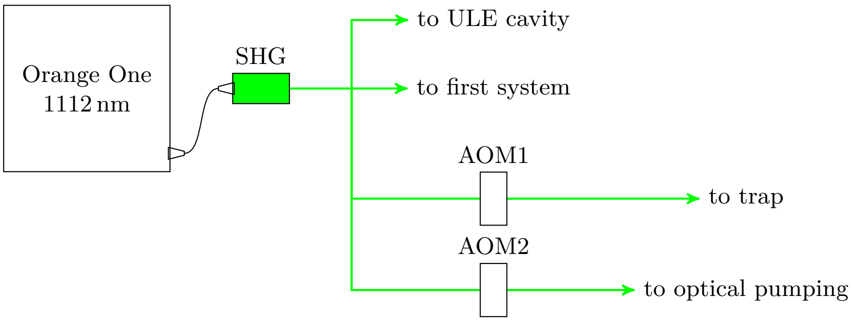

Figure 8.11: Scheme for the green 556 nm radiation in the second system.

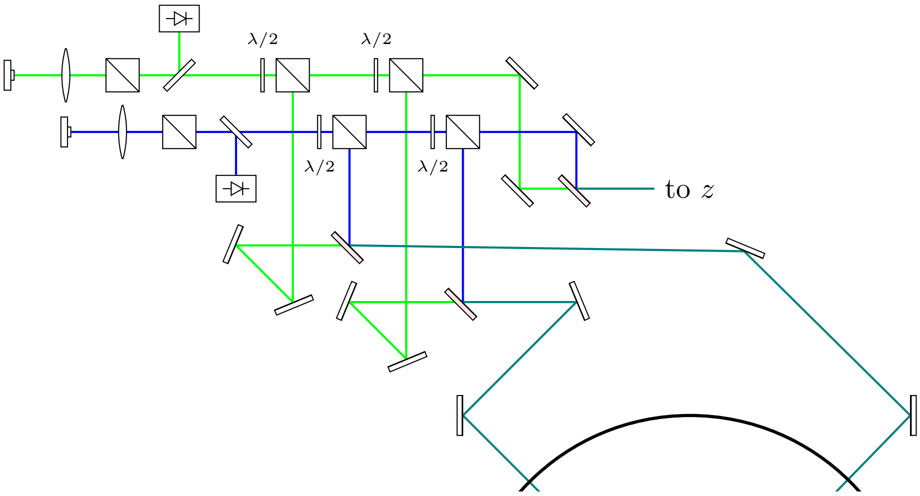

Figure 8.12: Scheme of the optics bench for the blue and green trapping beams.

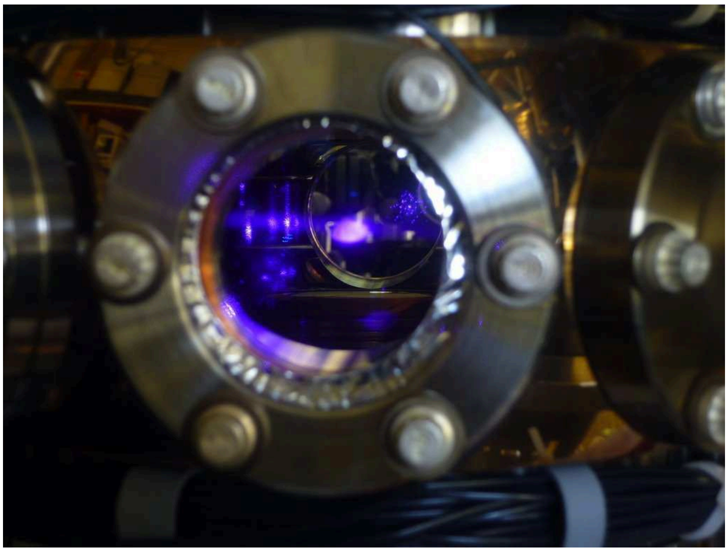

Figure 8.13: Blue 399 nm MOT in the second NIST setup.

A bright blue MOT (fig. 8.13) was observed in the last days of my stay at NIST.

8.3.3 Injection-locking of the lattice laser

At NIST I also worked on the Ti:sapphire laser for the lattice at 759 nm.

The Ti:sapphire laser is a M Squared Soltsis pumped by a 10 W solid-state green laser (Lighthouse photonics Sprout). The Ti:sapphire laser has a bow-tie ring cavity. For maximum power the cavity is empty, except for the Ti:sapphire crystal, with no optics for wavelength selection or single-direction lasing. Single-mode lasing is achieved by injection-locking with an extended cavity diode laser (fig. 8.14).

The frequency of the master diode laser is locked to the Ti:sapphire cavity with the Pound-Drever-Hall technique. The diode laser is protected by two optical isolators, modulated by a resonant EOM (15 MHz) and mode-matched to the Ti:sapphire cavity. The master is injected through the output coupler of the Ti:sapphire cavity. The reflection needed for the Pound-Drever-Hall signal is thus superimposed to the main laser output. A pick-off and a neutral filter are used to extract a weak beam to be sent to a fast photodiode. The Pound-Drever-Hall signal so obtained is used for locking the master frequency to the Ti:sapphire cavity acting on the current of the diode laser (fast lock) and on its piezo (slow lock).

When the master is locked, the Ti:sapphire lases in single mode and only in one direction. The output of the other direction can be monitored with a photodiode. It drops to zero when the lock is properly executed; a small output can be observed is the injection is not good enough and the Ti:sapphire is lasing multimode.

The Ti:sapphire cavity can be locked to an external reference (for example a ULE cavity) acting on a piezo on one of its mirrors.

The main output of the laser is sent to an AOM at 80 MHz that is used for intensity

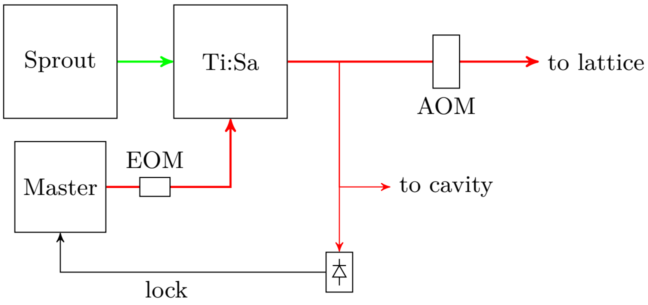

Figure 8.14: Injection locking of the lattice laser.

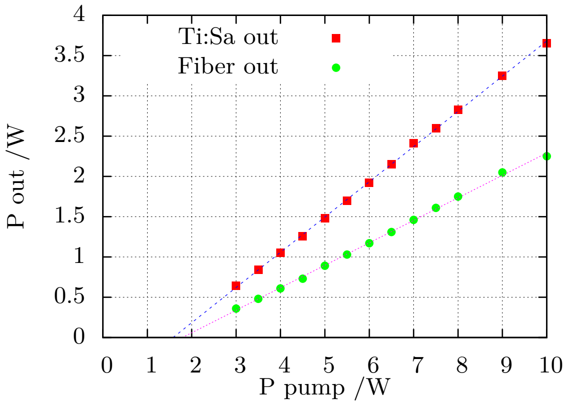

Figure 8.15: Output power of the Ti:sapphire laser and available power after the fiber.

stabilization. The first order of the AOM is coupled in a high-power fiber for delivery to the experiment. The AOM works also as an isolator, since backreflections are frequency shifted out of resonance of the cavity.

Figure 8.15 shows the power output of the Ti:sapphire laser while injected as a function of the pump power. The same figure shows also the available power at 759 nm after the AOM and the fiber. A maximum power of 3.6 W has been measured out of the laser of which 2.2 W are available out of the fiber. This is more than enough for a typical 1D lattice, that works usually at 1 Wand is retroreflected.

9 Conclusions

With my work for the Ph.D. course in metrology of the Politecnico di Torino I contributed to the development of an optical frequency standrad based on cold ytterbium atoms in the laboratories of the Optical Division of Istituto Nazionale di Ricerca Metrologica (INRIM). I have also been guest reasearcher of the Optical Frequency Measurement group of National Institute of Standards and Technology (NIST) in 2011.

Several important milestone have been achieved during my work at INRIM. All the lasers needed for clock operation have been realized. The radiations for a two-stage MOT at 399 nm and 556 nm were obtained by second harmonic generation in non-linear crystals. In particular a recent upgrade of the 399 nm system allowed an improvement of the power and stability of this laser source. The clock laser at 578 nm was obtained by sum frequency generation in a compact setup. The Ti:sapphire laser that will be used as optical lattice has been recently installed in January 2013, completing the ensemble of laser sources of the experiment.

The frequency of the laser at 578 nm was stabilized using the Pound-Drever-Hall technique on a ultrastable Fabry-Pérot cavity to a level of 3×10^{-15} at 1 s. The frequency noise of the laser has been characterized and it is suitable for the spectroscopy of the clock transition of ytterbium. An innovative control scheme based on Active Disturbance Rejection Control (ADRC) was implemented for the stabilization of the temperature of the cavity. One of the ultrastable ULE cavities of INRIM was recently moved to the European Laboratory for Non-Linear Spectroscopy (LENS) in Florence, where L. Fallani group is working on a experiment with quantum-degenerate gases of ytterbium. The ultrastable laser will be used on ytterbium atoms to simulate extra dimensions and as a tool for quantum information. A new cavity using fused silica mirrors with ULE rings, with lower thermal noise, is planned for the INRIM experiment.

Ytterbium atoms were cooled and trapped in the blue 399 nm MOT and in the green 556 nm MOT. The last result was achieved at INRIM in 2012 with the present setup. A new experimental setup have been designed to overcome some of the drawbacks of the current system. It is planned to have a better vaccum level, a higher number of trappable atoms and a wider optical access for experiments. The new setup is now in progress. The new atomic oven source has been already mounted and tested. Other parts of the vaccum chamber are being assembled. Cooling and trapping of ytterbium atoms in the double-stage MOT in the new chamber is expected for the next months and the successive step will be the transfer of atoms in the optical lattice.

At NIST I contributed to the development of a second setup for a ytterbium optical clock allowing a direct comparison of two state-of-the-art optical standards. The measurement of the Stark effect in ytterbium made at NIST is useful to reduce the uncertainty coming from blackbody radition on the ytterbium transition. Metrologicak characterizations carried on so far allow to reasonably expect ytterbium clock uncertainty heading to 10^{-17} in the near future.

Bibliography

[1] L. D. Landau and E. M. Lifshitz, *Quantum mechanics - Non-relativistic theory*, volume 3 of *Course of Theoretical Physics* (Pergamon Press, 1977), 3rd edition

[2] L. Essen and J. V. L. Parry, "An Atomic Standard of Frequency and Time Interval: A Caesium Resonator," *Nature*, **176**, pp. 280–282 (1955)

[3] BIPM, *The International System of Units (SI)* (2006), 8th edition

[4] W. Markowitz, R. G. Hall, L. Essen, and J. V. L. Parry, "Frequency of Cesium in Terms of Ephemeris Time," *Phys. Rev. Lett.*, **1**, pp. 105–107 (1958)

[5] D. B. Sullivan, D. W. Allan, D. A. Howe, and F. L. Walls, editors, *Characterization of clocks and oscillators*, NIST Tech. Note 1337 (1990)

[6] W. M. Itano, L. L. Lewis, and D. J. Wineland, "Shift of $^2S_{\frac{1}{2}}$ hyperfine splittings due to blackbody radiation," *Phys. Rev. A*, **25**, pp. 1233–1235 (1982)

[7] D. Allan, "Statistics of atomic frequency standards," *Proc. IEEE*, **54**, pp. 221–230 (1966)

[8] W. M. Itano, J. C. Bergquist, J. J. Bollinger, J. M. Gilligan, D. J. Heinzen, F. L. Moore, M. G. Raizen, and D. J. Wineland, "Quantum projection noise: Population fluctuations in two-level systems," *Phys. Rev. A*, **47**, pp. 3554–3570 (1993)

[9] L. Hollberg, C. Oates, E. Curtis, E. Ivanov, S. Diddams, T. Udem, H. Robinson, J. Bergquist, R. Rafac, W. Itano, R. Drullinger, and D. Wineland, "Optical frequency standards and measurements," *Quantum Electronics, IEEE Journal of*, **37**, pp. 1502–1513 (2001)

[10] N. F. Ramsey, "A Molecular Beam Resonance Method with Separated Oscillating Fields," *Phys. Rev.*, **78**, pp. 695–699 (1950)

[11] H. J. Metcalf and P. van der Straten, *Laser cooling and trapping* (Springer, New York, 2002)

[12] R. Wynands and S. Weyers, "Atomic fountain clocks," *Metrologia*, **42**, p. S64 (2005)

[13] F. Levi, C. Calosso, D. Calonico, L. Lorini, E. Bertacco, A. Godone, G. Costanzo, B. Mongino, S. Jefferts, T. Heavner, and E. Donley, "Cryogenic fountain development at NIST and INRIM: preliminary characterization," *IEEE Trans. Ultrason., Ferroelect., Freq. Cont.*, **57**, pp. 600–605 (2010)

[14] G. Santarelli, P. Laurent, P. Lemonde, A. Clairon, A. G. Mann, S. Chang, A. N. Luiten, and C. Salomon, "Quantum Projection Noise in an Atomic Fountain: A High Stability Cesium Frequency Standard," *Phys. Rev. Lett.*, **82**, pp. 4619–4622 (1999)

[15] K. Evenson, J. Wells, F. Petersen, B. Danielson, and G. Day, "Accurate frequencies of molecular transitions used in laser stabilization: the 3.39 µm transition in CH_4 and the 9.33 and 10.18 µm transitions in CO_2," *Appl. Phys. Lett.*, **22**, pp. 192–195 (1973)

[16] K. M. Evenson, J. S. Wells, F. R. Petersen, B. L. Danielson, G. W. Day, R. L. Barger, and J. L. Hall, "Speed of Light from Direct Frequency and Wavelength Measurements of the Methane-Stabilized Laser," *Phys. Rev. Lett.*, **29**, pp. 1346–1349 (1972)

[17] C. R. Pollock, D. A. Jennings, F. R. Petersen, J. S. Wells, R. E. Drullinger, E. C. Beaty, and K. M. Evenson, "Direct frequency measurements of transitions at 520 THz (576 nm) in iodine and 260 THz (1.15 µm) in neon," *Opt. Lett.*, **8**, pp. 133–135 (1983)

[18] D. A. Jennings, C. R. Pollock, F. R. Petersen, R. E. Drullinger, K. M. Evenson, J. S. Wells, J. L. Hall, and H. P. Layer, "Direct frequency measurement of the I2-stabilized He-Ne 433 THz (633 nm) laser," *Opt. Lett.*, **8**, pp. 136–138 (1983)

[19] S. A. Diddams, J. C. Bergquist, S. R. Jefferts, and C. W. Oates, "Standards of Time and Frequency at the Outset of the 21st Century," *Science*, **306**, pp. 1318–1324 (2004)

[20] L. Hollberg, C. W. Oates, G. Wilpers, C. W. Hoyt, Z. W. Barber, S. A. Diddams, W. H. Oskay, and J. C. Bergquist, "Optical frequency/wavelength references," *J. Phys. B: At. Mol. Opt. Phys.*, **38**, p. S469 (2005)

[21] B. C. Young, F. C. Cruz, W. M. Itano, and J. C. Bergquist, "Visible Lasers with Subhertz Linewidths," *Phys. Rev. Lett.*, **82**, pp. 3799–3802 (1999)

[22] R. W. Boyd, *Nonlinear Optics* (Academic Press, 2008), third edition

[23] T. Udem, J. Reichert, R. Holzwarth, and T. W. Hänsch, "Accurate measurement of large optical frequency differences with a mode-locked laser," *Opt. Lett.*, **24**, pp. 881–883 (1999)

[24] T. Udem, R. Holzwarth, and T. W. Hansch, "Optical frequency metrology," *Nature*, **416**, pp. 233–237 (2002)

[25] S. T. Cundiff and J. Ye, "*Colloquium* : Femtosecond optical frequency combs," *Rev. Mod. Phys.*, **75**, pp. 325–342 (2003)

[26] J. Ye and S. T. Cundiff, editors, *Femtosecond Optical Frequency Comb: Principle, Operation, and Applications* (Kluwer Academic Publishers / Springer, Norwell, MA, 2004)

[27] R. H. Dicke, "The Effect of Collisions upon the Doppler Width of Spectral Lines," *Phys. Rev.*, **89**, pp. 472–473 (1953)

[28] D. J. Wineland and W. M. Itano, "Laser cooling of atoms," *Phys. Rev. A*, **20**, pp. 1521–1540 (1979)

[29] F. Diedrich, J. C. Bergquist, W. M. Itano, and D. J. Wineland, "Laser Cooling to the Zero-Point Energy of Motion," *Phys. Rev. Lett.*, **62**, pp. 403–406 (1989)

[30] W. H. Oskay, S. A. Diddams, E. A. Donley, T. M. Fortier, T. P. Heavner, L. Hollberg, W. M. Itano, S. R. Jefferts, M. J. Delaney, K. Kim, F. Levi, T. E. Parker, and J. C. Bergquist, "Single-Atom Optical Clock with High Accuracy," *Phys. Rev. Lett.*, **97**, p. 020 801 (2006)

[31] T. Rosenband, D. B. Hume, P. O. Schmidt, C. W. Chou, A. Brusch, L. Lorini, W. H. Oskay, R. E. Drullinger, T. M. Fortier, J. E. Stalnaker, S. A. Diddams, W. C. Swann, N. R. Newbury, W. M. Itano, D. J. Wineland, and J. C. Bergquist, "Frequency Ratio of Al^+ and Hg^+ Single-Ion Optical Clocks; Metrology at the 17th Decimal Place," *Science*, **319**, pp. 1808–1812 (2008)

[32] C. W. Chou, D. B. Hume, J. C. J. Koelemeij, D. J. Wineland, and T. Rosenband, "Frequency Comparison of Two High-Accuracy Al^+ Optical Clocks," *Phys. Rev. Lett.*, **104**, p. 070 802 (2010)

[33] H. S. Margolis, G. P. Barwood, G. Huang, H. A. Klein, S. N. Lea, K. Szymaniec, and P. Gill, "Hertz-Level Measurement of the Optical Clock Frequency in a Single $^{88}\mathrm{Sr}^+$ Ion," *Science*, **306**, pp. 1355–1358 (2004)

[34] A. A. Madej, P. Dubé, Z. Zhou, J. E. Bernard, and M. Gertsvolf, "$^{88}\mathrm{Sr}^+$ 445-THz Single-Ion Reference at the 10^{-17} Level via Control and Cancellation of Systematic Uncertainties and Its Measurement against the SI Second," *Phys. Rev. Lett.*, **109**, p. 203 002 (2012)

[35] C. Tamm, B. Lipphardt, H. Schnatz, R. Wynands, S. Weyers, T. Schneider, and E. Peik, "$^{171}\mathrm{Yb}^+$ single-ion optical frequency standard at 688 THz," in "International Frequency Control Symposium and Exposition, 2006 IEEE," pp. 457–461 (2006)

[36] U. Sterr, C. Degenhardt, H. Stoehr, C. Lisdat, H. Schnatz, J. Helmcke, F. Riehle, G. Wilpers, C. Oates, and L. Hollberg, "The optical calcium frequency standards of PTB and NIST," *Comptes Rendus Physique*, **5**, pp. 845–855 (2004)

[37] H. Katori, M. Takamoto, V. G. Pal'chikov, and V. D. Ovsiannikov, "Ultrastable Optical Clock with Neutral Atoms in an Engineered Light Shift Trap," *Phys. Rev. Lett.*, **91**, p. 173 005 (2003)

[38] M. Takamoto, F.-L. Hong, R. Higashi, and H. Katori, "An optical lattice clock," *Nature*, **435**, pp. 321–324 (2005)

[39] A. D. Ludlow, T. Zelevinsky, G. K. Campbell, S. Blatt, M. M. Boyd, M. H. G. de Miranda, M. J. Martin, J. W. Thomsen, S. M. Foreman, J. Ye, T. M. Fortier, J. E. Stalnaker, S. A. Diddams, Y. Le Coq, Z. W. Barber, N. Poli, N. D. Lemke, K. M. Beck, and C. W. Oates, "Sr Lattice Clock at 1×10^{-16} Fractional Uncertainty by Remote Optical Evaluation with a Ca Clock," *Science*, **319**, pp. 1805–1808 (2008)

[40] N. Poli, M. G. Tarallo, M. Schioppo, C. W. Oates, and G. M. Tino, "A simplified optical lattice clock," *Applied Physics B*, **97**, pp. 27–33 (2009)

[41] S. Falke, H. Schnatz, J. S. R. V. Winfred, T. Middelmann, S. Vogt, S. Weyers, B. Lipphardt, G. Grosche, F. Riehle, U. Sterr, and C. Lisdat, "The ^{87}Sr optical frequency standard at PTB," *Metrologia*, **48**, p. 399 (2011)

[42] J. Friebe, A. Pape, M. Riedmann, K. Moldenhauer, T. Mehlstäubler, N. Rehbein, C. Lisdat, E. M. Rasel, W. Ertmer, H. Schnatz, B. Lipphardt, and G. Grosche, "Absolute frequency measurement of the magnesium intercombination transition $^1\mathrm{S}_0 \rightarrow {}^3\mathrm{P}_1$," *Phys. Rev. A*, **78**, p. 033 830 (2008)

[43] J. J. McFerran, L. Yi, S. Mejri, S. Di Manno, W. Zhang, J. Guéna, Y. Le Coq, and S. Bize, "Neutral Atom Frequency Reference in the Deep Ultraviolet with Fractional Uncertainty $= 5.7 \times 10^{-15}$," *Phys. Rev. Lett.*, **108**, p. 183 004 (2012)

[44] N. Poli, Z. W. Barber, N. D. Lemke, C. W. Oates, L. S. Ma, J. E. Stalnaker, T. M. Fortier, S. A. Diddams, L. Hollberg, J. C. Bergquist, A. Brusch, S. Jefferts, T. Heavner, and T. Parker, "Frequency evaluation of the doubly forbidden $^1\mathrm{S}_0 \rightarrow {}^1\mathrm{P}_3$ transition in bosonic ^{174}Yb," *Phys. Rev. A*, **77**, p. 050 501 (2008)

[45] N. D. Lemke, A. D. Ludlow, Z. W. Barber, T. M. Fortier, S. A. Diddams, Y. Jiang, S. R. Jefferts, T. P. Heavner, T. E. Parker, and C. W. Oates, "Spin-1/2 Optical Lattice Clock," *Phys. Rev. Lett.*, **103**, p. 063 001 (2009)

[46] T. Kohno, M. Yasuda, K. Hosaka, H. Inaba, Y. Nakajima, and F.-L. Hong, "One-Dimensional Optical Lattice Clock with a Fermionic ^{171}Yb Isotope," *Applied Physics Express*, **2**, p. 072 501 (2009)

[47] D. Calonico, F. Levi, L. Lorini, G. Costanzo, M. Zoppi, M. Pizzocaro, A. Mura, E. K. Bertacco, and A. Godone, "Yb optical lattice clock at INRIM," in "Proceedings of the 24th European Frequency and Time forum," P2.27 (2010)

[48] M. Yasuda, H. Inaba, T. Kohno, T. Tanabe, Y. Nakajima, K. Hosaka, D. Akamatsu, A. Onae, T. Suzuyama, M. Amemiya, and F.-L. Hong, "Improved Absolute Frequency Measurement of the ^{171}Yb Optical Lattice Clock towards a Candidate for the Redefinition of the Second," *Applied Physics Express*, **5**, p. 102 401 (2012)

[49] C. Y. Park, D.-H. Yu, W.-K. Lee, S. E. Park, E. B. Kim, S. K. Lee, J. W. Cho, T. H. Yoon, J. Mun, S. J. Park, T. Y. Kwon, and S.-B. Lee, "Absolute frequency measurement of ^{1}S$_0$ ($F = 1/2$) - ^{3}P$_0$ ($F = 1/2$) transition of ^{171}Yb atoms in a one-dimensional optical lattice at KRISS," *Metrologia*, **50**, p. 119 (2013)

[50] M. Lombardi, T. Heavner, and S. Jefferts, "NIST Primary Frequency Standards and the Realization of the SI Second," *NCSL International Measure*, **2**, pp. 74–89 (2007)

[51] J. Ye, H. Schnatz, and L. Hollberg, "Optical frequency combs: from frequency metrology to optical phase control," *Selected Topics in Quantum Electronics, IEEE Journal of*, **9**, pp. 1041–1058 (2003)

[52] C. W. Hoyt, Z. W. Barber, C. W. Oates, T. M. Fortier, S. A. Diddams, and L. Hollberg, "Observation and Absolute Frequency Measurements of the ^{1}S$_0$-^{3}P$_0$ Optical Clock Transition in Neutral Ytterbium," *Phys. Rev. Lett.*, **95**, p. 083 003 (2005)

[53] C. Abou-Jaoudeh, C. Bruni, F. Baumer, and A. Gorlitz, "A compact source of ultracold ytterbium for an optical lattice clock," in "Frequency Control Symposium, 2009 Joint with the 22nd European Frequency and Time forum. IEEE International," pp. 756 –759 (2009)

[54] D. DeMille, "Parity Nonconservation in the $6s^{21}S_0 \rightarrow 6s5d^3D_1$ Transition in Atomic Ytterbium," *Phys. Rev. Lett.*, **74**, pp. 4165–4168 (1995)

[55] Y. Takasu, K. Maki, K. Komori, T. Takano, K. Honda, M. Kumakura, T. Yabuzaki, and Y. Takahashi, "Spin-Singlet Bose-Einstein Condensation of Two-Electron Atoms," *Phys. Rev. Lett.*, **91**, p. 040 404 (2003)

[56] T. Fukuhara, Y. Takasu, M. Kumakura, and Y. Takahashi, "Degenerate Fermi Gases of Ytterbium," *Phys. Rev. Lett.*, **98**, p. 030 401 (2007)

[57] K. Honda, Y. Takasu, T. Kuwamoto, M. Kumakura, Y. Takahashi, and T. Yabuzaki, "Optical dipole force trapping of a fermion-boson mixture of ytterbium isotopes," *Phys. Rev. A*, **66**, p. 021 401 (2002)

[58] D. Hayes, P. S. Julienne, and I. H. Deutsch, "Quantum Logic via the Exchange Blockade in Ultracold Collisions," *Phys. Rev. Lett.*, **98**, p. 070 501 (2007)

[59] F. Levi, L. Lorini, D. Calonico, and A. Godone, "IEN-CsF1 accuracy evaluation and two-way frequency comparison," *IEEE Trans. Ultrason., Ferroelect., Freq. Cont.*, **51**, pp. 1216–1224 (2004)

[60] M. Pizzocaro, G. Costanzo, A. Godone, F. Levi, A. Mura, M. Zoppi, and D. Calonico, "Realization of an ultrastable 578-nm laser for an Yb lattice clock," *IEEE Trans. Ultrason., Ferroelect., Freq. Cont.*, **59**, pp. 426–431 (2012)

[61] C. Clivati, *Sorgente laser ultrastabile a* 1.5 µm *e link ottico per il confronto remoto al subfemtosecondo di orologi atomici*, Tesi di laurea specialistica, Universita degli Studi di Torino (2010)

[62] C. Clivati, A. Mura, D. Calonico, F. Levi, G. Costanzo, C. Calosso, and A. Godone, "Planar-waveguide external cavity laser stabilization for an optical link with 10^{-19} frequency stability," *IEEE Trans. Ultrason., Ferroelect., Freq. Cont.*, **58**, pp. 2582–2587 (2011)

[63] D. Calonico, C. Clivati, G. A. Costanzo, A. Godone, F. Levi, M. Marchetti, A. Mura, M. Prevedelli, M. Schioppo, G. M. Tino, M. E. Zucco, and N. Poli, "Optical Frequency Link between Torino and Firenze for remote comparison between Yb and Sr optical clocks," in "Proceedings of the 26th European Frequency and Time forum," pp. 396–399 (2012)

[64] CCTF, "Consultative Committee for Time and Frequency. Report of the 19th meeting (13–14 September 2012) to the International Committee for Weights and Measures," (2012)

[65] W. D. Phillips and H. Metcalf, "Laser Deceleration of an Atomic Beam," *Phys. Rev. Lett.*, **48**, pp. 596–599 (1982)

[66] S. Chu, L. Hollberg, J. E. Bjorkholm, A. Cable, and A. Ashkin, "Three-dimensional viscous confinement and cooling of atoms by resonance radiation pressure," *Phys. Rev. Lett.*, **55**, pp. 48–51 (1985)

[67] P. D. Lett, W. D. Phillips, S. L. Rolston, C. E. Tanner, R. N. Watts, and C. I. Westbrook, "Optical molasses," *J. Opt. Soc. Am. B*, **6**, pp. 2084–2107 (1989)

[68] J. Dalibard and C. Cohen-Tannoudji, "Laser cooling below the Doppler limit by polarization gradients: simple theoretical models," *J. Opt. Soc. Am. B*, **6**, pp. 2023–2045 (1989)

[69] R. Grimm, M. Weidemüller, and Y. B. Ovchinnikov, "Optical Dipole Traps for Neutral Atoms," volume 42 of *Advances In Atomic, Molecular, and Optical Physics*, pp. 95 – 170 (Academic Press, 2000)

[70] N. W. Ashcroft and N. D. Mermin, *Solid State Physics* (Hartcourt College, 1976)

[71] A. E. Siegman, *Lasers* (University Science Books, Mill Valley, CA, 1986)

[72] Z. W. Barber, J. E. Stalnaker, N. D. Lemke, N. Poli, C. W. Oates, T. M. Fortier, S. A. Diddams, L. Hollberg, C. W. Hoyt, A. V. Taichenachev, and V. I. Yudin, "Optical Lattice Induced Light Shifts in an Yb Atomic Clock," *Phys. Rev. Lett.*, **100**, p. 103 002 (2008)

[73] J. E. Sansonetti, W. C. Martin, and S. L. Young, "Handbook of Basic Atomic Spectroscopic Data," (2012), http://www.nist.gov/pml/data/handbook/index.cfm

[74] D. R. Lide, editor, *CRC Handbook of Chemistry and Physics (Internet Version 2010)* (CRC Press/Taylor and Francis, 2010), 90th edition

[75] E. U. Condon and G. H. Shortley, *The Theory of Atomic Spectra* (Cambridge University Press, London, 1970)

[76] A. Kramida, Y. Ralchenko, J. Reader, and NIST ASD Team, "NIST Atomic Spectra Database (ver. 5.0)," (2012), http://physics.nist.gov/asd

[77] S. G. Porsev, Y. G. Rakhlina, and M. G. Kozlov, "Electric-dipole amplitudes, lifetimes, and polarizabilities of the low-lying levels of atomic ytterbium," *Phys. Rev. A*, **60**, pp. 2781–2785 (1999)

[78] K. Blagoev and V. Komarovskii, "Lifetimes of Levels of Neutral and Singly Ionized Lanthanide Atoms," *Atomic Data and Nuclear Data Tables*, **56**, pp. 1–40 (1994)

[79] Y. Takasu, K. Komori, K. Honda, M. Kumakura, T. Yabuzaki, and Y. Takahashi, "Photoassociation Spectroscopy of Laser-Cooled Ytterbium Atoms," *Phys. Rev. Lett.*, **93**, p. 123 202 (2004)

[80] K. Honda, Y. Takahashi, T. Kuwamoto, M. Fujimoto, K. Toyoda, K. Ishikawa, and T. Yabuzaki, "Magneto-optical trapping of Yb atoms and a limit on the branching ratio of the $^1P_1$ state," *Phys. Rev. A*, **59**, pp. R934–R937 (1999)

[81] J. W. Cho, H.-g. Lee, S. Lee, J. Ahn, W.-K. Lee, D.-H. Yu, S. K. Lee, and C. Y. Park, "Optical repumping of triplet-P states enhances magneto-optical trapping of ytterbium atoms," *Phys. Rev. A*, **85**, p. 035 401 (2012)

[82] J. E. Golub, Y. S. Bai, and T. W. Mossberg, "Radiative and dynamical properties of homogeneously prepared atomic samples," *Phys. Rev. A*, **37**, pp. 119–124 (1988)

[83] D. Das, S. Barthwal, A. Banerjee, and V. Natarajan, "Absolute frequency measurements in Yb with 0.08 ppb uncertainty: Isotope shifts and hyperfine structure in the 399 nm $^1S_0 \rightarrow {}^1P_1$ line," *Phys. Rev. A*, **72**, p. 032 506 (2005)

[84] S. G. Porsev, A. Derevianko, and E. N. Fortson, "Possibility of an optical clock using the 6 $^1\mathrm{S}_0 \rightarrow 6\ ^3\mathrm{P}^o_0$ transition in ^{171,173}Yb atoms held in an optical lattice," *Phys. Rev. A*, **69**, p. 021 403 (2004)

[85] A. V. Taichenachev, V. I. Yudin, C. W. Oates, C. W. Hoyt, Z. W. Barber, and L. Hollberg, "Magnetic Field-Induced Spectroscopy of Forbidden Optical Transitions with Application to Lattice-Based Optical Atomic Clocks," *Phys. Rev. Lett.*, **96**, p. 083 001 (2006)

[86] Z. W. Barber, C. W. Hoyt, C. W. Oates, L. Hollberg, A. V. Taichenachev, and V. I. Yudin, "Direct Excitation of the Forbidden Clock Transition in Neutral ^{174}Yb Atoms Confined to an Optical Lattice," *Phys. Rev. Lett.*, **96**, p. 083 002 (2006)

[87] Z. W. Barber, *Ytterbium Optical Lattice Clock*, Ph.D. thesis, University of Colorado (2007)

[88] K. Pandey, A. K. Singh, P. V. K. Kumar, M. V. Suryanarayana, and V. Natarajan, "Isotope shifts and hyperfine structure in the 555.8 nm $^1S_0 \rightarrow {}^3P_1$ line of Yb," *Phys. Rev. A*, **80**, p. 022 518 (2009)

[89] A. Yariv, *Quantum electronics* (Wiley, New York, 1989), third edition

[90] W. P. Risk, T. R. Gosnell, and A. V. Nurmikko, *Compact Blue-Green Lasers* (Cambridge University Press, New York, 2003)

[91] G. D. Boyd and D. A. Kleinman, "Parametric Interaction of Focused Gaussian Light Beams," *J. Appl. Phys.*, **39**, pp. 3597–3639 (1968)

[92] T. Hansch and B. Couillaud, "Laser frequency stabilization by polarization spectroscopy of a reflecting reference cavity," *Opt. Commun.*, **35**, pp. 441–444 (1980)

[93] G. Ferrari, J. Catani, L. Fallani, G. Giusfredi, G. Schettino, F. Schäfer, and P. C. Pastor, "Coherent addition of laser beams in resonant passive optical cavities," *Opt. Lett.*, **35**, pp. 3105–3107 (2010)

[94] R. Maruyama, *Optical Trapping of Ytterbium Atoms*, Ph.D. thesis, University of Washington (2003)

[95] A. V. Smith, "SNLO nonlinear optics code," (2009), http://www.as-photonics.com/SNLO

[96] E. S. Polzik and H. J. Kimble, "Frequency doubling with $KNbO_3$ in an external cavity," *Opt. Lett.*, **16**, pp. 1400–1402 (1991)

[97] H. Kogelnik and T. Li, "Laser Beams and Resonators," *Appl. Opt.*, **5**, pp. 1550–1567 (1966)

[98] T. Freegarde and C. Zimmermann, "On the design of enhancement cavities for second harmonic generation," *Opt. Commun.*, **199**, pp. 435–446 (2001)

[99] A. Nevsky, U. Bressel, I. Ernsting, C. Eisele, M. Okhapkin, S. Schiller, A. Gubenko, D. Livshits, S. Mikhrin, I. Krestnikov, and A. Kovsh, "A narrow-line-width external cavity quantum dot laser for high-resolution spectroscopy in the near-infrared and yellow spectral ranges," *Appl. Phys. B*, **92**, pp. 501–507 (2008)

[100] C. Oates, Z. Barber, J. Stalnaker, C. Hoyt, T. Fortier, S. Diddams, and L. Hollberg, "Stable Laser System for Probing the Clock Transition at 578 nm in Neutral Ytterbium," in "Frequency Control Symposium, 2007 Joint with the 21st European Frequency and Time Forum. IEEE International," pp. 1274–1277 (2007)

[101] G. Dick, "Local oscillator induced instabilities in trapped ion frequency standards," Technical report, DTIC Document (1987)

[102] G. Santarelli, C. Audoin, A. Makdissi, P. Laurent, G. Dick, and A. Clairon, "Frequency stability degradation of an oscillator slaved to a periodically interrogated atomic resonator," *IEEE Trans. Ultrason., Ferroelect., Freq. Cont.*, **45**, pp. 887–894 (1998)

[103] S. Herrmann, A. Senger, K. Möhle, M. Nagel, E. V. Kovalchuk, and A. Peters, "Rotating optical cavity experiment testing Lorentz invariance at the 10^{-17} level," *Phys. Rev. D*, **80**, p. 105 011 (2009)

[104] A. Bartels, S. A. Diddams, C. W. Oates, G. Wilpers, J. C. Bergquist, W. H. Oskay, and L. Hollberg, "Femtosecond-laser-based synthesis of ultrastable microwave signals from optical frequency references," *Opt. Lett.*, **30**, pp. 667–669 (2005)

[105] K. Predehl, G. Grosche, S. M. F. Raupach, S. Droste, O. Terra, J. Alnis, T. Legero, T. W. Hänsch, T. Udem, R. Holzwarth, and H. Schnatz, "A 920-Kilometer Optical Fiber Link for Frequency Metrology at the 19th Decimal Place," *Science*, **336**, pp. 441–444 (2012)

[106] T. Accadia et al., "Status of the Virgo project," *Class. Quant. Grav.*, **28**, p. 114 002 (2011)

[107] R. W. P. Drever, J. L. Hall, F. V. Kowalski, J. Hough, G. M. Ford, A. J. Munley, and H. Ward, "Laser phase and frequency stabilization using an optical resonator," *Appl. Phys. B*, **31**, pp. 97–105 (1983)

[108] E. D. Black, "An introduction to Pound-Drever-Hall laser frequency stabilization," *Amer. J. Phys.*, **69**, pp. 79–87 (2001)

[109] T. Nazarova, F. Riehle, and U. Sterr, "Vibration-insensitive reference cavity for an ultra-narrow-linewidth laser," *Appl. Phys. B*, **83**, pp. 531–536 (2006)

[110] A. D. Ludlow, X. Huang, M. Notcutt, T. Zanon-Willette, S. M. Foreman, M. M. Boyd, S. Blatt, and J. Ye, "Compact, thermal-noise-limited optical cavity for diode laser stabilization at 1×10^{-15}," *Opt. Lett.*, **32**, pp. 641–643 (2007)

[111] J. Alnis, A. Matveev, N. Kolachevsky, T. Udem, and T. W. Hänsch, "Subhertz linewidth diode lasers by stabilization to vibrationally and thermally compensated ultralow-expansion glass Fabry-Pérot cavities," *Phys. Rev. A*, **77**, p. 053 809 (2008)

[112] S. A. Webster, M. Oxborrow, S. Pugla, J. Millo, and P. Gill, "Thermal-noise-limited optical cavity," *Phys. Rev. A*, **77**, p. 033 847 (2008)

[113] J. Millo, D. V. Magalhães, C. Mandache, Y. Le Coq, E. M. L. English, P. G. Westergaard, J. Lodewyck, S. Bize, P. Lemonde, and G. Santarelli, "Ultrastable lasers based on vibration insensitive cavities," *Phys. Rev. A*, **79**, p. 053 829 (2009)

[114] Y. Y. Jiang, A. D. Ludlow, N. D. Lemke, R. W. Fox, J. A. Sherman, L.-S. Ma, and C. W. Oates, "Making optical atomic clocks more stable with 10-16-level laser stabilization," *Nat. Photon.*, **5**, pp. 158–161 (2011)

[115] B. Argence, E. Prevost, T. Lévèque, R. L. Goff, S. Bize, P. Lemonde, and G. Santarelli, "Prototype of an ultra-stable optical cavity for space applications," *Opt. Express*, **20**, pp. 25 409–25 420 (2012)

[116] T. Kessler, C. Hagemann, C. Grebing, T. Legero, U. Sterr, F. Riehle, M. J. Martin, L. Chen, and J. Ye, "A sub-40-mHz-linewidth laser based on a silicon single-crystal optical cavity," *Nat. Photon.*, **6**, pp. 687–692 (2012)

[117] T. Legero, T. Kessler, and U. Sterr, "Tuning the thermal expansion properties of optical reference cavities with fused silica mirrors," *J. Opt. Soc. Amer. B*, **27**, pp. 914–919 (2010)

[118] K. Numata, A. Kemery, and J. Camp, "Thermal-Noise Limit in the Frequency Stabilization of Lasers with Rigid Cavities," *Phys. Rev. Lett.*, **93**, p. 250 602 (2004)

[119] M. Pizzocaro, G. Costanzo, M. Zoppi, D. Calonico, F. Levi, A. Mura, and A. Godone, "Generation of an ultrastable 578 nm laser for Yb Lattice clock," in "Frequency Control and the European Frequency and Time Forum (FCS), 2011 Joint Conference of the IEEE International," pp. 1–4 (2011)

[120] T. Kessler, T. Legero, and U. Sterr, "Thermal noise in optical cavities revisited," *J. Opt. Soc. Amer. B*, **29**, p. 178 (2012)

[121] S. A. Webster, M. Oxborrow, and P. Gill, "Vibration insensitive optical cavity," *Phys. Rev. A*, **75**, p. 011 801 (2007)

[122] M. Pizzocaro, D. Calonico, C. Calosso, C. Clivati, G. Costanzo, F. Levi, and A. Mura, "Active disturbance rejection control of temperature for ultrastable optical cavities," *IEEE Trans. Ultrason., Ferroelect., Freq. Cont.*, **60**, pp. 273–280 (2013)

[123] E. A. Donley, T. P. Heavner, F. Levi, M. O. Tataw, and S. R. Jefferts, "Double-pass acousto-optic modulator system," *Rev. Sci. Inst.*, **76**, 063112 (2005)

[124] M. Pizzocaro, D. Calonico, C. Calosso, C. Clivati, G. A. Costanzo, F. Levi, and A. Mura, "Active Disturbance Rejection Control: Application to the Temperature Stabilization of Ultra-Stable Cavities," in "Proceedings of the 26th European Frequency and Time forum," pp. 169–173 (2012)

[125] J. Han, "Nonlinear Design Methods for Control Systems," in "Proc. Of The 14th IFAC World Congress," (1999)

[126] Z. Gao, "Scaling and bandwidth-parameterization based controller tuning," in "American Control Conference, 2003. Proceedings of the 2003," volume 6, pp. 4989–4996 (2003)

[127] Z. Gao, "Active disturbance rejection control: a paradigm shift in feedback control system design," in "American Control Conference, 2006," pp. 2399–2405 (2006)

[128] Q. Zheng, L. Gao, and Z. Gao, "On stability analysis of active disturbance rejection control for nonlinear time-varying plants with unknown dynamics," in "Decision and Control, 2007 46th IEEE Conference on," pp. 3501–3506 (2007)

[129] R. Miklosovic, A. Radke, and Z. Gao, "Discrete implementation and generalization of the extended state observer," in "American Control Conference, 2006," pp. 2209–2214 (2006)

[130] J. Rutman, "Characterization of phase and frequency instabilities in precision frequency sources: Fifteen years of progress," *Proc. IEEE*, **66**, pp. 1048–1075 (1978)

[131] D. A. Howe, D. W. Allan, and J. A. Barnes, "Properties of Signal Sources and Measurement Methods," in "Thirty Fifth Annual Frequency Control Symposium. 1981," pp. 669–716 (1981)

[132] G. Santarelli, A. Clairon, S. N. Lea, and G. M. Tino, "Heterodyne optical phase-locking of extended-cavity semiconductor lasers at 9 GHz," *Opt. Commun.*, **104**, pp. 339–344 (1994)

[133] C. M. Caves, "Quantum-Mechanical Radiation-Pressure Fluctuations in an Interferometer," *Phys. Rev. Lett.*, **45**, pp. 75–79 (1980)

[134] N. R. Newbury, P. A. Williams, and W. C. Swann, "Coherent transfer of an optical carrier over 251 km," *Opt. Lett.*, **32**, pp. 3056–3058 (2007)

[135] L.-S. Ma, P. Jungner, J. Ye, and J. L. Hall, "Delivering the same optical frequency at two places: accurate cancellation of phase noise introduced by an optical fiber or other time-varying path," *Opt. Lett.*, **19**, pp. 1777–1779 (1994)

[136] H. Jiang, F. Kéfélian, S. Crane, O. Lopez, M. Lours, J. Millo, D. Holleville, P. Lemonde, C. Chardonnet, A. Amy-Klein, and G. Santarelli, "Long-distance frequency transfer over an urban fiber link using optical phase stabilization," *J. Opt. Soc. Am. B*, **25**, pp. 2029–2035 (2008)

[137] P. A. Williams, W. C. Swann, and N. R. Newbury, "High-stability transfer of an optical frequency over long fiber-optic links," *J. Opt. Soc. Am. B*, **25**, pp. 1284–1293 (2008)

[138] M. L. Meade, *Lock-in amplifiers: principles and applications*, IEE Electrical Measurement Series 1 (Peter Peregrinus on behalf of the Institution of Electrical Engineers, London, UK, 1983)

[139] M. Zoppi, *Development of an atomic frequency standard in the optical domain based on ultracold ytterbium atoms*, Ph.D. thesis, Politecnico di Torino (2012)

[140] M. Schioppo, *Development of a Transportable Strontium Optical Clock*, Ph.D. thesis, Università degli Studi di Firenze (2010)

[141] M. Schioppo, N. Poli, M. Prevedelli, S. Falke, C. Lisdat, U. Sterr, and G. M. Tino, "A compact and efficient strontium oven for laser-cooling experiments," *Rev. Sci. Inst.*, **83**, 103101 (2012)

[142] A. Noble and M. Kasevich, "UHV optical window seal to conflat knife edge," *Rev. Sci. Inst.*, **65**, pp. 3042–3043 (1994)

[143] A. Brusch, *Horloge à réseau optique à atomes de Strontium, et étude des effets d'hyperpolarisabilité dus aux pièges laser*, Ph.D. thesis, Université Paris VI (2006)

[144] D. M. Hoffman, B. Singh, and J. H. I. Thomas, *Handbook of Vacuum Science and Technology* (Academic Press, 1997)

[145] Duniway Stockroom Corporation, *New Duniway Ion Pumps Instruction Manual* (2008)

[146] H. P. Steinrück and K. D. Rendulic, "A test of capillary array beam sources for very large Knudsen numbers," *Vacuum*, **36**, pp. 213–215 (1986)

[147] P. Clausing, "The Flow of Highly Rarefied Gases through Tubes of Arbitrary Length," *J. Vac. Sci. & Tech.*, **8**, pp. 636–646 (1971), translation of [165]

[148] N. F. Ramsey, *Molecular Beams* (Oxford University Press, 1956)

[149] T. P. Meyrath, "Electromagnet Design Basics for Cold Atom Experiments," Technical report, Atom Optics Laboratory Center for Nonlinear Dynamics - University of Texas at Austin (2004)

[150] I. Courtillot, *Première observation de la transition fortement interdite* $^1S_0 - {}^1P_0$ *du strontium, pour une horloge optique à atomes piégés*, Ph.D. thesis, Université de Paris VI (2003)

[151] T. Bergeman, G. Erez, and H. J. Metcalf, "Magnetostatic trapping fields for neutral atoms," *Phys. Rev. A*, **35**, pp. 1535–1546 (1987)

[152] N. D. Lemke, J. von Stecher, J. A. Sherman, A. M. Rey, C. W. Oates, and A. D. Ludlow, "p-Wave Cold Collisions in an Optical Lattice Clock," *Phys. Rev. Lett.*, **107**, p. 103 902 (2011)

[153] J. A. Sherman, N. D. Lemke, N. Hinkley, M. Pizzocaro, R. W. Fox, A. D. Ludlow, and C. W. Oates, "High-Accuracy Measurement of Atomic Polarizability in an Optical Lattice Clock," *Phys. Rev. Lett.*, **108**, p. 153 002 (2012)

[154] J. A. Sherman, "Coping with the Blackbody Radiation Shift in a Yb optical frequency standard," (2012), unpublished

[155] S. G. Porsev and A. Derevianko, "Multipolar theory of blackbody radiation shift of atomic energy levels and its implications for optical lattice clocks," *Phys. Rev. A*, **74**, p. 020 502 (2006)

[156] K. Beloy, J. A. Sherman, N. D. Lemke, N. Hinkley, C. W. Oates, and A. D. Ludlow, "Determination of the $5d6s$ $^3D_1$ state lifetime and blackbody-radiation clock shift in Yb," *Phys. Rev. A*, **86**, p. 051 404 (2012)

[157] L. Hunter, D. K. Jr., K. Miller, D. Berkeland, and M. Boshier, "Precise measurement of the Stark shift of the cesium D1 line," *Opt. Commun.*, **94**, pp. 210–214 (1992)

[158] S. Reid, G. Cagnoli, E. Elliffe, J. Faller, J. Hough, I. Martin, and S. Rowan, "Influence of temperature and hydroxide concentration on the settling time of hydroxy-catalysis bonds," *Phys. Lett. A*, **363**, pp. 341–345 (2007)

[159] D. S. Sivia and J. Skilling, *Data Analysis - a Bayesian Tutorial* (Oxford University Press, 2006), second edition

[160] T. Middelmann, C. Lisdat, S. Falke, J. Winfred, F. Riehle, and U. Sterr, "Tackling the Blackbody Shift in a Strontium Optical Lattice Clock," *IEEE Trans. Instrum. Meas.*, **60**, pp. 2550–2557 (2011)

[161] J. Lodewyck, M. Zawada, L. Lorini, M. Gurov, and P. Lemonde, "Observation and cancellation of a perturbing dc stark shift in strontium optical lattice clocks," *IEEE Trans. Ultrason., Ferroelect., Freq. Cont.*, **59**, pp. 411 –415 (2012)

[162] M. Takamoto, T. Takano, and H. Katori, "Frequency comparison of optical lattice clocks beyond the Dick limit," *Nat. Photon.*, **5**, pp. 288–292 (2011)

[163] J. L. Hall, L. Hollberg, T. Baer, and H. G. Robinson, "Optical heterodyne saturation spectroscopy," *Appl. Phys. Lett.*, **39**, pp. 680–682 (1981)

[164] J. H. Shirley, "Modulation transfer processes in optical heterodyne saturation spectroscopy," *Opt. Lett.*, **7**, pp. 537–539 (1982)

[165] P. Clausing, *Ann. Physik*, **12**, p. 961 (1932)